UNIVERSITY OF OKLAHOMA

GRADUATE COLLEGE

INVESTIGATIONS OF THE MECHANICAL AND MICROSTRUCTURAL PROPERTIES OF THE ATRIOVENTRICULAR HEART VALVE LEAFLETS AND CHORDAE TENDINEAE

A THESIS

SUBMITTED TO THE GRADUATE FACULTY

in partial fulfillment of the requirements for the

Degree of

MASTER OF SCIENCE

By

COLTON JAY ROSS
Norman, Oklahoma
2020

INVESTIGATIONS OF THE MECHANICAL AND MICROSTRUCTURAL PROPERTIES OF THE ATRIOVENTRICULAR HEART VALVE LEAFLETS AND CHORDAE TENDINEAE

A THESIS APPROVED FOR THE

SCHOOL OF AEROSPACE AND MECHANICAL ENGIENERING

BY THE COMMITTEE CONSISTING OF

Dr. Chung-Hao Lee, Chair

Dr. Kuang-Hua Chang

Dr. Rachel Childers

This thesis is dedicated to my parents, my family, and my friends

Your love, support, and guidance have made this all possible

Table of Contents

Table of Contents v

List of Figures viii

List of Tables xix

Acknowledgments xxi

ABSTRACT OF THE THESIS xxii

CHAPTER 1 – INTRODUCTION 1

1.1 Motivation 1

1.2 Objective and Scope 2

CHAPTER 2 – LITERATURE REVIEW 5

2.1 Overview of the Atrioventricular Heart Valve Anatomy and Function 5

2.2 Heart Valve Regurgitation 17

2.3 Purpose of the Thesis 19

CHAPTER 3 – BIAXIAL MECHANICAL CHARACTERIZATIONS OF AHV LEAFLETS . 21

3.1 Methods 22

3.2 Results 32

3.3 Discussion 43

3.4 Concluding Remarks 46

CHAPTER 4 – MECHANICS OF AHV LEAFLET-CT-PAPILLARY MUSCLES ENTITIES 48

4.1 Methods 49

4.2 Results 54

4.3 Discussion 58

4.4 Concluding Remarks 65

CHAPTER 5 – MICROSTRUCTURE-MECHANICS RELATIONSHIPS OF THE CT-LEAFLET INSERTION 66

5.1 Methods 68

5.2 Results 78

5.3 Discussion 94

5.4 Concluding Remarks 98

CHAPTER 6 – CONCLUSIONS AND FUTURE WORK 99

6.1 Conclusions 99

6.2 Recommendations for Future Research 101

APPENDIX A – NOMENCLATURE 103

APPENDIX B – DETAILED BIAXIAL MECHANICAL TESTING PROCEDURES FOR VALVE LEAFLETS 105

APPENDIX C – UNIAXIAL MECHANICAL TESTING AND POLARIZED SPATIAL FREQUENCY DOMAIN IMAGING PROCEDURES FOR THE LEAFLET-CT-PAPILLARY MUSCLE ENTITY 127

APPENDIX D – POST-PROCESSING PIPELINE FOR MECHANICAL AND PSFDI DATA OF THE LEAFLET-CT-PAPILLARY MUSCLE ENTITIES 136

List of Figures

Figure 2-1. Schematic of the heart anatomy and the AHVs (image adapted from uptodate.com). 5

Figure 2-2. An excised porcine MVAL, illustrating the basal, strut, and marginal chordae. 6

Figure 2-3. Micrographs of the porcine TV leaflets' microstructure using Movat's Pentachrome staining to highlight the elastin, collagen fibers, non-fibrous ground substance, and valvular interstitial cells. The four morphologically distinct layers are also illustrated in each image, i.e., A: atrialis, S: spongiosa, F: fibrosa, and V: ventricularis..... 8

Figure 2-4. (a) Schematic of the excised leaflet tissue and the central bulk region taken for mechanical testing. (b) An illustration of the mounted TV leaflet tissue specimen onto the biaxial testing system with the collagen fiber orientations (i.e., the circumferential and radial directions) aligned with the testing *x*- and *y*-directions. (c) First-PK stress versus stretch results of the porcine TVAL, TVPL, and TVSL tissues (n = 6) under equibiaxial loading (F_x:F_y = 1:1). Results are presented in mean ± SEM. Images were modified from Jett *et al.* (2018) [12]. 9

Figure 2-5. Schematic of the chordae tendineae microstructure (image from Millington-Sanders *et al.* (1998) [37]). 11

Figure 2-6. Scanning electron micrograph of (a) external endothelial cells, (b) elastin fibers, and (c) collagen fiber waves of the chordae (image from Millington-Sanders *et al.* (1998) [37]). 12

Figure 2-7. (a) A micrograph of a cross-section of the CT, showing the collagen core (C) and connective tissues (CT). (b) Within the connective tissue cushion, a disorganized

network of elastin fibers (E) and endothelium (En) exists (image from Millington-Sanders *et al.* (1998) [37]). 12

Figure 2-8. Digital microscopic image of the mitral valve strut chordae-leaflet insertion (from Chen, *et al.* (2004) [40]). Dotted lines correspond to imaging locations used for quantifying the fiber angle. 14

Figure 2-9. Various mechanical characterization methods for the AHV chordae tendineae: (a) uniaxial mechanical testing, (b) stress-relaxation testing, (c) CT-leaflet insertion deformation tracking, and (d) *in vitro* heart-simulating flow loops. 15

Figure 2-10. Results from uniaxial mechanical testing by Pokutta-Paskaleva *et al*. (2019) [15] for characterizing the strut, marginal, and basal CT from: (a) the MVAL, and (b) the TVAL. 16

Figure 2-11. Visualization of severe tricuspid regurgitation using two different 2D transthoracic echocardiography views and color flow Doppler: (a) a parasternal long-axis inflow view, and (b) an apical four-chamber view of a newborn with a severe pulmonary hypertension due to diaphragmatic hernia. (Images provided by Drs. Mir and Burkhart at the OUHSC) 18

Figure 3-1. Dissected porcine hearts showing: (a) the mitral valve, and (b) the tricuspid valve with the anterior leaflet highlighted for both atrioventricular heart valves. (c) Schematic of a valve anterior leaflet with the six smaller delimited regions. 22

Figure 3-2. Microdissection process for an MVAL tissue, showing the atrialis layer first separated from the remaining tissue. 9/16" head T-pins were used to fasten the tissue on a wax tray. 24

Figure 3-3. (a) Experimental setup for biaxial mechanical testing of the MVAL and TVAL tissue specimens. Schematic of the testing procedures: (b) force-controlled biaxial testing protocol, and (c) biaxial stress relaxation testing protocol. 25

Figure 3-4. Schematic of the enzyme-based GAG removal treatment: (a) tissue strips of the MVAL or the TVAL used for determination of optimal treatment; (b) tissue specimen (either the tissue strip used for histology, or the square tissue used for biaxial mechanical testing) in a 3mL vial with a warm enzyme bath. 29

Figure 3-5. Mean ± SEM of membrane tension versus total tissue stretch results for the six MVAL tissue regions under equibiaxial loading protocol ($T_{circ,\max} : T_{rad,\max} = 1{:}1$). The labels (a-f) correspond to the region label defined in **Figure 3-1c**. N.S.: non-statistically significant. 33

Figure 3-6. Mean ± SEM of membrane tension versus total tissue stretch results for the six TVAL tissue regions under equibiaxial loading protocol ($T_{circ,\max} : T_{rad,\max} = 1{:}1$). The labels (a-f) correspond to the region label defined in **Fig. 3-1c**. N.S.: non-statistically significant. 34

Figure 3-7. Mean ± SEM of the normalized membrane tension versus time results from the stress relaxation testing for all the six MVAL tissue regions. 35

Figure 3-8. Mean ± SEM of the normalized membrane tension versus time results from the stress relaxation testing for all the six TVAL tissue regions. 36

Figure 3-9. Histological images with Movat's Pentachrome stain: (a) intact MVAL tissue, (b) separated fibrosa layer (F), combined atrialis/spongiosa (A/S), and ventricularis (V). 37

Figure 3-10. Histological images with Movat's Pentachrome stain: (a) intact TVAL tissue, and (b) separated combined atrialis/spongiosa (A/S) and combined fibrosa/ventricularis (F/V) layers. 37

Figure 3-11. Mean ± SEM of the biaxial mechanical testing results (first Piola-Kirchhoff stress versus peak stretch) of TVAL layer tissues (n=6) under equibiaxial loading. 39

Figure 3-12. Mean ± SEM of the biaxial mechanical testing results (first Piola-Kirchhoff stress versus peak stretch) of MVAL layer tissues (n=6) under equibiaxial loading. 39

Figure 3-13. Alcian blue-stained histological images demonstrating the progression of the GAG constituent removal associated with various enzyme treatment durations. Scale bar=200 μm. 40

Figure 3-14. Mean ± SEM of the peak tissue stretch responses of the control and enzyme-treated groups for the MVAL (n=7). (*: statistically significant; N.S.: statistically non-significant)..... 41

Figure 3-15. Mean ± SEM of the peak tissue stretch responses of the control and enzyme-treated groups for the TVAL (n=6). (*: statistically significant; N.S.: statistically non-significant)..... 41

Figure 3-16. Comparison of the 15-minute biaxial stress-relaxation responses (mean ± SEM) of the MVAL between the control and enzyme-treated groups: (a) circumferential; (b) radial directions. (*: statistically significant) 43

Figure 3-17. Comparison of the 15-minute biaxial stress-relaxation responses (mean ± SEM) of the TVAL between the control and enzyme-treated groups: (a) circumferential; (b) radial directions. (N.S.: statistically non-significant)..... 43

Figure 4-1. (a) Photo of a dissected representative porcine MV. (b) Schematic of the leaflet-CT-PM entities from the left and right sides of the leaflet's apex. (c) Measurement of the chordae thickness by a microscope. (d) Experimental setting of the leaflet-CT-PM entity. (e) Uniaxial mechanical testing protocol for characterizing the leaflet-CT-PM entity specimens (the targeted target force: F_{max}=1.4 N or 1.2 N for the MVAL or TVAL strut CT, respectively)..... 50

Figure 4-2. Cauchy stress versus stretch responses of (a) the MVAL strut CT, and (b) the TVAL strut CT. Values are reported as mean±SEM (n=12). 54

Figure 4-3. Box plots of the (a) peak stretch, (b) preconditioning stretch, (c) stretch, and (d) diameter *D* of the left chordae group (LG) and right chordae group (RG) of the MVAL and TVAL strut CT tissues. (*: $p<0.05$, N.S.: not significant)..... 56

Figure 4-4. Representative Ogden model fits to the Cauchy stress-stretch data: (a) MVAL-LG #5 (μ=40.8 kPa; α=205.2), and (b) TVAL-LG #1 (μ=17.7 kPa; α=241.2). (black dots (•) denote experimental data, and red solid curves (–) refer to the Ogden constitutive model fits)..... 56

Figure 4-5. (a) Schematic of the clamp-based testing configuration used in [94]. (b) Comparison to the uniaxial testing setup of the present study, which allows the analysis of tissue deformation of strut CT, especially for the CT-leaflet insertion and the chordae-PM attachment..... 60

Figure 4-6. Distributions of the stretch across the CT domain determined by the cubic B-spline fitting (n=12): (a) MVAL-LG, (b) MVAL-RG, (c) TVAL-LG, and (d) TVAL-RG. 63

Figure 4-7. Variations in the stretch of the four quarter-sections of the CT segment: (a) MVAL strut chordae, and (b) TVAL strut chordae. Values are reported as mean ± SEM (n=12) 64

Figure 5-1. (a) Illustration of a tricuspid valve and its sub-valvular components. (b) Schematic of the leaflet-strut CT-papillary muscle entity-based tissue specimen dissected from porcine mitral valves and tricuspid valves under investigation. (c) Integrated instrument for conducting uniaxial mechanical testing and collagen fiber microstructural quantification. (d) Six loading points defined along the force-displacement curve for acquiring load-dependent CFAs. (e) Schematic of the sub-regions for analyzing the regional variations in the quantified CFAs for the CT-leaflet insertion. 68

Figure 5-2. Algorithmic flowchart for the differential evolution optimization framework used in determining the Ogden-type constitutive model parameters. 72

Figure 5-3. (a) Illustration of the birefringent reflected light intensity versus polarizer angle $\theta_{polarizer}$ for an example of a (cylindrical) collagen fiber with an orientation angle θ_{fiber} =90°, where the maximum intensity occurs when $\theta_{polarizer}$ and θ_{fiber} match each other. (b) pSFDI image from a representative TVAL strut CT-leaflet insertion, with the region of interest (ROI) of the tissue outlined in red, together with a selected pixel (red circle). (c) Measured reflected light intensity versus $\theta_{polarizer}$ from the analyzed pixel (red circle in (b)), superimposed with the 3-term Fourier series fit that shows how θ_{fiber} was determined. 75

Figure 5-4. Schematic of the procedure for generating the sub-regions of the load-dependent CFAs of the CT-leaflet insertions. The isoparametric mapping concept was adopted, and the uniform 3x3 grid was generated in the parametric domain and mapped back to the CT-leaflet insertion in the physical domain. 76

Figure 5-5. Whisker box plots for (a) the thickness, (b) the Cauchy stress σ, (c) the tissue stretch λ, and (d-e) the Ogden model parameters, μ and α, for the TVAL and MVAL CT segments. 79

Figure 5-6. Progressive CFAs of a representative TVAL strut chordae entity specimen under uniaxial mechanical testing (~38,000 pixels in the analyzed region). The white lines represent the predicted collagen fiber orientations of the selected coarser pixels (for visualization purpose), and the colormap intensities signify the degree of optical anisotropy (DOA). Values of the predicted θ_{fiber} and DOA are presented as mean±SEM. 80

Figure 5-7. Progressive CFAs of a representative MVAL strut chordae entity specimen under uniaxial mechanical testing (~15,000 pixels in the analyzed region). The white lines represent the predicted collagen fiber orientations of selected coarser pixels (for visualization purpose), and the colormap intensities signify the degree of optical anisotropy (DOA). Values of the predicted θ_{fiber} and DOA are presented as mean±SEM. 81

Figure 5-8. Comparison of the predicted DOAs of the CT-leaflet insertions between the sequential loading points from the 3x3 sub-regional analysis: (a) Loading Points 0 vs. 1, (b) Loading Points 1 vs. 2, (c) Loading Points 2 vs. 3, (d) Loading Points 3 vs. 4, and (e)

Loading Points 4 vs. 5. Values are presented as mean±SEM, and * denotes a statistically significant change, as obtained through one-way ANOVA ($p<0.05$)... 92

Figure B-1. Experimental photos of porcine hearts retrieved from a local slaughterhouse: (a) whole heart is rinsed of blood with PBS, (b) a cut is made between the atria and ventricle to reveal both the MV and the TV, and (c) blood clots are removed from the heart before storage. 106

Figure B-2. Experimental photos of the opened porcine heart, showing the five AHV leaflets and other sub-valvular components: (a) the MV with dissection of the left heart along the commissure between the two leaflets , and (b) the TV with similar dissection on the right heart. 108

Figure B-3. Photos of the excised leaflet being prepared for biaxial mechanical testing: Heart valve leaflet testing requires the (a) bulk leaflet be sectioned into a (b) 10mm x 10mm testing region (radial direction noted by surgical pen markers). (c) The leaflet thickness is measured. Specimens are mounted to (d) the biaxial testing system by (e) piercing the tissue with metal tines. After mounting, (f) fiducial markers are glued onto the surface of the tissue before (g) submersion in PBS solution at 37 °C. ... 110

Figure B-4. Example protocol parameters for the preconditioning testing of an MVAL with a 7.5x 7.5mm testing region: The preconditioning protocol is created by setting (a) the protocol name, (b) the testing control mode and force in the *X*-axis, (c) the preload conditions, (d) the *Y*-axis parameters to be the same as in the *X*-axis, and (e) the cycle parameters. 113

Figure B-5. Example protocol parameters for the timing step for an MVAL with a 7.5x7.5mm testing region: The timing step requires (a) moving the tissue from the post preconditioning deformation to the peak membrane tension (and corresponding peak deformation) while simultaneously starting a stopwatch to record the stretch time. When the target force has been reached, (b) the post-preconditioning deformation is recorded. 114

Figure B-6. Schematic of the force-controlled biaxial testing procedure for testing mitral and tricuspid valve leaflets: The testing protocol consists of an equibiaxial loading preconditioning step to exercise the tissue to its in vivo state, followed by various loading ratios of the peak membrane tension in each tissue direction (T_X:T_Y): 1:1, 0.75:1, 1:0.75, 0.5:1, and 1:0.5. Each subsection of the force-controlled testing protocol is performed for 10 loading/unloading cycles..... 116

Figure B-7. Schematic of displacement-controlled biaxial testing procedure for testing mitral and tricuspid valve leaflets: The testing protocol consists of an (a) biaxial displacements associated with the peak membrane tensions, (b) pure shear in the *X*-direction, (c) constrained uniaxial displacement in the *X*-direction, (d) pure shear in the *Y*-direction, and (e) constrained uniaxial displacement in the *Y*-direction. Each subsection of the displacement-controlled testing protocol is performed for 10 loading/unloading cycles. 118

Figure B-8. Example stress-relaxation testing parameters for a mitral valve anterior leaflet with effective testing region of 7.5x7.5mm: Testing set parameters for stress-relaxation testing for a mitral valve anterior leaflet where targeted displacement is the peak tissue deformation specific to this tissue. 121

Figure B-9. Schematic of the 15-minute stress-relaxation testing procedure for testing mitral and tricuspid valve leaflets: The testing protocol involves holding biaxial displacements associated with the peak membrane tensions for 15 minutes, after which the tissue is returned to the mounting configuration. 122

Figure B-10. Example histological data from the atrioventricular heart valves' anterior leaflets: Representative histology images of (a) the mitral valve anterior leaflet, and (b) the tricuspid valve posterior leaflet. Both are stained with a Masson's trichrome stain: collagen in blue, cytoplasm and keratin in red, and nuclei in black. Scale bar=200 μm. 123

Figure B-11. Representative images illustrating the tracking of the coordinates of four fiducial markers during biaxial mechanical testing using a DIC technique: (a) the tissue mounting configuration, (b) the configuration after the preconditioning step, and (c) the deformed configuration associated with the tissue specimen under mechanical loading. 124

Figure C-1. The anatomical structures of a porcine: (a) mitral valve, and (b) tricuspid valve, with the strut chordae highlighted. 128

Figure C-2. The leaflet-CT-papillary muscle entity, with the ventricular surface of the leaflet facing upwards, showing the CT left group (LG) and the CT right group (RG). . 129

Figure C-3. A sectioned leaflet-CT-papillary muscle entity. 129

Figure C-4. Measuring the CT thickness with a digital caliper. 130

Figure C-5. The leaflet-CT-papillary muscle entity mounted to the BioTester via BioRakes. . 131

Figure C-6. Experimental photo of the integrated pSFDI-biaxial testing system. 133

Figure C-7. The camera software used for verifying the tissue within the polarizer lens 133

Figure C-8. The LightCrafter software, being used to project cyan light at a spatial frequency index of 12. 134

Figure C-9. The custom LabView program used for the pSFDI 135

List of Tables

Table 3-1. Percentage of GAGs in the control (time=0 mins) and enzyme-treated tissue strips over a 160-minute treatment time. All quantities are reported as mean ± SEM. 40

Table 4-1. Estimated Ogden model parameters for the MVAL strut CT, together with comparisons to other studies in the literature. (NRMSD: normalized root-mean-square deviation)57

Table 4-2. Estimated Ogden model parameters for the TVAL strut CT, together with comparisons to other studies in the literature. 58

Table 4-3. Comparisons of tissue stretches and Cauchy stresses. Values are reported as either mean±SEM or mean±standard deviation (SD), as indicated. 60

Table 5-1. Quantified collagen fiber architecture, including the predicted collagen fiber orientation angle θ_{fiber} and the predicted degree of optical anisotropy (DOA), for the CT segments (see **Fig. 5-1b**). Values are reported as mean±SEM. 83

Table 5-2. Percentage changes in the predicted degree of optical anisotropy (DOA) between two consecutive states of the 5 loading points for the CT segments (see **Fig. 5-1b**). Values are reported as mean±SEM, and p-values determined from the one-way ANOVA are given in square brackets. 84

Table 5-3. Quantified collagen fiber architecture, including the predicted collagen fiber orientation angle θ_{fiber} and the predicted degree of anisotropy (DOA), for the CT-leaflet insertions (see **Fig. 5-1b**). Values are reported as mean±SEM. 86

Table 5-4. Percentage changes in the predicted degree of optical anisotropy (DOA) between two consecutive states of the 5 loading points for the CT-leaflet insertions (see **Fig. 5-1b**).

Value are reported as mean±SEM, and p-values, determined from the one-way ANOVA, are given in square brackets. 87

Table 5-5. Regional analyses of the quantified collagen fiber architecture for the TVAL CT-leaflet insertion (n=8, see **Fig. 5-1e**). Values are reported as mean±SEM. 89

Table 5-6. Regional analyses of the quantified collagen fiber architecture for the MVAL CT-leaflet insertion (n=10, see **Fig. 5-1e**). Values are reported as mean±SEM. 90

Table 5-7. Percentage changes in the predicted degree of optical anisotropy (DOA) between two non-sequential loading states for sub-regions of the CT-leaflet insertion (see **Fig. 5-1e**). Values are reported as mean±SEM, and p-values are determined from the one-way ANOVA and multiple comparisons are given in square brackets. 94

Table A-1. Description of the abbreviations used throughout the thesis. 103

Table B-1. Full testing parameters for all protocols of the force-controlled testing scheme: Testing parameters for the force-controlled testing scheme. Forces (in millinewtons) are written as F to represent the force associated with targeted peak membrane tension. Stretch time is written as t to represent the stretch time (in seconds) specific to the tissue being tested. 117

Table B-2. Displacements (in percentages) are written as *dx* and *dy* to represent the peak post-preconditioning percent elongation in the *X*- and *Y*-directions, respectively. Stretch time is written as *t* to represent the stretch time (in seconds) specific to the tissue. Abbreviations are: PS, pure shear; CU, constrained uniaxial. 120

Acknowledgments

I will start by extending my thanks and appreciation to my advisor Dr. Chung-Hao Lee for continually working with me in both the development of this thesis, and my professional development. Just over two years ago I joined the lab on a whim, and my time since has contained some of the most transformative experiences of my life. Dr. Lee has been of great guidance in helping me realize and make progress towards my academic and career goals, and I am excited to continue my education and research with him in my pursuit of a Ph.D.

I would also like to thank my thesis committee members Dr. Chung-Hao Lee, Dr. Kuang-Hua Chang, and Dr. Rachel Childers for their consideration of my thesis, and the advice they have provided me along the way. I'm also grateful for the teachings they have provided me throughout my academic career, and the support they have shown for me. I would also like to extend acknowledgements to other faculty and staff at the University of Oklahoma who have helped me throughout my academic career so far.

My greatest thanks go out to my parents, my family, and my friends for supporting me every step of the way and helping me to always become a better person. I could not have asked for a better family, with the loving support of my parents, my brothers, and my sister – without them, none of this would have been possible. My closest friends, Lauren, Kirk, and Peyton, have also helped to keep me sane throughout the pursuit of this degree. In addition, I've made so many new friends in my time in the lab that have been some of the best people I have ever worked alongside, and that I am extremely grateful for – Devin, Luke H., Sergio, Rob, Ryan, and many more.

Thank you

Colton J. Ross

ABSTRACT OF THE THESIS

INVESTIGATIONS OF THE MECHANICAL AND MICROSTRUCTURAL PROPERTIES OF THE ATRIOVENTRICULAR HEART VALVE LEAFLETS AND CHORDAE TENDINEAE

by

Colton Jay Ross

Master of Science in Mechanical Engineering

University of Oklahoma, Norman, OK, 2020

Dr. Chung-Hao Lee, Chair

The unidirectional blood flow through the heart is facilitated by the atrioventricular heart valves – namely the mitral valve and the tricuspid valve. The two atrioventricular heart valves (AHVs) are composed of soft tissue leaflets that cyclically open and close throughout the cardiac cycle. The leaflets are supported in their functions by the chordae tendineae, which attach to the papillary muscles to distribute force loads that occur during systolic closure. The dysfunction of any of these valvular components can lead to retrograde blood flow during the valve closing, otherwise known as heart valve regurgitation. Current therapies for heart valve regurgitation range from repair of the native valve, to replacement by a mechanical or biological prosthesis, both of which suffer from different ailments including short- to long-term recurrence of the original pathological condition. Improvements of such therapies are contingent on a better understanding

of the biomechanics of the atrioventricular heart valves, including the tissue mechanical behaviors, tissue microstructures, and the relationships between the mechanics and the microstructure. To date, there is lacking information in literature regarding the complex mechanics, and mechanics-microstructure behaviors of these tissues. This thesis research addresses this gap in knowledge through three studies: (i) biaxial mechanical testing of AHV anterior leaflets to understand regionally-varying mechanical properties, the mechanics of individual leaflet layers, and the mechanical contributions of the glycosaminoglycans to the organ-level behaviors; (ii) cyclic, uniaxial tensile testing of the chordae tendineae using a unique tine-based leaflet-chordae-papillary muscle entity approach; and (iii) quantifications of the load-dependent changes in the collagen fiber architectures of the chordae-leaflet insertion region. In the first study series, we found that the AHV anterior leaflets had spatially-varying mechanics with central regions of the tissue being more anisotropic than the edge regions, as evident trough the anisotropy index, with the tricuspid valve anterior leaflet (TVAL) demonstrating an average anisotropy index of 1.09 in central regions and 1.02 in edge regions. We also observed that the atrialis/spongiosa layer was more compliant and more anisotropic than the fibrosa or ventricular layers. For example, in the TVAL we saw the atrialis/spongiosa layer was 9.0% and 12.3% more compliant in the peak stretch in the circumferential and radial directions, respectively, than the fibrosa/ventricularis layers. In addition, we saw glycosaminoglycan-deficient leaflets had higher extensibility (TVAL: 4.7% and 7.6% differences in the circumferential and radial peak stretches, respectively) and lower stress-relaxation behaviors (TVAL: 13.0% and 12.0% differences in the circumferential and radial relaxation, respectively). In the second study, we found that testing the chordae tendineae using the leaflet-chordae-papillary muscle procedure, preserving potential *in vivo* mechanical interactions, resulted in different uniaxial tensile behaviors than in previous studies, and that the

tissue stretches were non-uniform across the chordae domain (average peak stretch of 1.09 for the TVAL strut chordae). In the third study, we effectively quantified the load-dependent collagen fiber architecture changes across the same specimen and found that the center of the insertion had higher increases in fiber alignment than the edges of the insertion. Furthermore, we quantified the collagen fiber architecture changes through the degree of optical anisotropy and noticed increases in alignment up to 37.7% for the TVAL strut chordae-leaflet insertion between the mounting and peak loading configurations. Findings on the collagen fiber architectural changes are useful for better insight and connections between tissue mechanics and microstructure. In summary, these investigations greatly enhance the understanding of AHV biomechanics, which will be useful for the development of computational models and the refinement of therapeutics.

CHAPTER 1 – INTRODUCTION

1.1 Motivation

The atrioventricular heart valves (AHVs) regulate the unidirectional blood flow through the heart by cyclical opening and closing of the leaflets. The leaflets are supported in their functions by the chordae tendineae, which attach to the papillary muscles and provide necessary supporting forces during systolic closure (heart contraction). In cases of valvular heart diseases, the unidirectional flow of blood between the atrium and ventricles may be impaired, and regurgitant blood can jet into the atrium during valve closure. The regurgitation can cause a deficiency of blood in the ventricles, which can further result in a compensatory overworking of the heart and eventual heart failure. Current treatments for heart valve regurgitation can have sub-optimal outcomes, including recurrence of the original pathology, a need for reoperation due to deterioration of the treatment device, or the use of anti-coagulants for the remainder of the patient's life that can result in subsequent complications.

To reduce the issue of disease recurrence from heart valve surgeries, patient-specific computer simulations have been of increasing interest in the cardiovascular heart valve biomechanics literature. Patient-specific simulations will be a pivotal tool in the clinic for use in diagnosis, surgical planning, and therapeutic refinement, because each patient's unique heart valve geometry, as obtained by clinical computed tomography (CT) imaging or other medical imaging modalities, can be used for predictions of the heart valve behaviors pre- and post-treatment. Development of such predictive simulation tools requires detailed information on the interrelationship between the heart valve macro- and micro-structures and the mechanical behaviors of the tissues. In the previous literature, there have been many studies mechanically characterizing the heart valve

leaflets and the chordae tendineae; however, many of them do not consider the complexity of the tissues, such as the spatial variations in the tissues' mechanical properties or the connections between the tissue mechanics and their underlying collagen fiber microstructures. Improving our fundamental understanding of the complex tissue mechanical behaviors is critical to the refinement and enhancement of AHV computational models, and, thus, more systematic and comprehensive investigations of the mechanics and microstructure, as well as their connection to the organ-level heart valve function, are warranted.

1.2 Objective and Scope

The objective of this thesis research is to provide detailed quantifications of the mechanical behaviors of the two primary AHV components, namely the *leaflets* and the *chordae tendineae*. For the AHV *leaflets*, the studies performed involve:

(1) *Quantifying the regional variations in the stress-stretch behaviors*

In this study, porcine AHV anterior leaflets were retrieved from the valve apparatus and segmented into six delimited regions. These six regions were each biaxially tested to physiologically representative stresses, with varied loading ratios between the tissues' circumferential and radial directions to capture a full range of potential *in vivo* deformations. The spatial variations in the tissues' stress-stretch and stress-relaxation behaviors were quantified.

(2) *Mechanical characterizations of tissue layers of the AHV leaflets*

Similar biaxial mechanical testing protocols were used to quantify the mechanics of the four tissue layers of the AHV anterior leaflet: namely, the atrialis, spongiosa, fibrosa, and ventricularis layers. A microdissection procedure was performed to separate tissue layers,

and the separated tissue layers were biaxially tested to quantify their mechanical characteristics. The findings provide new insight to the mechanics-microstructure connections, and the variations in the AHV leaflet mechanics along the transmural (i.e., thickness) direction.

(3) *Quantification of the contributions of the glycosaminoglycan content to the AHV leaflet tissue's mechanical behaviors*

The contributions of the glycosaminoglycans (GAGs) to the biaxial mechanical behaviors of the AHV leaflets were further investigated. In this study, AHV leaflets were biaxially tested, enzymatically treated to remove a majority (>50%) of the GAG contents, and then biaxially tested again to observe the changes in the tissues' mechanical properties by utilizing the same leaflet specimen, which help to develop a better understanding of the interrelationship between tissue mechanics and its microstructural constituents.

For the AHV *chordae tendineae (CT)*, studies performed include:

(1) *Mechanical testing of chordae tendineae as a leaflet-CT-papillary muscle entity*

In this work, the load-bearing strut chordae tendineae of porcine AHVs were dissected as a leaflet-CT-papillary muscle entity, by maintaining the CT-leaflet insertion and CT-papillary muscle attachment. Uniaxial mechanical testing was performed on the specimen entities to examine the chordae mechanics when interactions between the leaflet, chordae, and papillary muscle were preserved. Quantification of the chordae mechanics using this unique testing setup provides better insight into chordae mechanical behaviors.

(2) *Quantification of the collagen fiber architecture for the CT-leaflet insertion*

Polarized spatial frequency domain imaging (pSFDI) allowed for the quantification of load-dependent changes in the collagen fiber architecture of soft collagenous tissues. Using the leaflet-CT-papillary muscle entity, pSFDI was performed for the CT-leaflet insertion at various loading conditions, ranging from an unloaded state to a physiologically loaded configuration. The changes in the collagen fiber architecture in response to mechanical loads, *for the first time*, were quantitatively investigated, and the results from this study provided richer information about the connection of CT mechanics to the underlying collagen fiber microstructure.

The remainder of this thesis is organized as follows. Chapter 2 provides a literature review on the recent advancements in the mechanical characterizations of the AHV structures. In Chapter 3, the studies on the biaxial mechanical characterizations of the AHV leaflets are described, which include: (i) regionally-varied mechanics of the AHV leaflets, (ii) mechanics of the individual AHV leaflet layers, and (iii) AHV leaflet mechanical behaviors before and after the removal of the glycosaminoglycan contents. Chapter 4 describes the experimental procedure for the mechanical characterizations of the leaflet-chordae-papillary muscles entities. A study on the interrelationship between the collagen fiber architecture and the chordae-leaflet insertion mechanics is presented in Chapter 5. Chapter 6 concludes this thesis, alongside suggestions for future extensions based upon the works herein.

CHAPTER 2 – LITERATURE REVIEW

2.1 Overview of the Atrioventricular Heart Valve Anatomy and Function

2.1.1 The Atrioventricular Heart Valve Anatomy

The atrioventricular heart valves (AHVs) are referred as the mitral valve (MV) and the tricuspid valve (TV). As illustrated in **Figure 2-1**, the mitral valve, located between the left atrium and the left ventricle, is composed of two collagenous leaflets, namely the anterior leaflet (MVAL) and the posterior leaflet (MVPL) according to their anatomical locations. The tricuspid valve, on the other hand, resides within the right side of the heart, as organized by three leaflets: the anterior leaflet (TVAL), the posterior leaflet (TVPL), and the septal leaflet (TVSL). Comparing between the MV and the TV leaflets, the MV leaflets are generally thicker than the TV counterparts, likely owing to a higher pressure gradient experienced in the left side of the heart. AHV leaflets are affixed to a ring-shaped annulus and are supported in their functions by the chordae tendineae (CT) and the papillary muscles (PMs).

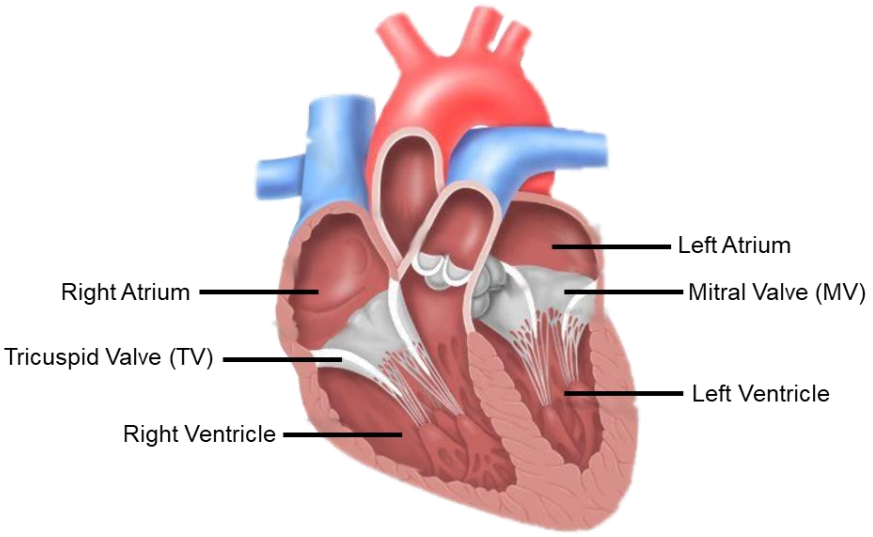

Figure 2-1. Schematic of the heart anatomy and the AHVs (image adapted from uptodate.com).

The CT of the AHVs have been morphologically categorized into three types, based on their insertion location to the valve leaflet. Specifically, those attaching to the free edge of the leaflet are considered the *marginal* chordae, ones attaching to the base of the valve are deemed the *basal* chordae, and the thicker CT attaching near the central belly region of the MVAL and TVAL are the *strut* chordae (**Fig. 2-2**). Furthermore, the string-like CT originate as a singular strand and would either split into three segments prior to the leaflet insertion or remain a singular structure.

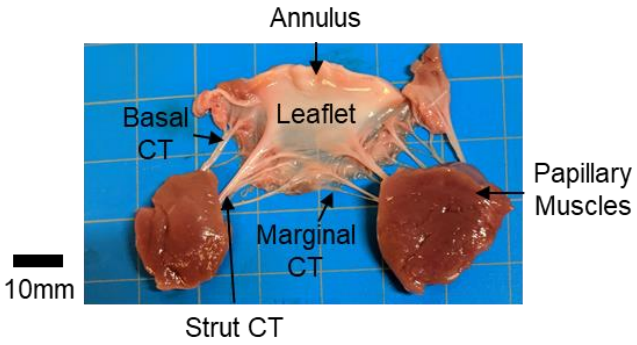

Figure 2-2. An excised porcine MVAL, illustrating the basal, strut, and marginal chordae.

2.1.1 The Atrioventricular Heart Valve Function

The AHVs are responsible for regulating a unidirectional flow of blood through the heart by means of cyclic opening and closing of the leaflets. The leaflets are supported by the CT during valve closing, during which the CT transfer systolic mechanical loads to the papillary muscles, preventing prolapse of the leaflet into the atria. In addition, the leaflets are anchored to the ring-shaped annulus, which acts as a hinge-like structure for the leaflets. Further, the annulus has been known to contract with the full beating motion of the heart [1]. Dysfunction of any of these sub-valvular components may result in the one-way blood flow being disrupted, and a backflow of blood can enter the atrium during systolic closure. This condition, known as heart valve regurgitation, will be further described in Section 2.2.

2.1.2 The Microstructure of the AHV Leaflets

The AHV leaflets have a complex microstructure that is made of collagen fibers, elastin fibers, proteoglycans (PGs), glycosaminoglycans (GAGs), and valve interstitial cells (VICs) [2, 3]. These microstructural components can be found in varying densities throughout the tissue thickness, resulting in a morphologically distinct layered structure. These tissues' layers are named, from the atrial side to the ventricular surface, as the atrialis (A), spongiosa (S), fibrosa (F), and the ventricularis (V). Each of these tissue layers is theorized to have its own function that collectively contributes to the overall mechanical behaviors of the AHV leaflets.

To elaborate, the atrialis layer is largely composed of radially-oriented elastin, collagen fibers, and GAGs, and is reported to have a higher innervation density [4]. The spongiosa layer is mostly made up of non-fibrous ground matrix, such as the GAGs and PGs, which acts to reduce the shearing forces between the atrialis and the fibrosa layers, as well as serving as a damping mechanism during rapid leaflet bending [5, 6]. The fibrosa is the thickest layer and is composed of a dense collagen fiber network oriented in the tissue's circumferential direction. These collagen fibers act as the primary load-bearing component of the AHV leaflet tissue. The ventricularis layer is mostly composed of circumferentially oriented elastin, providing the elastic response of the tissue. Within these four tissue layers are valvular interstitial cells that regulate and remodel the extracellular matrix (ECM). To elaborate, the VICs are contractile and respond to changes in strain conditions through coupled communication junctions [7], which allow for the coordinated secretion of the ECM components [8, 9]. For example, the VICs can increase GAG contents when subject to increased strain [10], or upregulate contractile filaments such as ACTA2 based on the changes in the mechanical environment [11]. Histological images of the microstructure of the three leaflets from a representative porcine TV are shown in **Figure 2-3**.

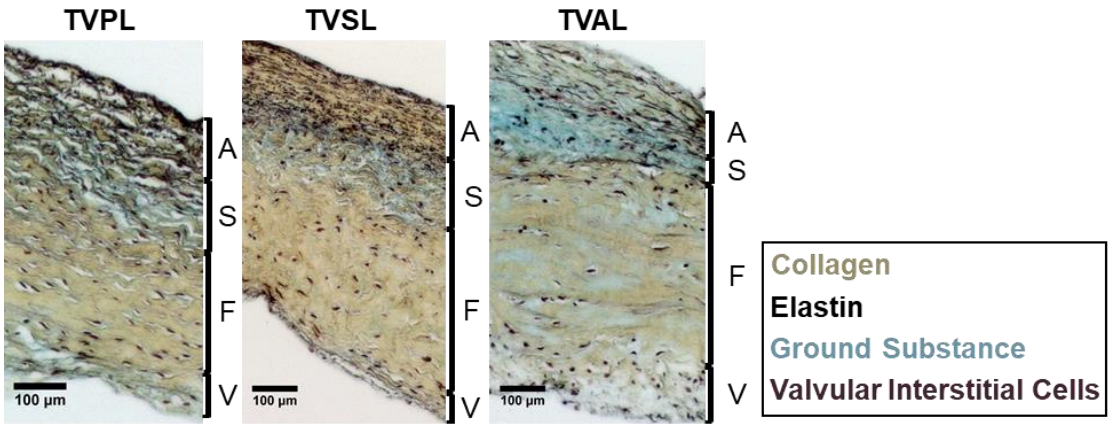

Figure 2-3. Micrographs of the porcine TV leaflets' microstructure using Movat's Pentachrome staining to highlight the elastin, collagen fibers, non-fibrous ground substance, and valvular interstitial cells. The four morphologically distinct layers are also illustrated in each image, i.e., A: atrialis, S: spongiosa, F: fibrosa, and V: ventricularis.

2.1.3 Mechanical Characterizations of the AHV Leaflets

Extensive studies in the AHV biomechanics society have elucidated the leaflet's mechanical properties by performing biaxial testing of the central, belly regions of the leaflets (**Fig. 2-4a** and **Fig. 2-4b**) [2, 12-24]. Owing to the unique and complex microstructure of the fibrous tissues of the AHV leaflets, biaxial mechanical testing is generally performed at various loading ratios of a targeted stress in each direction of the tissue (i.e., the circumferential and radial directions, see **Fig. 2-4a**). Coupling between the two directions of the tissue plays a critical role in the overall stress-stretch responses [25]. Moreover, the leaflet tissues exhibit repeatable cyclic mechanical response after the tissue has been preconditioned to restore their *in vivo* functionality [26], as is common in soft tissues biomechanics [27-29].

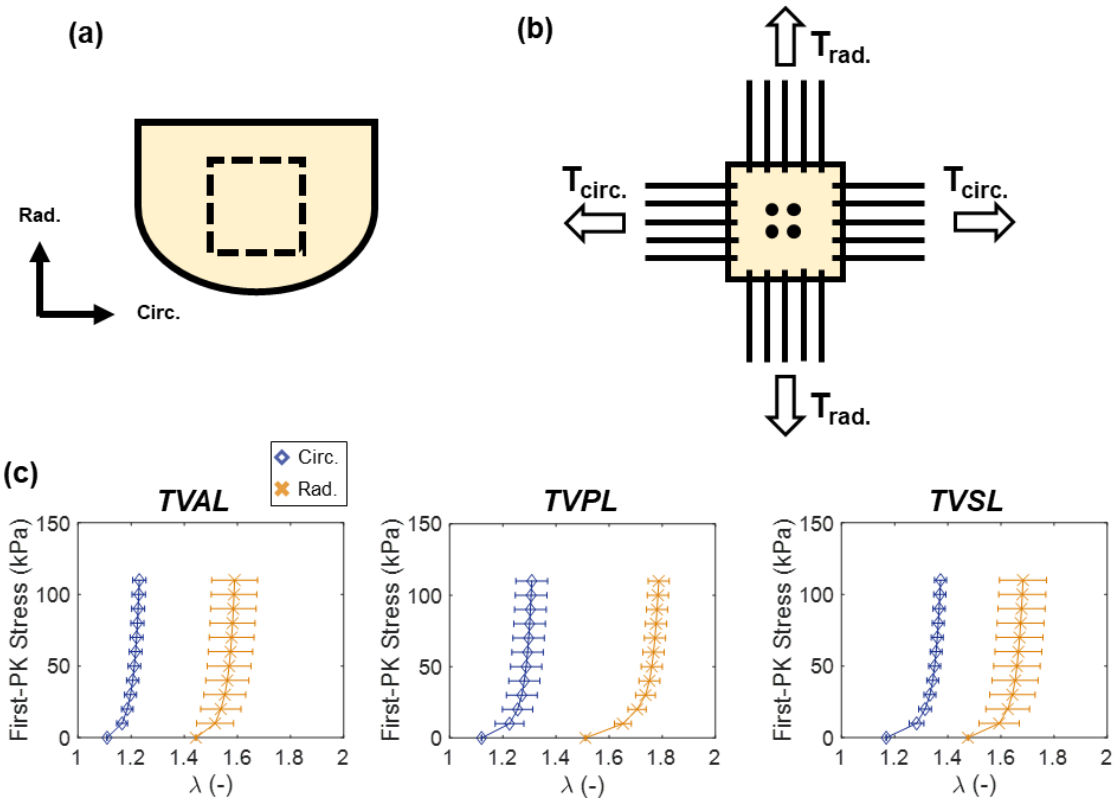

Figure 2-4. (a) Schematic of the excised leaflet tissue and the central bulk region taken for mechanical testing. (b) An illustration of the mounted TV leaflet tissue specimen onto the biaxial testing system with the collagen fiber orientations (i.e., the circumferential and radial directions) aligned with the testing *x*- and *y*-directions. (c) First-PK stress versus stretch results of the porcine TVAL, TVPL, and TVSL tissues (n = 6) under equibiaxial loading (F_x:F_y = 1:1). Results are presented in mean ± SEM. Images were modified from Jett *et al.* (2018) [12].

Several key findings from these biaxial mechanical testing studies of the AHV leaflets are summarized as follows. First, the AHV leaflets have an anisotropic and J-shaped non-linear mechanical response, with the tissue's radial direction being generally more extensible than the circumferential direction. For example, in Jett *et al.* (2018) [12], the porcine TVAL tested to a 115 kPa equibiaxial stress was found to have a circumferential strain of ~22% and a radial strain of ~73%. Secondly, the mechanical properties differ between the three TV leaflets, with the greatest

extensibility and the greatest anisotropy generally observed in the TVPL (**Fig. 2-4c**). Similar trends were observed for the MV leaflets, with the MVPL being more extensible than the MVAL [12]. Moreover, Pham *et al.* (2017) [30] tested human AHV leaflets at the following equibiaxial stresses: MVAL, 70 kPa; MVPL, 40 kPa; TVAL, 70 kPa; TVPL, 70 kPa; and TVSL, 80 kPa. From this testing, they reported circumferential strains of 10%; 13%, and 10% for the TVAL, the TVPL, and the TVSL, respectively, whereas the radial strains were found to be generally larger, i.e., the TVAL: 17%, the TVPL: 22%, and the TVSL: 20%. Thirdly, studies have demonstrated that the leaflets' mechanical responses have a slight dependence on the loading rate. In Jett *et al.* (2018) [12], the leaflets were tested at 2.29 N/m, 4.42 N/m, and 7.92 N/min loading rates, and only a ~7% difference was observed in the tissue strains under physiological loading. Further, Grashow *et al.* (2006) [22] tested the MVAL at physiologic strain rates *in vitro* and found similar strain rate insensitivity at or below the physiologic loading conditions. Fourth, the AHV leaflets possess a profound stress–relaxation behavior [12, 31].

The above-mentioned anisotropic, non-linear nature of the AHV leaflet's mechanical response stems from the gradual straightening (uncrimping) of the collagen fibers that are preferentially oriented in the tissue's circumferential direction. Following the uncrimping is recruitment, including reorientations of the collagen fibers to bear loading in different directions. Since the crimped collagen fibers do not significantly contribute to the mechanical behavior, the tissue's mechanical response initially has a toe-region in which there are large deformations and low stresses [32]. As the collagen fibers are recruited and straightened, the tissue's mechanical response stiffens, resulting in the distinct non-linearity. The load-dependent changes in orientation, recruitment, and re-orientation of the collagen fibers in the leaflet has been determined by different imaging techniques [33-35]. For example, Liao *et al.* (2007) used an integrated small angle X-ray

scattering and biaxial testing device and quantified the straightening and reorientation of the collagen fibers in the MV anterior leaflet under equibiaxial tension, creep, and stress relaxation [36].

2.1.4 Microstructure of the AHV Chordae Tendineae

The CT are primarily composed of collagen fibers surrounded by an elastin sheath. Specifically, the CT have been described as having five distinct layers, (from outermost to innermost): (i) a layer of endothelial cells, (ii) an elastin sheath with fibers oriented at inclined angles to the longitudinal axis, (iii) a longitudinally-oriented elastin sheath, (iv) collagen fibers aligned circumferentially in planar waves, and (v) a core of straight collagen fibers with longitudinal elastic fibers sparsely dispersed throughout (**Fig. 2-5**, **Fig. 2-6**, and **Fig. 2-7**) [37].

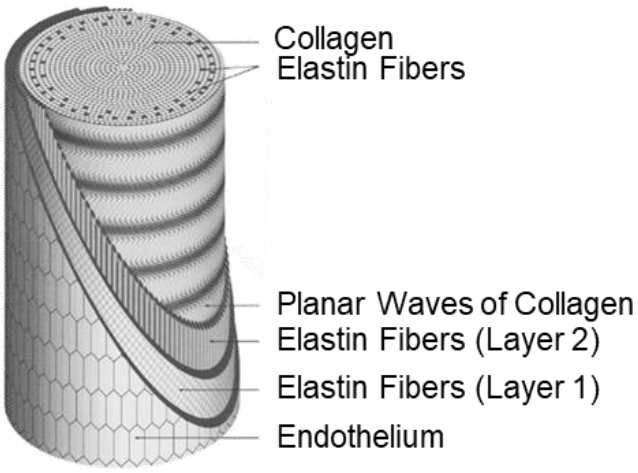

Figure 2-5. Schematic of the chordae tendineae microstructure (image from Millington-Sanders *et al.* (1998) [37]).

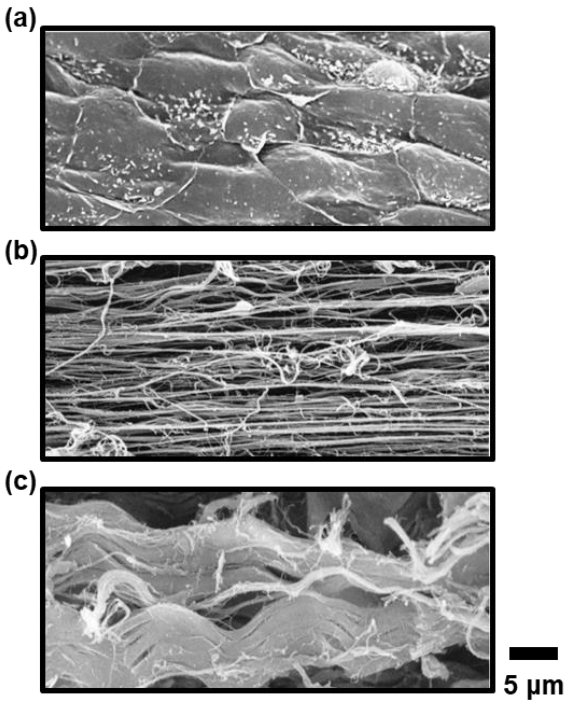

Figure 2-6. Scanning electron micrograph of (a) external endothelial cells, (b) elastin fibers, and (c) collagen fiber waves of the chordae (image from Millington-Sanders *et al.* (1998) [37]).

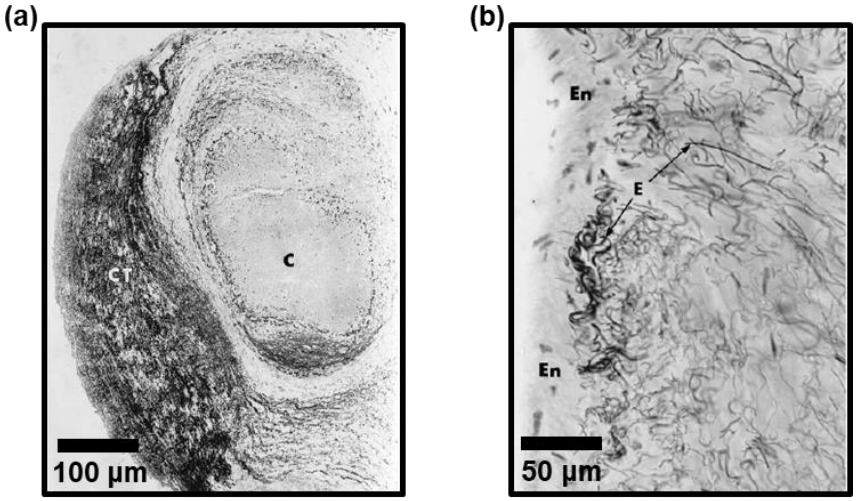

Figure 2-7. (a) A micrograph of a cross-section of the CT, showing the collagen core (C) and connective tissues (CT). (b) Within the connective tissue cushion, a disorganized network of elastin fibers (E) and endothelium (En) exists (image from Millington-Sanders *et al.* (1998) [37]).

It is worth noting that differences have been observed in the human and the porcine CT microstructure. To elaborate, Ritchie *et al*. (2005) histologically examined porcine MV chordae, and they did not observe the distinct elastin layer found in Millington-Sanders *et al.* (1998), which could be attributed to a difference in species [37, 38]. Additionally, the porcine CT have been found to contain blood vessels that connect from the leaflet to the papillary muscles, supplying the leaflet with essential nutrients [39], but these results have not been validated for human CT.

Another integral part of the chordae microstructure is the CT-leaflet insertion, where the highly aligned collagen fibers of the chordae transition into the more complex collagen fiber architecture of the leaflets (**Fig. 2-8**). It is possible the differences in the microstructure at the chordae-leaflet insertion, such as in the orientation and crimping, could manifest as differences in the mechanics when compared to analyzing purely the leaflet or the chordae. Chen *et al*. (2004) studied the strut CT-leaflet insertions of porcine MVs and found that collagen fibers in the leaflet closer to the annulus were more circumferentially aligned, and that the collagen fibers became more radially aligned and uniform approaching the leaflet-chordae transition [40]. Similarly, the CT-papillary muscle insertion has also been examined, and it was found that both human and porcine chordae exhibited a smooth, continuous endocardium endothelium between the CT and the PMs [41]. However, across-species differences were observed in the collagen fiber connection to the muscle, with human hearts being more organized and porcine hearts being more random in the collagen fiber architecture.

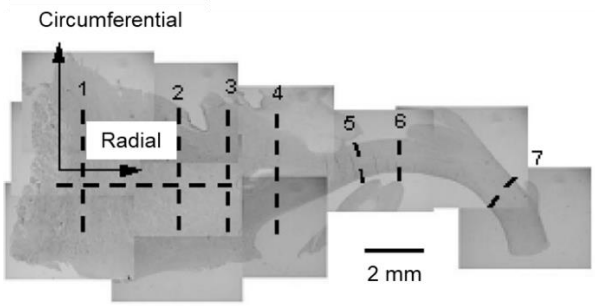

Figure 2-8. Digital microscopic image of the mitral valve strut chordae-leaflet insertion (from Chen, *et al.* (2004) [40]). Dotted lines correspond to imaging locations used for quantifying the fiber angle.

2.1.5 Mechanical Characterizations of the Chordae Tendineae

Research advancements have been made to investigate the mechanical properties of the chordae tendineae through methods including: (i) uniaxial tensile testing, (ii) stress-relaxation testing, (iii) CT-leaflet insertion testing, and (iv) *in vitro* flow loop testing (**Fig. 2-9**).

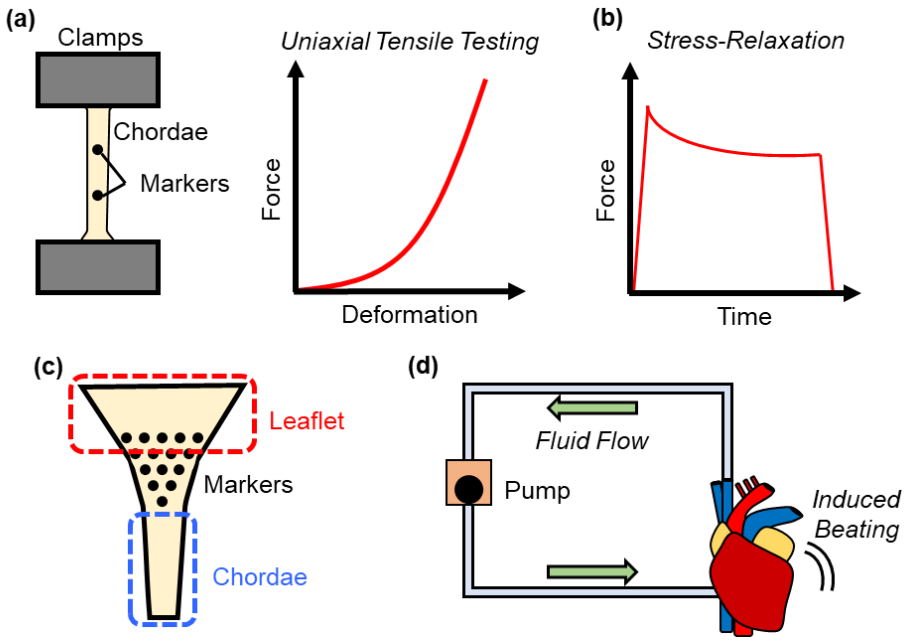

Figure 2-9. Various mechanical characterization methods for the AHV chordae tendineae: (a) uniaxial mechanical testing, (b) stress-relaxation testing, (c) CT-leaflet insertion deformation tracking, and (d) *in vitro* heart-simulating flow loops.

The most prevalent method for investigating the chordae mechanics is through uniaxial tensile testing. In these studies, generally chordae are fully separated from their valve attachments and placed into a hydraulic uniaxial tensile testing machine (**Fig. 2-9a**). Then, chordae are preconditioned, followed by either cyclic force loading and unloading to a target load, or loading until tissue rupture. Pokutta-Paskaleva *et al.* (2019) [15] characterized porcine MV and TV chordae and observed that the strut chordae were stiffer than the marginal and basal chordae, that the basal chordae had greater extensibilities than the marginal chordae, that the MV chordae were stiffer than the TV counterparts, and that the chordae attaching to the TV septal leaflet were more extensible than the chordae connected to other TV leaflets (**Fig. 2-10**).

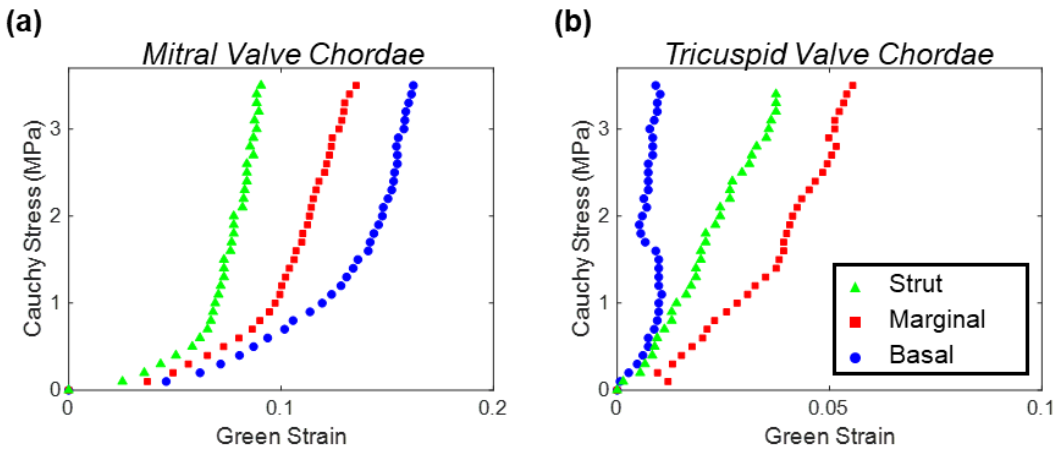

Figure 2-10. Results from uniaxial mechanical testing by Pokutta-Paskaleva *et al*. (2019) [15] for characterizing the strut, marginal, and basal CT from: (a) the MVAL, and (b) the TVAL.

To supplement the information on the chordae uniaxial tensile characteristics, Liao and Vesely (2004) performed stress-relaxation testing of porcine MV chordae [42]. In this study, they loaded tissues to the displacement associated with an initial 150 g load and observed the stress-relaxation behaviors over 100 seconds (**Fig. 2-9b**), and found that the strut chordae possess the fastest and greatest relaxation behavior (49.1±5.4%), followed by the basal chordae (42.4±8.3%), and then the marginal chordae (33.2±4.7%).

Moreover, there have been a couple of studies in literature focused on the mechanics of the CT-leaflet insertion. Padala *et al*. (2010) [43] investigated the porcine MV strut chordae using an *in vitro* flow loop in conjunction with optical marker tracking across the surface of the insertion region (**Fig. 2-9c**). From this experimental setup, they found that the edges of the insertion region stretched more than the center of the MV leaflet. Ritchie *et al*. (2006) [44] performed a similar study using the Georgia Tech left heart simulator in conjunction with a marker-tracking approach to analyze the porcine MV strut chordae response to a simulated cardiac cycle. They found that during valve closure chordae experienced a strain rate of 75.3±3.43% strain per second, and during

opening the strain rate was -54.8±-56.6% strain per second. Furthermore, there was a constant plateau of chordae strain between 3.75% and 4.29% during valve closure.

Chen *et al*. (2004) [40] also examined the porcine MV strut chordae insertion using a biaxial testing system. In their testing, they fixed the leaflet on three edges via suture hooks, and on the fourth edge attached the chordae to a string. From optical tracking of fiducial markers across the surface of the CT-leaflet insertion, they found that approaching the MV strut CT-leaflet insertion the radial extensibility of the tissue decreased while the tangent modulus increased.

2.2 Heart Valve Regurgitation

In the case of subvalvular component dysfunction, such as heart valve disease, a regurgitant jet of blood can form in the atria during systolic closure, causing a deficiency of blood in the ventricle (**Fig. 2-11**). The deficiency of blood can lead to an overworking of the heart and eventual heart failure. Examples of heart valve disease that can lead to regurgitation include tissue calcification, annular dilation, leaflet stenosis, chordae elongation, and chordae rupture. The severity of the regurgitation determines the severity of the associated surgical correction.

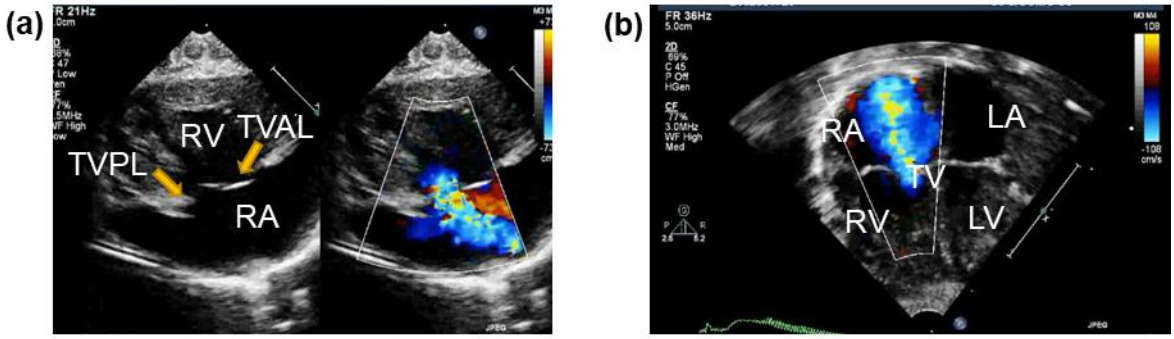

Figure 2-11. Visualization of severe tricuspid regurgitation using two different 2D transthoracic echocardiography views and color flow Doppler: (a) a parasternal long-axis inflow view, and (b) an apical four-chamber view of a newborn with a severe pulmonary hypertension due to diaphragmatic hernia. (Images provided by Drs. Mir and Burkhart at the OUHSC)

2.2.1 Clinical Treatment of Valvular Regurgitation

In situations where the valve has maintained a majority of the tissue's physiologic integrity, such as annular dilation, surgical repair often follows as the installation of an annuloplasty ring or the mitral clip [45, 46]. The annuloplasty ring approach uses a soft-plastic device sutured to the valvular annulus with the goal of restoring the annulus geometry for more coaptation and full closure of the leaflets. While this treatment option has been shown to be successful, it is an open-heart procedure with an undesirable recurrence rate of approximately 15%-20% within 3-5 years after the initial operation [47-49]. Alternatively, the mitral clip offers a suitable non-open-heart treatment for the MV where the two leaflets are clipped together. Despite its short- and mid-term success, it can be difficult to attach the clip appropriately, sometimes requiring re-operation for additional clips [50].

In more severe scenarios where the valve's structural function is significantly damaged, including severe valvular stenosis and leaflet calcification, treatment requires replacement of the

valve by a mechanical or biological prosthesis. Mechanical valves are made of metals, ceramics, or polymers, which require undesirable life-long anticoagulant prescriptions to prevent thromboembolism. In contrast, bioprosthetic valves, constructed of grafted porcine or bovine tissues, require no anticoagulant treatment, but often suffer from degeneration issues and require reoperation within 15 years for 40% of patients [51-54].

Specific to the CT tissues, several surgical techniques have been employed including chordal shortening, chordal transposition, and chordal replacement, each with their own limitations. For example, chordal shortening may not always yield the optimal treatment results [55]. Chordal transposition provides a desirable mid-term (from 18-82 months) freedom from reoperation, but still requires further investigations to confirm its effectiveness [56]. Additionally, chordal replacement utilizes expanded polytetrafluoroethylene (ePTFE) to replace the chordae tendineae. This technique is advantageous as it is minimally invasive with an excellent recurrence rate of 1.4% at 3.5 years; however, in the long-term, recurrence can occur due to excessive elongation of the suture, or rupture of the native chordae tendineae [57, 58]. To elaborate, the elastic moduli of ePTFE sutures are significantly larger than those of native chordae tendineae, which may lead to recurrent leaflet prolapse [59]. Improvement of surgical therapeutics to reduce issues of disease recurrence relies on a better understanding of the tissue mechanics of native chordae tendineae.

The various shortcomings and undesirable outcomes of heart valve disease therapeutics provides a clear demonstration of the need for patient-specific surgical planning using detailed simulation tools, and consequently a better understanding of the native valve tissue mechanics.

2.3 Purpose of the Thesis

Refinements to address limitations of current AHV therapeutics can be guided through the development of simulation tools utilizing the experimentally acquired mechanical and

microstructural properties of the valve tissues. The development of such simulation tools could also lead to patient-specific diagnoses and treatments – a promising topic in current AHV biomechanics literature [60-62]. However, the refinement of current therapeutics and the development of highly accurate patient-specific computational models are reliant on a thorough and detailed understanding of the AHV leaflets and chordae tendineae. To elaborate, for the AHV leaflets there is lacking information regarding heterogeneities in the mechanical properties, such as in different regions across the tissue, or through the tissue thickness. Furthermore, there is very limited information on the contributions of the leaflets' microstructural components to the overall leaflet behaviors. To better highlight the necessities of such investigations, there have been extensive studies on the aortic valve cusps and leaflets, and some other elaborate studies on the mitral valve leaflets, but the tricuspid valve leaflets have not been as thoroughly examined. On the other hand, information on the chordae tendineae mechanics are lacking in current literature, such as the effects of different boundary conditions during *in vitro* testing on the observed mechanical properties, or a detailed understanding of the load-dependent collagen fiber microstructure of the CT-leaflet insertion.

The overall objective of this thesis is to provide a more detailed understanding of the leaflet and chordae tendineae biomechanics, addressing the current gaps in AHV biomechanics knowledge. Through the presented studies on the AHV leaflet mechanical properties, the chordae tendineae tensile characteristics, and the CT-leaflet insertion microstructure-mechanics relationships a more detailed understanding of the AHV biomechanics has been developed. The findings from these works will allow for unique insight to the valvular components' behaviors and lead to further refinement of AHV computational models for improved therapies.

CHAPTER 3 – BIAXIAL MECHANICAL CHARACTERIZATIONS OF AHV LEAFLETS

In the previous literature, focus has largely been on the biaxial mechanical characteristics of the central, belly regions of the bulk AHV leaflets [14, 15, 19]. In these studies, mechanical loading is applied to the tissues in two directions (i.e., the circumferential and radial directions) to emulate physiologic conditions. The findings from the material characterizations are useful for simulation tools that can predict the tissues' behaviors *in vivo*. However, many of these studies, and consequently the computational models, do not consider the complex mechanical behaviors of the AHV leaflet tissues, including the spatial variations, layer-specific mechanics, or microstructure-mechanics relationships. To advance the knowledge in the AHV biomechanics field, experiments are warranted to quantify these complex leaflet stress-stretch behaviors.

This chapter summarizes the works pertaining to characterizing the mechanical behaviors of the AHV leaflets. Specifically, the studies include: (i) investigation of the regionally varying mechanics of the MV and TV anterior leaflets; (ii) mechanical characterizations of individual tissue layers of the AHV leaflets; and (iii) quantifications of the contributions of glycosaminoglycans to the AHV leaflet behaviors. The remaining of this chapter is organized as follows. The biaxial mechanical testing procedures are described in Section 3.1. Section 3.2 presents the results of those mechanical characterization studies. The key findings and the implications of the results for the AHV biomechanics field are provided in Section 3.3.

3.1 Methods

3.1.1 Tissue Acquisition and Preparation

Healthy, adult porcine hearts (80-140 kg, 1-1.5 years of age) were obtained from a local USDA-approved slaughterhouse (Country Home Meat Co., Edmond, OK). Hearts were obtained on the same day of excision from the animal, promptly cleaned of clots, and placed in a freezer at -14 °C. This freezing-based storage procedure was adopted according to the previous studies, which demonstrated a minimal effect of freezing on the mechanical properties of collagenous tissues [63-65]. For dissection, hearts were thawed, and the MV and TV anterior leaflets were excised (**Fig. 3-1a** and **Fig. 3-1b**).

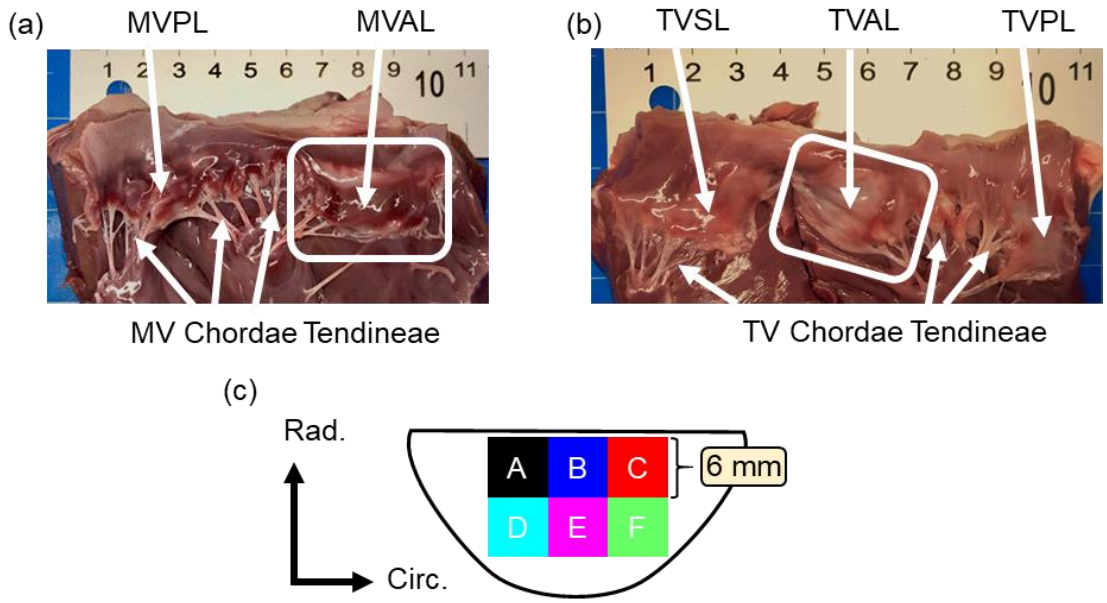

Figure 3-1. Dissected porcine hearts showing: (a) the mitral valve, and (b) the tricuspid valve with the anterior leaflet highlighted for both atrioventricular heart valves. (c) Schematic of a valve anterior leaflet with the six smaller delimited regions.

For the study on the regional variations, leaflets were further sectioned into six smaller regions, each of 6x6mm dimension (**Fig. 3-1c**): regions B and E as the *central* regions, and regions

A, C, D, and F as the *edge* regions. For the investigation on layer-specific mechanics, a microdissection was performed, as described in Section 3.1.2, with the resulting specimen size being approximately 4x4mm. For the study on the GAG contributions, AHV leaflet tissues were sectioned into 10x10mm specimens. The sectioned tissue samples were then stored in phosphate-buffered saline (PBS) solution and refrigerated at 4 °C for up to two days before mechanical testing.

3.1.2 Microdissection of the AHV Leaflets

For AHV leaflet microdissection, only two layers were segmented for the TVAL (A/S: combined atrialis-spongiosa layer, and F/V: combined fibrosa-ventricularis layer), due to the tissue's relatively smaller thickness and the unique structure, whereas it was possible to separate the MVAL into three tissue layers (A/S: atrialis/spongiosa; F: fibrosa; V: ventricularis). In brief, an intact leaflet was mounted on a wax dissecting pan (American Educational Products LLC), oriented with the atrialis facing upwards. The perimeter of the leaflet was tautly stretched and fastened to the wax tray by means of six 9/16" head T-pins (Eisco Labs). Once secured, two delicate incisions were made along the leaflet's central belly region, penetrating only the upper layer (**Fig. 3-2**). Dissecting forceps were used to gently pull against the severed atrialis/spongiosa, exposing the fibrillar interconnections, and bisecting the atrialis and fibrosa. These chords contained within the spongiosa were trimmed using ophthalmic scissors. After obtaining a ~4x4mm section, the layer was detached from the remaining bulk tissue. To perform the MVAL ventricularis micro-dissection, the tissue was flipped over (ventricularis-up) and remounted to the tray. The initial procedure was then repeated to obtain the MVAL ventricularis. After the atrialis/spongiosa and the MVAL ventricularis were removed, a square specimen of the exposed

fibrosa was excised from the bulk leaflet. Additionally, a strip of an intact tissue (~2x0.5mm) from above the dissected region was removed and stored as a baseline for histological comparison.

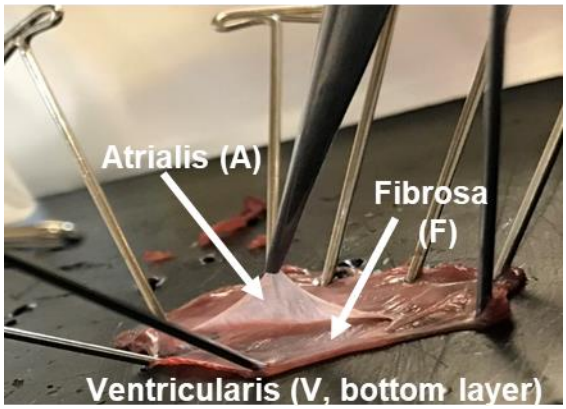

Figure 3-2. Microdissection process for an MVAL tissue, showing the atrialis layer first separated from the remaining tissue. 9/16" head T-pins were used to fasten the tissue on a wax tray.

3.1.3 Tissue Sample Preparation for Biaxial Mechanical Testing

At the time of testing, the tissues' thicknesses were recorded at three locations using a digital caliper (Westward 1AAU4 – 0.01mm resolution) and averaged. The specimen was then mounted, with an effective testing region (i.e., the separation distance between two BioRakes, see **Fig. 3-3a**), onto a commercial biaxial mechanical testing system (BioTester, CellScale Biomaterials Testing, Canada) equipped with 1.5N load cells. For the regional variations study the effective testing size was 4x4mm; for the layer-based study the effective testing region was 3.5x3.5mm; and for the GAG contributions investigation the effective testing region was 7x7mm prior to treatment and 5x5mm after treatment (see Section 3.1.4). The circumferential and radial directions of the tissue specimen were aligned with the testing *x*- and *y*-directions. Four fiducial markers were then placed in an array on the central region of the tissue for optical tracking-based strain calculations

(see Section 3.1.6**)**. During testing, the tissue was submerged in a 37 °C PBS bath to emulate physiological conditions.

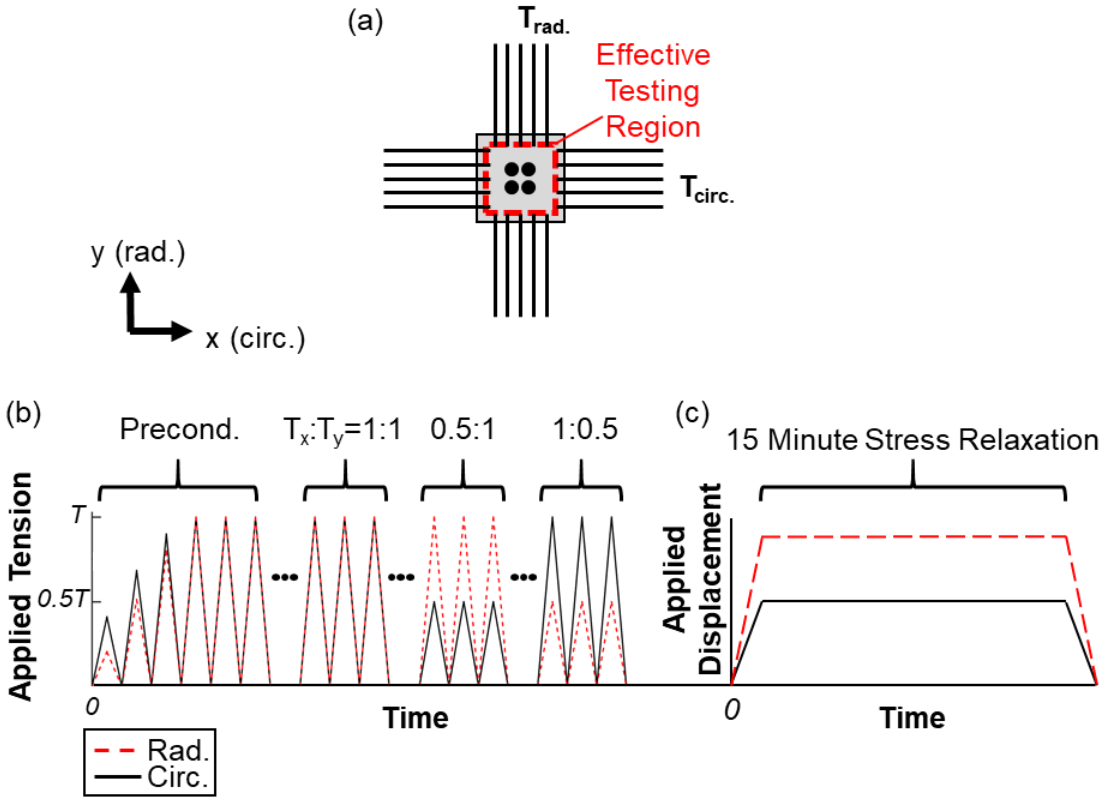

Figure 3-3. (a) Experimental setup for biaxial mechanical testing of the MVAL and TVAL tissue specimens. Schematic of the testing procedures: (b) force-controlled biaxial testing protocol, and (c) biaxial stress relaxation testing protocol.

3.1.4 Biaxial Mechanical Testing

The mechanical properties of the MV and TV leaflets were characterized using the BioTester biaxial mechanical testing system. In the regional and layer studies , maximum applied membrane tension in the circumferential and radial directions ($T_{circ,\max}$ and $T_{rad,\max}$) of 100 N/m and 50 N/m were used for the MVAL and TVAL, respectively [14, 20]. For the GAG study, the targeted membrane tensions were 100 N/m and 75 N/m for the MVAL and TVAL, respectively. Here,

$T_{circ,\max}$ and $T_{rad,\max}$ are the maximum membrane tensions in the circumferential and radial directions, respectively, which were calculated based on each AHV's physiological pressure gradient, i.e., 100 mmHg for the MV and 40 mmHg for the TV [14, 20, 66], respectively, and the tissue's effective testing edge length.

A two-step force-controlled biaxial testing procedure was used to characterize the mechanical behavior of the tissue specimens (**Fig. 3-3b**). First, a preconditioning protocol was used to restore the valve leaflet to its *in vivo* configuration, in which $T_{circ,\max}$ and $T_{rad,\max}$ were applied in each direction at a rate of 2.29 N/min for 8-10 repeated loading/unloading cycles, with a preload of 2.5% of $T_{circ,\max}$ and $T_{rad,\max}$. Next, five varying loading ratios ($T_{circ,\max}:T_{rad,\max}$ = 1:1, 0.75:1, 1:0.75, 0.5:1, and 1:0.5) were employed with 8-10 loading/unloading cycles to investigate possible physiological tissue deformations. Throughout the test the BioRake separation distance, load-cell force readings, and a series of 1280x960 images, using a high-resolution CCD camera, were collected at 15 Hz. Data from the last cycle of each loading protocol were used in the tissue stress and strain analyses.

In addition, a biaxial stress-relaxation test was performed to characterize the stress decaying response (**Fig. 3-3c**). For this testing, tissue specimens were loaded to $T_{circ,\max}$ and $T_{rad,\max}$, and the specimens were then held at the associated displacements to relax over 15 minutes. The force readings were retrieved at a rate of 5 Hz for the subsequent stress reduction analysis.

For quantifications of the GAG contribution to the overall leaflet's mechanical behavior, a sequential biaxial mechanical testing procedure was performed, including: (i) control testing ─ biaxial mechanical testing of the untreated (control, denoted by -C) MVAL or TVAL specimen with an effective testing region of size 7x7mm; (ii) GAG degradation – enzymatic removal of

GAG contents with the tissue specimen unmounted from the biaxial testing system; (iii) post GAG-removal testing – biaxial mechanical testing of the enzyme-treated specimen (denoted by -T) with an effective testing region of size 5.5x5.5mm to avoid interference with BioRake insertion points from previous mounting.

3.1.5 Tissue Strain and Stress Calculations

The time-dependent locations of the four applied fiducial markers were determined through analysis of the acquired images using the data-image correlation (DIC) functionality in the LabJoy software of the BioTester system. Then, the four fiducial markers were considered as a four-node bilinear finite element to compute the deformation gradient **F** through

$$\mathbf{F} = \mathbf{F}(\mathbf{X}, t) = \frac{\partial \mathbf{x}}{\partial \mathbf{X}} = \begin{bmatrix} \sum_{I=1}^{4} B_{XI} u_I(t) & \sum_{I=1}^{4} B_{YI} u_I(t) \\ \sum_{I=1}^{4} B_{XI} v_I(t) & \sum_{I=1}^{4} B_{YI} v_I(t) \end{bmatrix} \tag{3.1}$$

where B_{XI} and B_{YI} are the shape function derivatives for node I, and u_I and v_I are the displacements of node I in the x- and y- directions, respectively. The stretches in each direction were computed by taking the square roots of the principle values of the right Cauchy deformation tensor $\mathbf{C} = \mathbf{F}^T\mathbf{F}$ and the membrane tension was then computed by

$$diag[T_{circ}, T_{rad}] = \frac{1}{L} diag[f_C, f_R] \tag{3.2}$$

where f_C and f_R are the recorded forces in the circumferential and radial direction, respectively, and L is the effective edge length. Various stress measures can be readily computed for making comparisons with tissue stress results in other studies using the membrane tension values and the specimen's thickness: $\mathbf{P} = diag[P_{CC}, P_{RR}] = diag[T_{circ}, T_{rad}]/t$, $\mathbf{S} = \mathbf{F}^{-1}\mathbf{P}$, and $\boldsymbol{\sigma} = J^{-1}\mathbf{P}\mathbf{F}^T$ [67, 68]. Here, **P** is the first Piola-Kirchhoff stress tensor, **S** is the second Piola-Kirchhoff stress tensor, **σ** is

the Cauchy stress tensor, and J = det(**F**) is the Jacobian of **F**. Finally, an anisotropy index (*AI*), defined as the ratio of the peak stretch in the radial direction to the circumferential stretch, i.e., $AI = \lambda_{rad}^{0\text{-}peak} / \lambda_{circ}^{0\text{-}peak}$, was used to make quantitative evaluations of the material anisotropy.

For analyses of the stress decaying responses from stress relaxation testing, force readings were converted to membrane tensions. The reported membrane tension values were then normalized by the peak values with respect to each tissue's direction for evaluating the percent relaxation (i.e., stress reduction) over the 15-minute duration.

3.1.6 Enzymatic Treatment of AHV Leaflets for Removing Glycosaminoglycans

To examine the GAG contributions to AHV leaflet tissue mechanics, force-controlled and stress-relaxation biaxial mechanical tests were performed prior to and after an enzyme-based GAG degradation procedure previously developed for the aortic valve cusps [5]. In brief, an enzyme solution consisting of 30 Units/mL of the enzyme Hyaluronidase type VI-S and 0.6 Units/mL of the enzyme Chondroitinase ABC from Proteus vulgaris (Sigma Aldrich #H3631 and #C3667) in a 100 mM Ammonium Acetate Buffer Solution (AABS, Sigma Aldrich #A1542) was prepared with an adjusted pH of 7.0. The MVAL or TVAL tissue specimen was placed in a 1.5mL microvial tube filled with the prepared GAG-degradation solution and continuously shaken (H5000-H MultiTherm Shaker, Benchmark Scientific, Sayreville, NJ) for the optimal enzyme-treatment time (as described below) at 37 °C (**Fig. 3-4**). The enzyme solution was then removed, and the leaflet tissue specimen was washed with ice-cold PBS three times, for five minutes each time.

An intermediate study was first conducted to determine the optimal enzyme treatment time, which was considered as the balance between the degraded GAGs (>50%) and the experimental time. Briefly, porcine MVALs and TVALs were sectioned into tissue strips (**Fig. 3-4a**), with one strip from each untreated leaflet serving as the control and all other tissue strips subjected to the

enzymatic GAG degradation procedure. Tissue strips were continuously shaken in the enzyme degradation solution with one tissue strip from each leaflet removed every 20 minutes until a final time point of 160 minutes (**Fig. 3-4b**). After all tissue strips had been treated and PBS-washed, histological analysis was then performed (see Section 3.1.7) to quantify the percentage of GAGs remaining at each time point. This optimal treatment time of 100 minutes, determined by the GAG content quantification as described in Section 3.1.7, was used in the subsequent biaxial testing procedures.

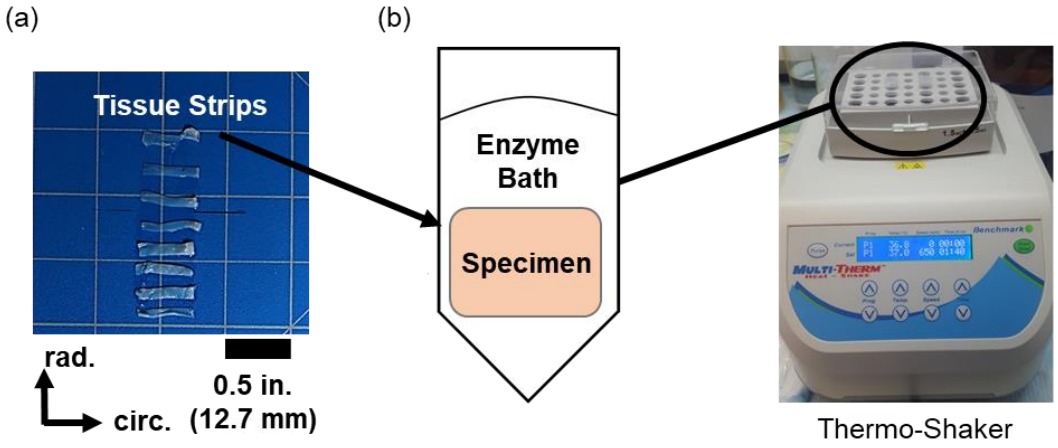

Figure 3-4. Schematic of the enzyme-based GAG removal treatment: (a) tissue strips of the MVAL or the TVAL used for determination of optimal treatment; (b) tissue specimen (either the tissue strip used for histology, or the square tissue used for biaxial mechanical testing) in a 3mL vial with a warm enzyme bath.

3.1.7 Histological Verification for Layer Separation and GAG Content Quantification

To confirm the accuracy of the employed microdissection method and to quantify the tissue's microstructure, histology was used. All tissues were fixed in 10% formalin at room temperature (23 ºC), embedded in paraffin wax, and sectioned (5-7 μm). For the layer-based study, Movat's Pentachrome stain was selected based on its ability to reveal comprehensive information about the

microstructural organization: elastin stains *purple*, collagen stains *yellow*, and ground substance stains *blue*. The stained sections were viewed under a halogen illumination microscope (Olympus, Waltham, MA, USA). For the layer-based study a 4X magnification was used for the intact tissues and a 10X magnification was used for the separated layers, with a single image acquired from each of the stained tissues. The microstructural ECM components—collagen, elastin, and ground matrix substance—were quantified by volume in accordance with previous studies [69, 70] utilizing the ImageJ (National Institute of Health, Bethesda, MD, USA) color deconvolution method [70, 71]. For each histological image, three measurements of the tissues' thickness and constituent percentages were made and analyzed. These three measurements were then averaged. It is noted that the tissue strip analyzed for the intact MVAL/TVAL was a different tissue strip from the layer-separated tissue but was still from the same leaflet.

To visualize and identify GAG contents Alcian blue staining was used in the GAG-removal study [6, 72]. Four images were acquired for each tissue, in which a 4X magnification was used for the MVAL tissues, while a 10X magnification was used for the TVAL tissues. The percent GAG content value was then found and averaged for the four images at each time point to account for regional variances within the tissue strip. The percent GAG content at each time point was then compared to the untreated (control) sample, taken from the same leaflet, to determine the percent GAG reduction. The optimal treatment time was determined when the majority of the leaflet's GAG content (>50%) had been removed, and further treatment did not result in a significant degradation of the GAG content. Additionally, the tissue thickness was determined for each image and averaged at each time point.

3.1.8 Statistical Analysis

To determine statistically significant differences in the regional responses of the tissues (n=10-13, dependent on region), one-way Analysis of Variance (ANOVA) was performed using an in-house MATLAB program to analyze the *total tissue stretch* values associated with the peak applied membrane tension ($\lambda_{circ}^{0\text{-}peak}$ and $\lambda_{rad}^{0\text{-}peak}$) between regions from the same valve leaflet. In the layer investigation, the non-parametric Mann-Whitney *U* test was used to determine statistical differences for the leaflet layers (n=6 for each) from the same valve tissue. For determining statistically significant differences in tissue mechanics due to GAG removal, a non-parametric Mann-Whitney *U* test was performed to determine statistically significant differences between the control and enzyme-treated groups of both the MVAL (n=7) and TVAL (n=6) tissue specimens. It is important to note that comparisons were not made between the MVAL and TVAL tissues in any of the studies, as different peak membrane tensions were targeted for each tissue. The null hypothesis for our statistical analyses was that the mean of the difference between the two groups had a value of zero, e.g., GAG removal had no statistically significant effect on the tissue mechanics.

For quantitative interpretations of our statistical analysis results, the peak stretch value was further broken into two parts as described in our previous work [12]: *(i)* the *preconditioning stretches* (λ_{circ}^{0-1} and λ_{rad}^{0-1}), which are defined as the tissue deformations due to the preconditioning effect, and *(ii)* the *mechanical stretches* ($\lambda_{circ}^{1\text{-}peak}$ and $\lambda_{rad}^{1\text{-}peak}$), corresponding to the tissue deformation in response to mechanical loading with respect to the post-preconditioning configuration. All analyses were performed with $p<0.05$ considered as *statistically significant*, and $p<0.1$ considered as *nearly statistically significant*. All results are reported as mean ± standard error of the mean (SEM).

3.2 Results

3.2.1 Results from the Regional Investigation

For examining the regional variations in leaflet mechanics, three main trends were observed for all loading ratios ($T_{circ,\max} : T_{rad,\max}$ = 1:1, 0.75:1, 1:0.75, 0.5:1, and 1:0.5) (**Fig. 3-5** and **Fig. 3-6**). First of all, we found that the central regions had a greater difference in the peak stretch between the circumferential and radial directions than the edge regions for both the MVAL (region B: p=0.034, region E: p=0.017) and the TVAL (region B: p=0.162, region E: p=0.189). Secondly, by analyzing the anisotropy index, the central regions were more anisotropic than the edge regions for the MVAL (statistically significant difference for the comparisons B vs. A: p=0.016, B vs. C: p=0.01, and E vs. A: p=0.01, and nearly statistically significant difference for D vs. E: p=0.072, and E vs. F: p=0.096). A similar trend was also observed in the TVAL regions (statistically significant difference for B vs. C: p=0.048, and nearly statistically significant difference for E vs. C: p=0.07). Thirdly, it was found that the mechanical stretches in the circumferential direction of the MVAL were higher in the regions near the annulus (regions A, B, and C) than those in regions near the free edge (regions D, E, and F) (circumferential direction, 0.036<p<0.703; radial direction, 0.136<p<0.842). This trend was not observed for the TVAL as the mechanical stretches were fairly uniform across the entire leaflet. Specifically, the mechanical stretches in the circumferential direction were 1.12-1.16 and 1.12-1.14 for the MVAL and TVAL tissue regions, respectively, with radial stretches of 1.13-1.15 and 1.11-1.14 for the MVAL and TVAL tissue regions, respectively.

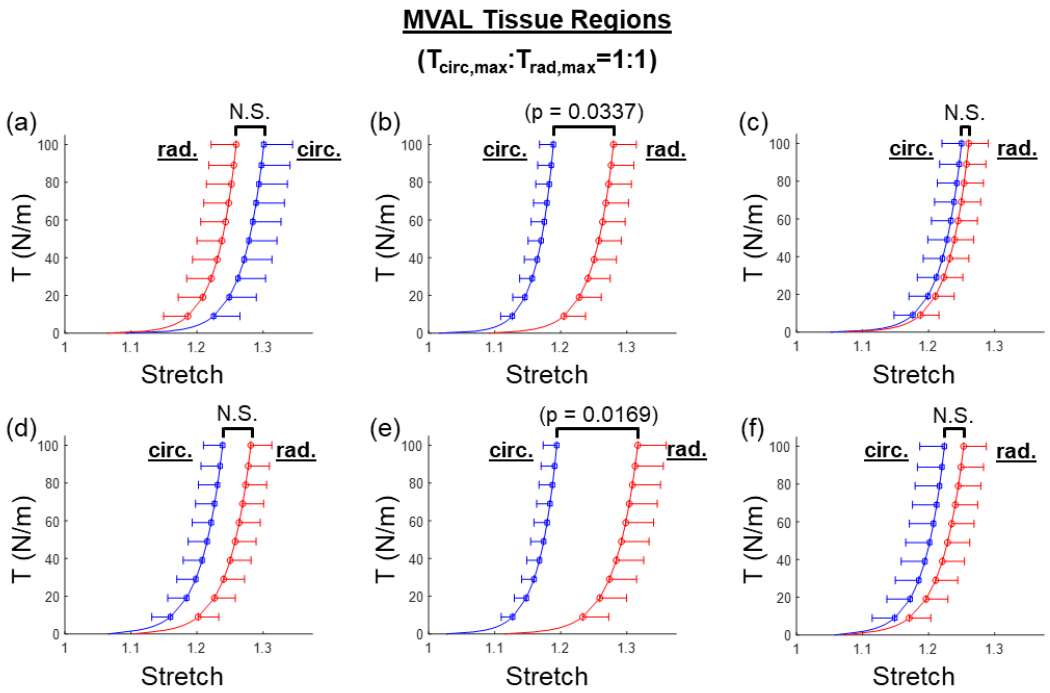

Figure 3-5. Mean ± SEM of membrane tension versus total tissue stretch results for the six MVAL tissue regions under equibiaxial loading protocol ($T_{circ,\max} : T_{rad,\max} = 1{:}1$). The labels (a-f) correspond to the region label defined in **Figure 3-1c**. N.S.: non-statistically significant.

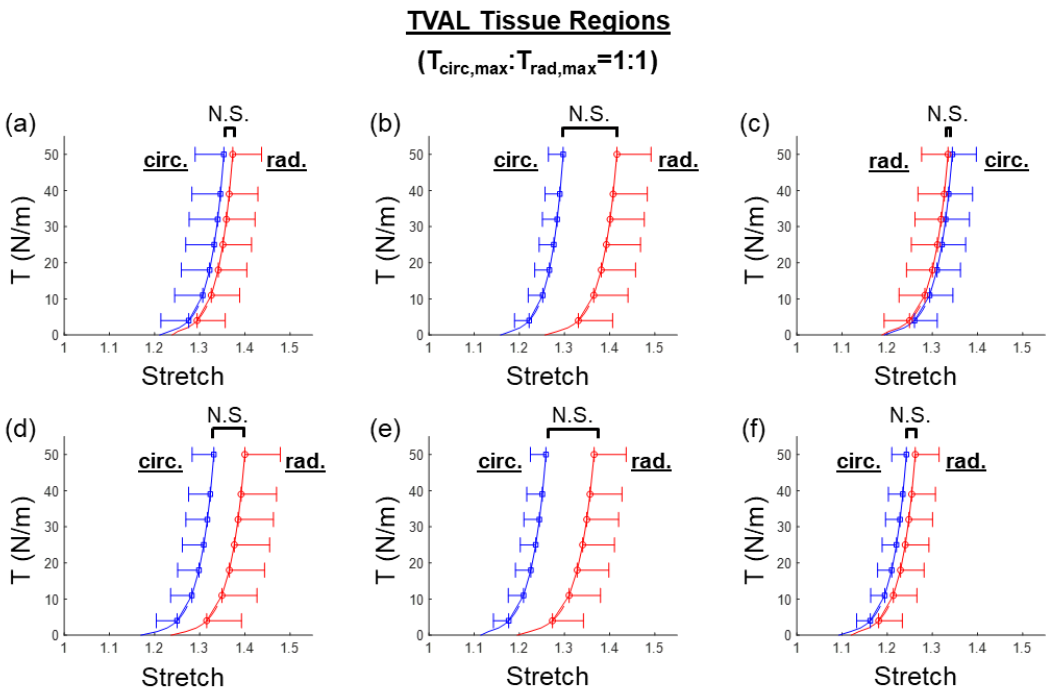

Figure 3-6. Mean ± SEM of membrane tension versus total tissue stretch results for the six TVAL tissue regions under equibiaxial loading protocol ($T_{circ,\max} : T_{rad,\max} = 1{:}1$). The labels (a-f) correspond to the region label defined in **Fig. 3-1c**. N.S.: non-statistically significant.

A general trend of anisotropic exponential decays in the normalized membrane tension was found for both the MVAL and TVAL tissue regions (**Fig. 3-7** and **Fig. 3-8**). For the MVAL, all regions were observed to have a similar stress decay, except for region C, which decayed slightly more in the circumferential direction (**Fig. 3-7c**). As for the TVAL, decays in the membrane tension magnitude were observed to be similar across all regions (**Fig. 3-8**). Comparing between the MVAL and the TVAL, an approximately 20-25% decay in stress was observed for the MVAL tissue regions, whereas 15-20% stress reduction was found across all TVAL tissue regions.

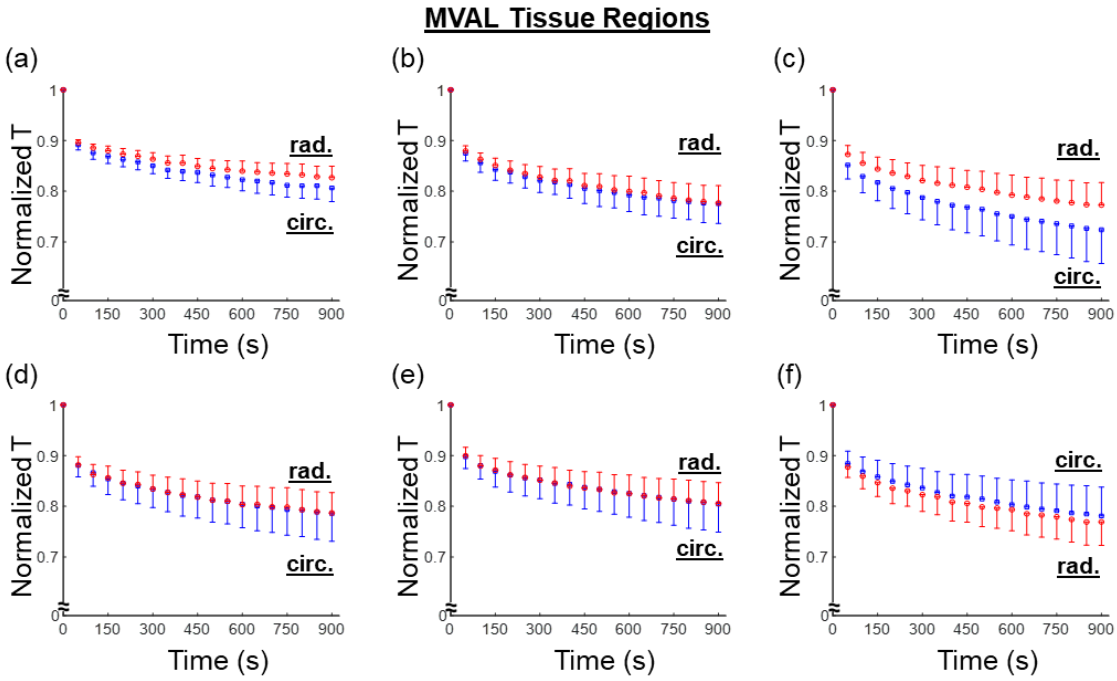

Figure 3-7. Mean ± SEM of the normalized membrane tension versus time results from the stress relaxation testing for all the six MVAL tissue regions.

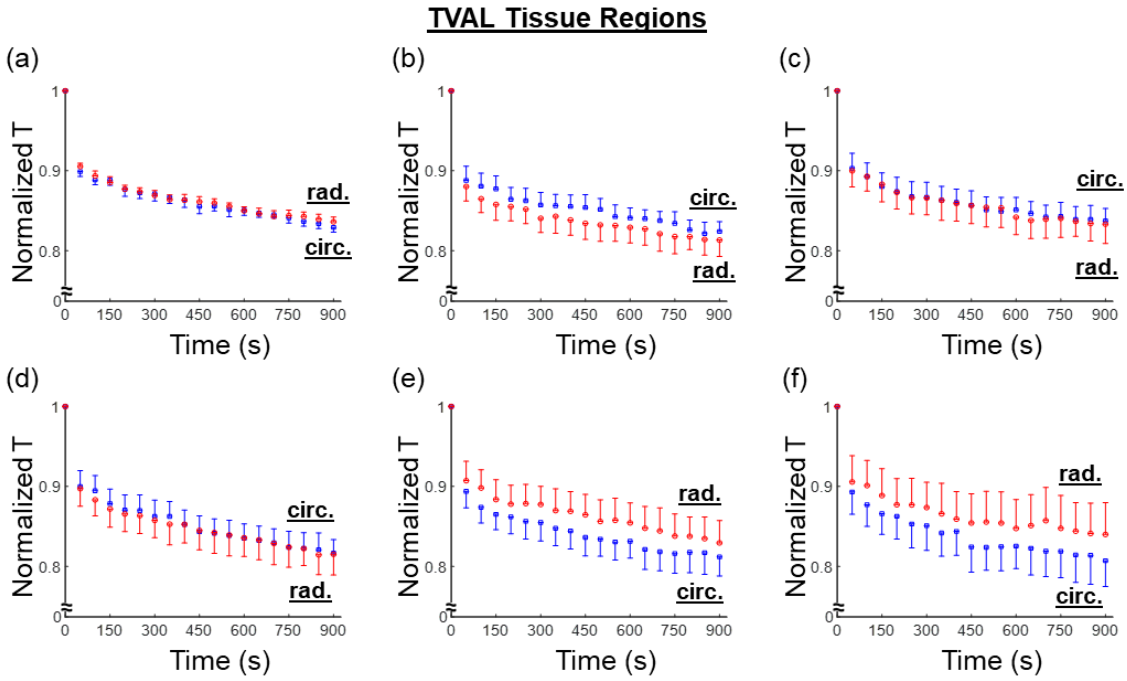

Figure 3-8. Mean ± SEM of the normalized membrane tension versus time results from the stress relaxation testing for all the six TVAL tissue regions.

3.2.2 Results from the Layer-Mechanics Study

Histology confirmed the successful separation of the leaflets into distinct layers for both the MVAL (**Fig. 3-9**) and the TVAL (**Fig. 3-10**) via our microdissection technique. Histological quantification of the microstructures indicated both the MV and TV anterior leaflets to be primarily composed of circumferentially oriented collagen fibers (**Fig. 3-9a** and **Fig. 3-10a**). The total GAG composition of the intact TVAL and MVAL (27.4% and 22.4%, respectively) was greater than the total elastin composition in the TVAL and MVAL. Additionally, elastin fibers constituted a similar percentage of the TVAL (14.3%) to the MVAL (14.8%), but the MVAL was more collagenous than the TVAL (62.8% vs. 58.3%). Both the TVAL-A/S and F/V layers contained only a small fraction of non-fibrous ground substance. The elastin struts in the fibrosa and ventricularis appeared to be radially oriented while in the atrialis they were more complexly oriented.

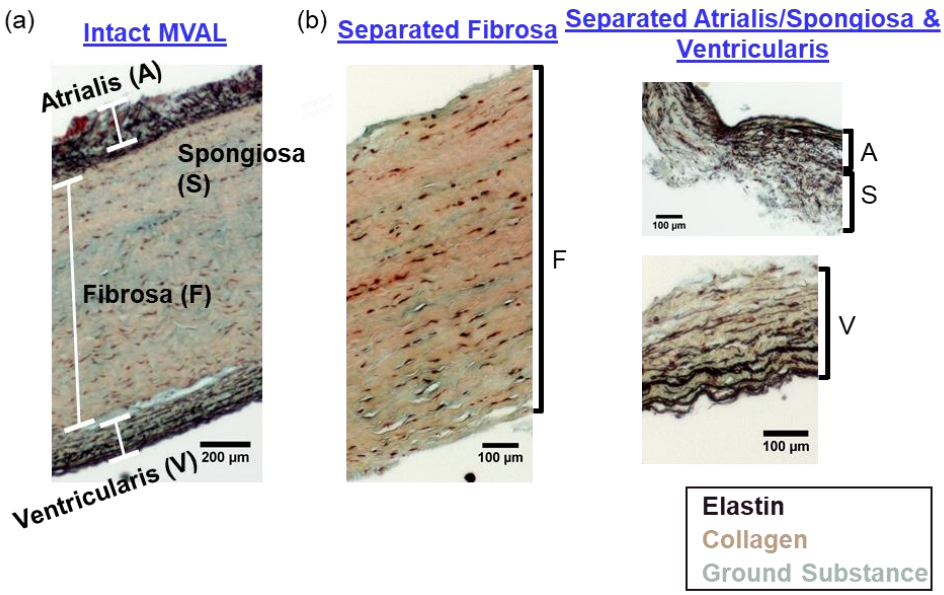

Figure 3-9. Histological images with Movat's Pentachrome stain: (a) intact MVAL tissue, (b) separated fibrosa layer (F), combined atrialis/spongiosa (A/S), and ventricularis (V).

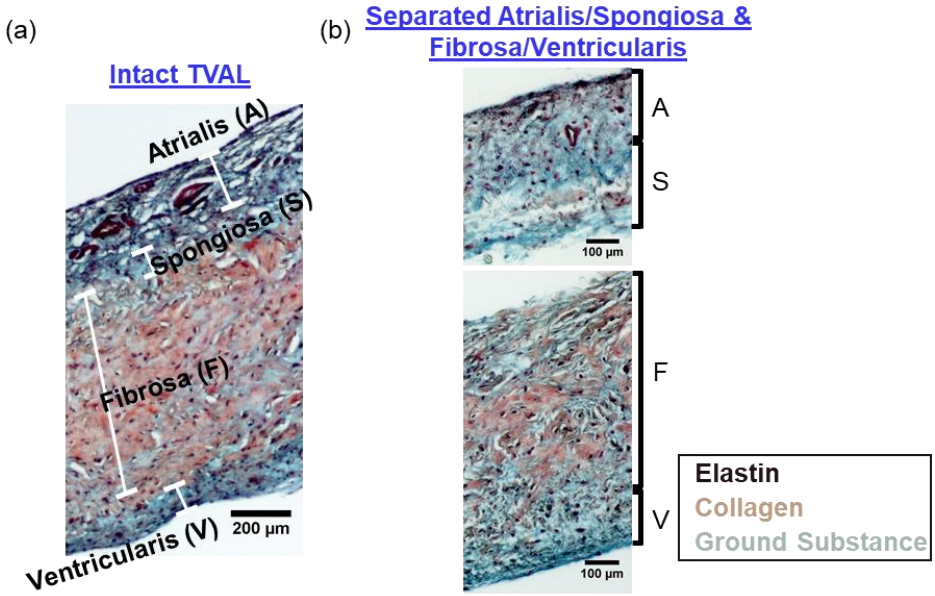

Figure 3-10. Histological images with Movat's Pentachrome stain: (a) intact TVAL tissue, and (b) separated combined atrialis/spongiosa (A/S) and combined fibrosa/ventricularis (F/V) layers.

The nonlinear, anisotropic mechanical behaviors of both TVAL A/S and F/V layers were identified from the peak tissue stretch (**Fig. 3-11**). The anisotropy largely stemmed from the

specimen's preconditioning stretch, as separated from the peak stretch. The average preconditioning stretch in the radial direction was 0.11 greater (p=0.132) for the A/S and 0.14 greater (p=0.093) in the F/V than the respective circumferential preconditioning stretch. Interestingly, the mechanical stretches for TVAL layers were found to be nearly isotropic, independent of the loading protocol. Additionally, the tissue stretches of the A/S layer and F/V layer revealed that A/S to be more compliant under all loading ratios (p=0.240-0.589, **Fig 3-11**).

The stretches of the MVAL A/S layer exhibited a nonlinear and anisotropic behavior, whereas both the fibrosa and ventricularis layers were found to be more isotropic (**Fig. 3-12**). The anisotropy of the A/S layer and the isotropy of the F and V layers can be explained by the associated preconditioning and mechanical stretch results. The average preconditioning radial-circumferential stretches differed by 0.08 (p=0.394) for the atrialis/spongiosa but only by 0.02 for both the fibrosa (p=0.699) and the ventricularis (p=0.818). Moreover, the mechanical stretch results showed that the behavior of the layers after preconditioning was nearly isotropic. The only layer that marginally diverged from this trend was the ventricularis under other non-equibiaxial loading protocols.

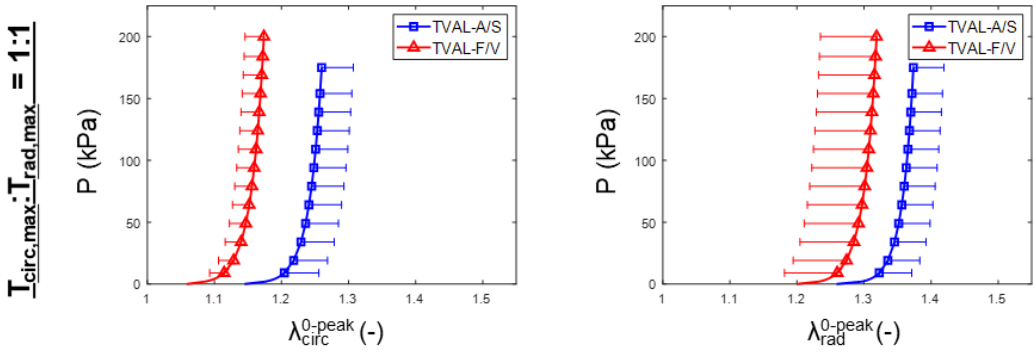

Figure 3-11. Mean ± SEM of the biaxial mechanical testing results (first Piola-Kirchhoff stress versus peak stretch) of TVAL layer tissues (n=6) under equibiaxial loading.

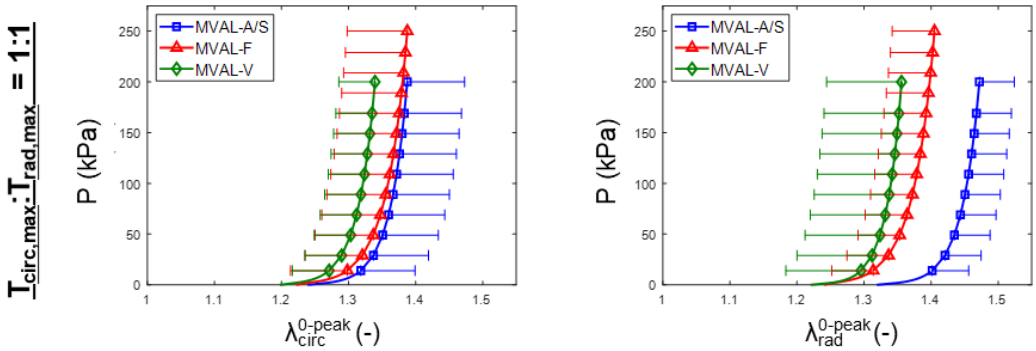

Figure 3-12. Mean ± SEM of the biaxial mechanical testing results (first Piola-Kirchhoff stress versus peak stretch) of MVAL layer tissues (n=6) under equibiaxial loading.

3.2.3 Results from GAG Investigation

To account for variations between specimens and to ensure that the treatment met the desired threshold (>50% GAGs removed), the optimal treatment time for both the MVAL and TVAL was selected to be 100 minutes (**Fig. 3-13** and **Table 3-1**). Thicknesses of the tissue leaflets, to be used for biaxial testing, before and after enzyme treatment were recorded using the digital caliper method, revealing a 20-30% reduction in tissue thickness after treatment: MVAL-C, 0.503±0.030 mm; MVAL-T, 0.361±0.038 mm; TVAL-C, 0.254±0.044 mm; TVAL-T, 0.176±0.018 mm.

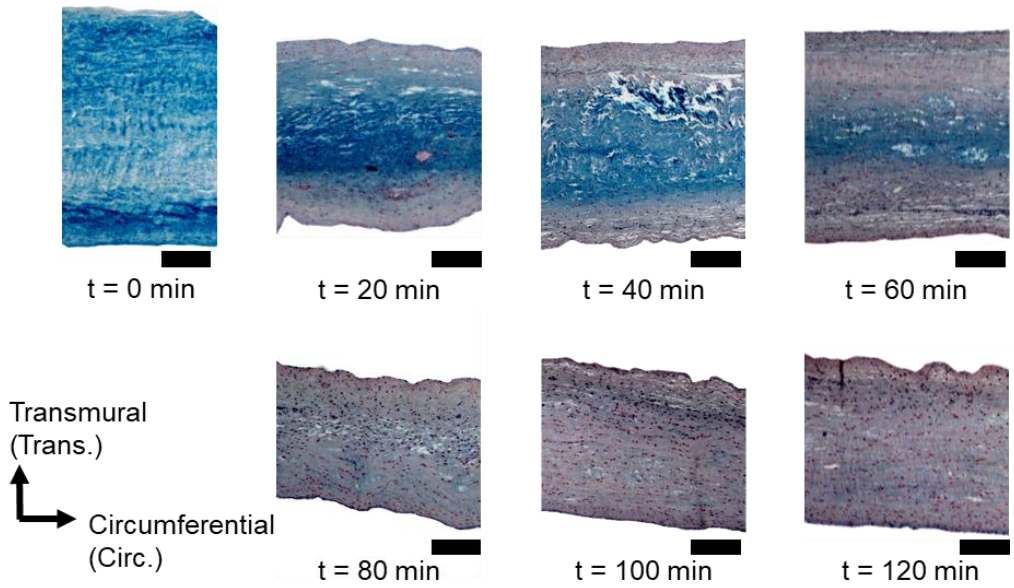

Figure 3-13. Alcian blue-stained histological images demonstrating the progression of the GAG constituent removal associated with various enzyme treatment durations. Scale bar=200 μm.

Table 3-1. Percentage of GAGs in the control (time=0 mins) and enzyme-treated tissue strips over a 160-minute treatment time. All quantities are reported as mean ± SEM.

Time (minutes)	MVAL		TVAL	
	GAGs in Tissue Strip (%)	GAG Reduction w.r.t. Control (%)	GAGs in Tissue Strip (%)	GAG Reduction w.r.t. Control (%)
0	82.23±3.85	–	45.16±1.08	–
20	47.43±2.31	42.32	16.94±2.57	62.49
40	36.83±3.33	55.32	11.66±0.64	74.19
60	27.20±2.52	66.92	14.31±0.88	68.30
80	31.63±1.52	61.53	13.11±1.10	70.97
100	19.81±1.62	75.91	17.50±0.93	61.24
120	17.70±1.46	78.48	11.63±1.04	74.24
140	21.36±1.40	74.02	17.61±1.23	61.00
160	24.99±1.76	69.60	17.32±1.99	61.65

Comparing the control and enzyme-treated groups with regard to the equibiaxial loading ratio (T_{Circ}:T_{Rad}=1:1), it was observed that the GAG-degraded specimens experienced greater stretches than the control specimens in both the circumferential and radial directions. Moreover, both the circumferential and radial directions experienced greater stretch values post treatment. The percent

difference in λ_{circ}^{0-peak} was 5.4% for the MVAL (p=0.038) and 4.7% for the TVAL (p=0.132), whereas the percent differences in λ_{rad}^{0-peak} were 5.3% and 7.6% for the MVAL (p=0.165) and the TVAL (p=0.015), respectively (**Fig. 3-14a** and **Fig. 3-15a**).

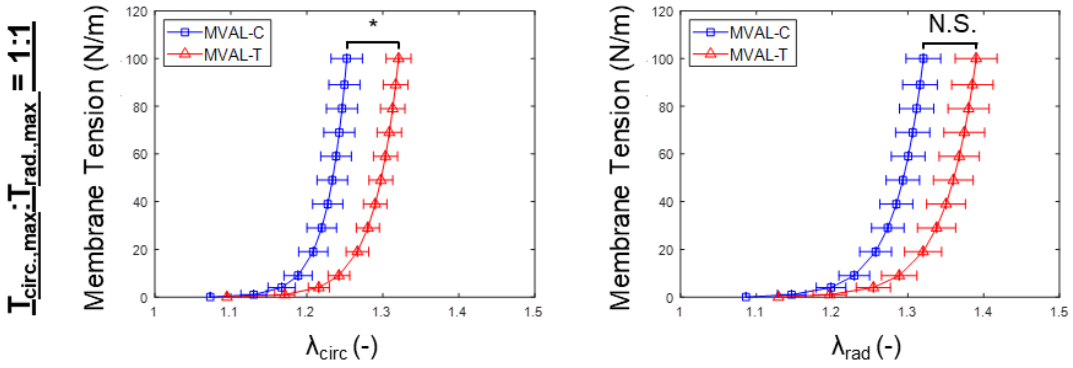

Figure 3-14. Mean ± SEM of the peak tissue stretch responses of the control and enzyme-treated groups for the MVAL (n=7). (*: statistically significant; N.S.: statistically non-significant)

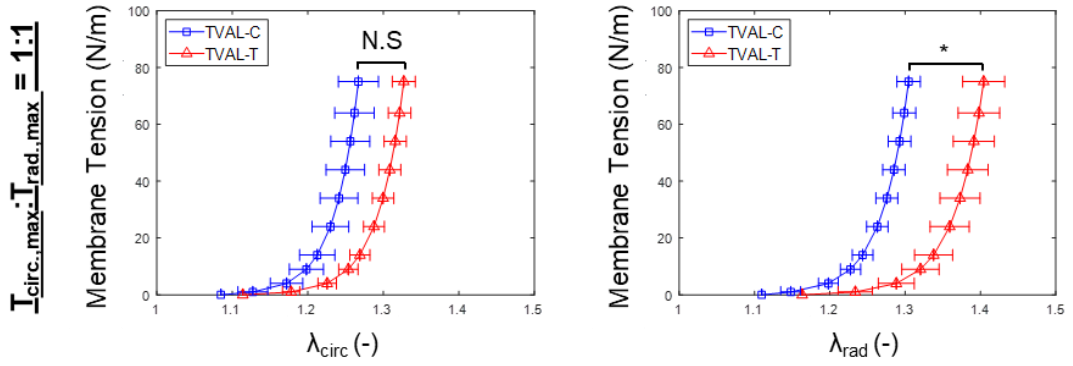

Figure 3-15. Mean ± SEM of the peak tissue stretch responses of the control and enzyme-treated groups for the TVAL (n=6). (*: statistically significant; N.S.: statistically non-significant)

Similar trends in the peak stretch were observed for the non-equibiaxial loading protocols (**Fig. 3-14b,c** and **Fig. 3-15b,c**). Additionally, the peak stretch values for the equibiaxial protocol were further used to compute the anisotropy index. The MVAL tissues demonstrated minimal

change between the control and treated *AI* values (1.06 ± 0.02 vs. 1.05 ± 0.02; p=0.902), while a slight increase in the *AI* (1.03±0.02 vs. 1.06±0.03; p=0.556) was observed for the TVAL tissues. Secondly, the preconditioning stretches were shown to be higher post-treatment for both the circumferential and radial directions. Specifically, the difference in λ_{circ}^{0-1} was 2.1% higher for the MVAL (p=0.274) and 2.7% higher for the TVAL (p=0.310). The difference in λ_{circ}^{0-1} was 3.9% higher for the MVAL (p=0.365) and 4.8% higher for the TVAL (p=0.048, *statistically significant*). Finally, the mechanical stretches were higher post-treatment for both the MVAL and the TVAL. The difference in λ_{circ}^{1-peak} was 3.3% for the MVAL (p=0.058) and 2.0% for the TVAL (p=0.240), respectively, while the difference in λ_{rad}^{1-peak} was 1.2% for the MVAL (p=0.515) and 2.6% for the TVAL (p=0.329). Similar increases in the mechanical stretch post-treatment were also observed for the non-equibiaxial loading protocols.

The average, normalized membrane tension reductions for the treated and untreated (control) specimens are presented in **Figure 3-15** for the MVAL and in **Figure 3-16** for the TVAL. It was found that the control tissues had a larger stress reduction than the treated tissues in both directions for the MVAL. In the circumferential direction, there was an observed statistically significant difference in the pre- and post-treatment stress relaxation (-C: 18.9% relaxation, -T: 15.2% relaxation, p=0.011). In the radial direction, there was an observed statistically significant difference in the pre- and post-treatment stress-relaxation behaviors (-C: 17.8% relaxation, -T: 15.1% relaxation, p=0.026). As for the TVAL tissue specimens, the difference in the stress relaxation was less pronounced. Specifically, there was an approximately 13% difference in the pre- and post-treatment stress-relaxation behaviors in the circumferential direction (-C: 17.1% relaxation, -T: 15.0% relaxation, p=0.065) and an approximately 12% difference in the radial direction (-C: 16.4% relaxation, -T: 14.5% relaxation, p=0.065).

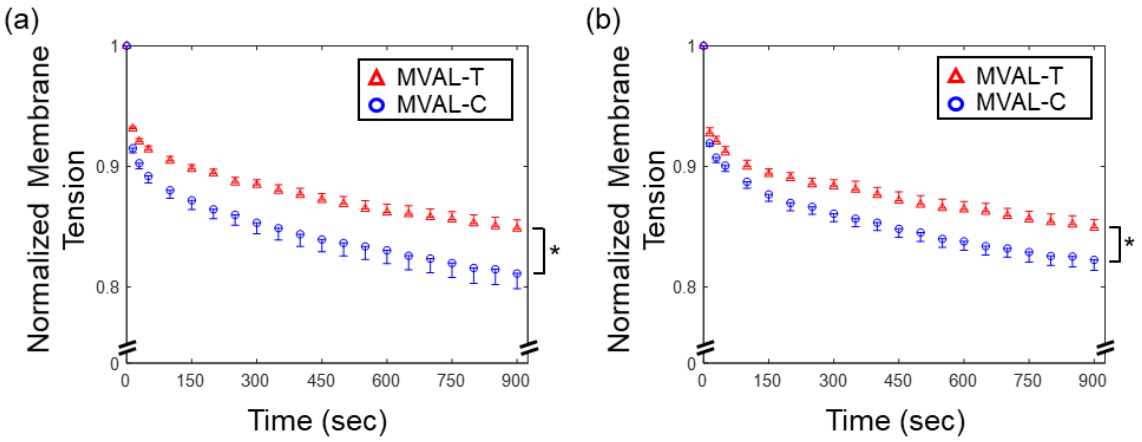

Figure 3-16. Comparison of the 15-minute biaxial stress-relaxation responses (mean ± SEM) of the MVAL between the control and enzyme-treated groups: (a) circumferential; (b) radial directions. (*: statistically significant)

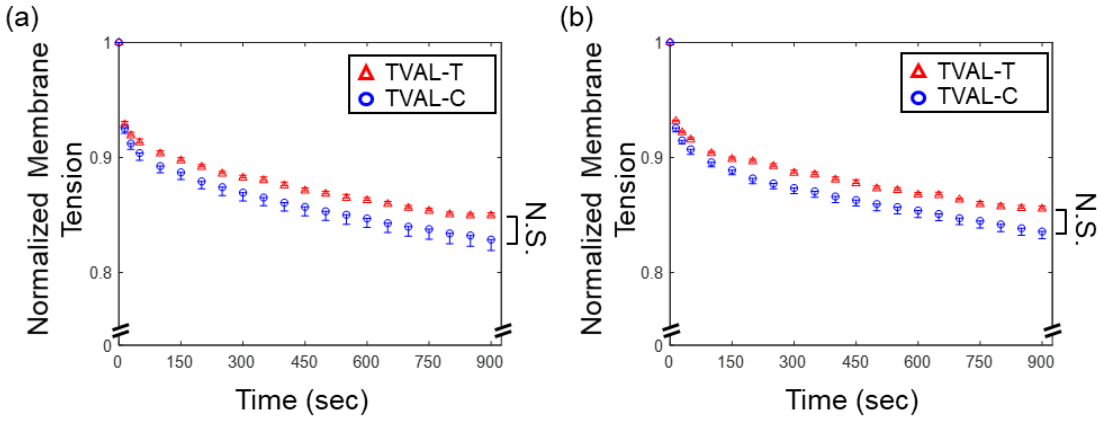

Figure 3-17. Comparison of the 15-minute biaxial stress-relaxation responses (mean ± SEM) of the TVAL between the control and enzyme-treated groups: (a) circumferential; (b) radial directions. (N.S.: statistically non-significant)

3.3 Discussion

There were a few limitations shared among all investigations. First, in previous studies it has been shown that the mechanical behavior of heart valve leaflets is loading-rate dependent [73, 74];

however, due to the limitations of the CellScale BioTester system, it was not possible to investigate loading-rate dependency as close to the *in vivo* physiological function of the atrioventricular heart valves. Secondly, the thickness obtained via the dial caliper method may not be as accurate as other non-contact measurement techniques, such as optical coherence tomography; nevertheless, in our previous study we have shown that the dial caliper method agrees reasonably with thickness measurements obtained via histological methods (see Table 6 and Figure 10 in Jett *et al.* (2018) [12]). Third, the freezing effect on the AHV mechanical behaviors has been shown to cause minor differences in tissue mechanics, however they are insignificant [17]. Fourth, a hold time of 15 minutes was considered for the stress relaxation testing in these studies, as opposed to the suggested 4 hours of previous literature [18, 75, 76].

3.3.1 Overall Findings from the Regional Investigation

Biaxial mechanical characterization of the six regions of the MVAL and TVAL allowed for comparisons of the leaflet tissue's regionally varied mechanical properties. It was found that the central regions (region B and region E, **Fig. 3-1c**) of both leaflets had a more distinct difference in the *peak total tissue stretches*. Additionally, for the TVAL we found that the p-values of the material anisotropy for the central regions were much lower than those for the edge regions, suggesting a more distinct difference in the *peak total tissue stretches* for the TVAL central regions, which would agree with previous investigations [14]. Regional variance was also exemplified through stress relaxation testing. Moreover, a fair amount of variation in stress decay was also observed between the six tissue regions. The general trend of greater stress decay in the MVAL regions compared to the TVAL regions suggests that the MVAL regions may have greater stress-relaxation potential than the TVAL regions. These novel finding suggests there is a noticeable regional variance in the mechanical behaviors of the MVAL and TVAL, typically when

comparing the central belly regions to those edge regions (i.e., closer to the free edge and commissures of the valve).

3.3.2 Overall Findings from the Layer-Mechanics Study

The present study highlights the subtle and considerable heterogeneity in the tissue biomechanics distributed throughout the intact tissue. This study's important biomechanical findings can be summarized as follows: (i) the atrialis layer of both selected leaflets (MVAL and TVAL) exhibited an apparent toe region and a significant compliancy; (ii) the average peak and preconditioning stretches of the intact TVAL were bounded between those responses of the A/S and F/V layers in the circumferential direction; (iii) contrary to the aortic valve leaflets, the MVAL fibrosa and ventricularis layers showed a nearly isotropic behavior.

There are some specific limitations to the layer investigation that arise from the methodology. Primarily, the micro-dissection procedure used to obtain the leaflet layers could potentially damage the tissue and it also results in a relatively small effective testing size (~3.5 mm) compared to previous biaxial mechanical studies of heart valve leaflet tissues (6.5-10 mm) [12, 14, 22]. Another minor limitation includes the relatively small sample size (n=6).

3.3.3 Overall Findings from the GAG-Degradation Study

This study has successfully provided insight into the previously uninvestigated mechanical contributions of the glycosaminoglycans to atrioventricular heart valve leaflet function. Biaxial mechanical testing revealed that removal of the GAGs resulted in a statistically significant increase of the peak tissue stretch in both the circumferential and radial directions of the MVAL and TVAL. Decomposing the peak tissue stretch into the preconditioning and mechanical stretches, significant differences were observed for the preconditioning stretch in the radial direction of the TVAL, and

for the mechanical stretch in the circumferential direction of the MVAL. One possibility for the greater stretch in the tissue post-treatment may be due to lessened fiber recruitments that are caused by a deficiency of GAGs in the tissue [5, 77, 78]. Specifically, it may suggest that GAGs are responsible for regulating the extensibility of the tissue, acting as a mediator between the atrialis and fibrosa layers. Stress-relaxation testing also provided insight into the GAG mechanical contributions, where treated specimens showed a smaller stress decay than untreated specimens. This difference was greater in the MVAL than the TVAL, suggesting that those constituents have a greater stress decay potential in the MV than the TV. These digressions in the stress-relaxation behavior post-enzymatic treatment suggest that the GAGs contribute to the viscoelastic properties of the AHV leaflets. The overall findings also suggest that GAGs are important to proper function of the AHV leaflets, and a GAG deficiency in those leaflets can significantly increase tissue extensibility, which could lead to inadvertent effects such as valvular heart disease. This information could guide development of heart valve therapeutics.

There are some additional limitations in the study on the GAG contributions. Primarily, the GAGs were not completely removed during the enzymatic treatment procedure; however, the majority (>50%) of GAGs were removed, and statistically significant differences in the tissues' mechanical responses were observed. Also, the enzyme-treated samples had a smaller effective specimen size in comparison to the control (5.5 mm vs. 7 mm).

3.4 Concluding Remarks

In this chapter, developments have been made that will improve the fundamental understanding of the AHV leaflets mechanical and microstructural behaviors. By better understanding the regionally varying leaflet mechanics, computational models can be refined for a more accurate heart valve simulation considering heterogenous leaflet deformations. Through

the study on the individual layer mechanics and the effects of the glycosaminoglycans on overall leaflet mechanical function, the information can be used for developing and refining microstructure-based constitutive models [34, 62, 69, 79-87] or aid in the development growth and remodeling framework for soft tissues [88, 89]. Furthermore, information on the tissue microstructure-mechanics relationships can be useful in the field of tissue-engineered leaflets, where the constructs are made to emulate native tissues [90, 91]. These studies supplement the current AHV literature and pave the way for other studies that can further expand knowledge on the MV and TV leaflet mechanics, such as the testing of the other leaflets using the aforementioned methods or investigating other microstructure-mechanics relationships.

CHAPTER 4 – MECHANICS OF AHV LEAFLET-CT-PAPILLARY MUSCLES ENTITIES

Studies in AHV biomechanical modeling have utilized the experimentally characterized valve leaflets' mechanical properties [34, 85]. Effort has also been devoted to incorporating the mechanical testing data of the AHV chordae tendineae from the literature into these computational models. The majority of those experimental CT characterizations considered the strut CT of the AHVs, because the strut chordae tendineae have been shown to experience greater *in vivo* loading than the other chordae tendineae categories (i.e., the marginal and basal CT) [92]. However, these previous experimental studies [15, 44, 85, 93] have been primarily focused on characterizing *individual* CT segments. Instead, it could be beneficial to use a leaflet-chordae-papillary muscle entity testing configuration that preserves the interactions between the chordae and the AHV leaflet and between the CT and the papillary muscles (PMs). A recent study by Gunning and Murphy (2015) [94] moved towards this modified experimental setup, in which a customized clamping method was developed with a leaflet-CT-PM entity. Nonetheless, this clamp-based mounting method did not adequately allow deformations of the leaflet or papillary muscle insertion.

To further advance our knowledge in the mechanical behaviors of the AHV chordae tendineae, the objective of this study is to characterize the strut chordae by means of a leaflet-CT-PM entity. The data reported from this study could provide new insight into the biomechanical role of the chordae tendineae in the AHV function, where mechanical interactions among the CT, valve leaflets, and papillary muscles are considered together. Such improved understanding of AHV strut CT tissue mechanics could also help with the development of AHV computational models to guide surgical treatment of chordae rupture-induced valvular heart disease.

The remaining of this chapter is organized as follows. The experimental procedure of uniaxial mechanical testing for the leaflet-CT-PM entity specimens and the corresponding data analysis are described in Section 4.1. Section 4.2 presents the results of these mechanical characterizations for the AHV chordae tendineae with our unique experimental setup, following by the key findings and their implications for the AHV biomechanics field summarized in Section 4.3

4.1 Methods

4.1.1 Tissue Preparation

Twelve healthy porcine hearts (80-140 kg, 1-1.5 years of age) were obtained from a local USDA approved abattoir (Country Home Meat Co., OK), cleaned of blood clots, and frozen for prolonged storage [64]. Within 2 days of tissue acquisition, hearts were thawed and the chordae tendineae were excised from each of the AHVs while preserving the papillary muscle and leaflet points of attachment (**Fig. 4-1a**).

In this study, strut CT of the MVAL and TVAL were selected for mechanical testing because they have been previously shown as the primary load-bearing CT during systolic closure of the AHVs [92]. Strut CT specimens were retrieved from each side of both the MVAL and TVAL apices, resulting in two CT groups per leaflet. These samples were labeled with respect to their location: LG – left chordae group, and RG – right chordae group. For the MVAL, the LG is adjacent to the posteromedial commissure and the RG is adjacent to the anterolateral commissure (**Fig. 4-1b**). For the TVAL, the LG and the RG are adjacent to the anteroseptal and anteroposterior commissures, respectively. Tissue specimens were then stored in phosphate-buffered saline solution in a refrigerated environment at 4 °C until later mechanical testing within 12 hours after dissection [95]. Measurements of the chordae thickness D at three points about the center of the CT, which was used in the tissue stress calculation, were recorded with a microscope at 4X

magnification (United Scope LLC, CA) both before and after uniaxial mechanical testing (**Fig. 4-1c**).

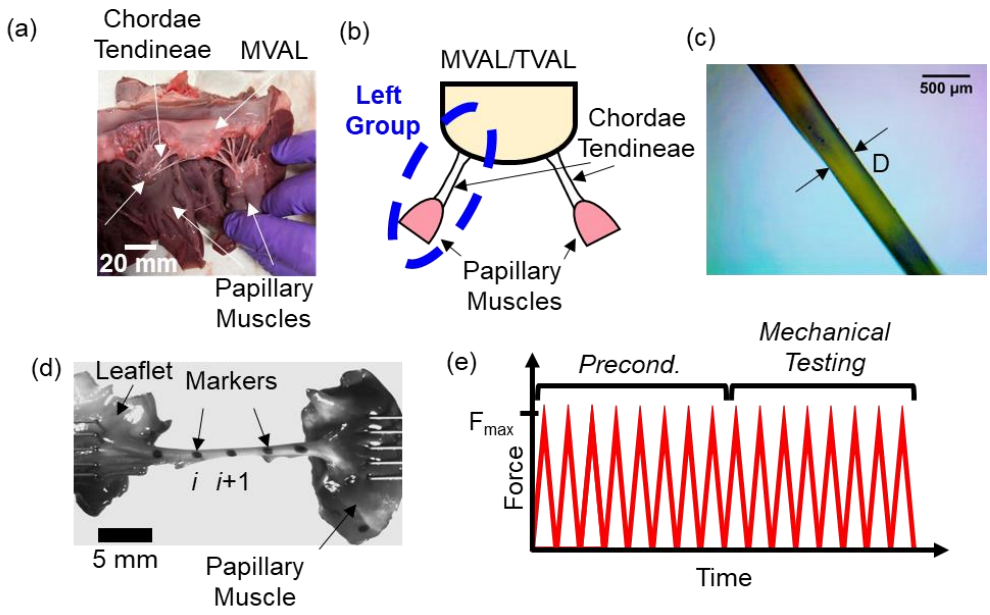

Figure 4-1. (a) Photo of a dissected representative porcine MV. (b) Schematic of the leaflet-CT-PM entities from the left and right sides of the leaflet's apex. (c) Measurement of the chordae thickness by a microscope. (d) Experimental setting of the leaflet-CT-PM entity. (e) Uniaxial mechanical testing protocol for characterizing the leaflet-CT-PM entity specimens (the targeted target force: F_{max}=1.4 N or 1.2 N for the MVAL or TVAL strut CT, respectively).

4.1.2 Uniaxial Testing

Uniaxial mechanical testing was performed using the BioTester mechanical testing system (CellScale Biomaterials Testing, Waterloo, Canada), equipped with 1.5N capacity load cells. Samples were mounted via five-tined BioRakes, anchoring the papillary muscles and AHV leaflet to the BioTester system and allowing in-plane stretching of the CT, leaflet, and papillary muscles (**Fig. 4-1d**). Approximately 5-7 fiducial markers, depending on the specimen's dimension, were

placed on the CT segment using a surgical pen for subsequent marker coordinate tracking, as described in Section 4.1.3.

A two-step force-controlled uniaxial testing protocol was employed for characterizing the CT tissues (**Fig. 4-1e**). Briefly, the MVAL/TVAL strut chordae tissues were first subjected to a *preconditioning* step of eight loading/unloading cycles using a linear ramp to the targeted force F_{max} with a rate of 4.42 N/min to restore the tissues to *in vivo* condition [96]. A maximum force of 1.4 N for the MVAL CT tissue samples was chosen for its similarity to the approximate 1.5 N force that the MVAL strut chordae experience under physiological loading, as observed in a previous *in vitro* experiment [97]. Similarly, a maximum force of 1.2 N was used for the TVAL chordae tissues, as the TV is subjected to a lower pressure gradient than the MV counterpart [14]. The loading rate of 4.42 N/min was used according to the equivalent loading rates from previous displacement-based CT mechanical characterizations, such as 3-5 mm/min in the previous *in vitro* studies [15, 85]. After preconditioning, the mechanical testing step was carried out with another eight loading-unloading cycles (**Fig. 4-1e**).

4.1.3 Tissue Stretch and Stress Calculations

Using the digital image correlation (DIC) module in the LabJoy software of the BioTester, the coordinates (x_i,y_i) of the center of the fiducial marker i were tracked (**Fig. 4-1d**), and, then, the marker's x- and y-displacements (u_i,v_i) between any two loading states were computed. The tissue stretch of the i-th CT segment between node i and node i+1 was determined using a one-dimensional two-node linear finite element [98]

$$\lambda_i = \frac{2}{l_i}\begin{bmatrix} -\frac{1}{2} & \frac{1}{2} \end{bmatrix}\begin{bmatrix} d_i \\ d_{i+1} \end{bmatrix} + 1 \,, \tag{4.1}$$

where $l_i = \sqrt{(x_{i+1} - x_i)^2 + (y_{i+1} - y_i)^2}$ is the segment length, and d_i and d_{i+1} are the displacements of nodes i and i+1, respectively, along the axial direction of the i-th segment, i.e.,

$$d_i = u_i \cos\theta + v_i \sin\theta, \quad d_{i+1} = u_{i+1} \cos\theta + v_{i+1} \sin\theta, \quad \tan\theta = \frac{y_2 - y_1}{x_2 - x_1} \ . \quad (4.2)$$

Each stretch λ of the CT tissue was obtained by averaging the stretch values of all the chordae tendineae segments, i.e., $\lambda = \frac{1}{m}\sum_{i=1}^{m} \lambda_i$, where m is the number of segments of each CT tissue specimen.

Since a uniform strain field was an inherent consequence of the above two-node linear finite element formulation, to further examine the *tissue stretch distribution* across the CT specimen, we also performed a cubic spline space curve fit to the fiducial markers using the `cscvn` built-in function in MATLAB (MathWorks, MA). Following a similar procedure in the previous study on dynamics of the mitral valve annulus [99], the spline-based stretch calculation for each CT tissue was made. Next, the Cauchy stress σ of the CT tissue was calculated by

$$\sigma = \left(\frac{F}{A_0}\right)\lambda \ , \quad (4.3)$$

where F is the force of the load cell reading, and $A_0 = \pi D^2/4$ is the undeformed area of the CT, assuming an idealized, circular cross-section with the measured thickness D.

4.1.4 Constitutive Modeling of the CT Mechanics

The CT tissues were idealized as a nonlinear, isotropic, incompressible solid and modeled by using the one-term Ogden hyperelastic constitutive model (p=1) [100]

$$\sigma = \mu\left(\lambda^{\alpha} - \lambda^{-\alpha/2}\right), \quad (4.4)$$

where μ and α are model parameters, which were estimated by nonlinear least-squares fitting to the tissue stress-stretch data using an in-house differential evolution optimization program with a residual error tolerance of 10^{-10} as the convergence criteria [101]. The normalized root-mean-square deviation (NRMSD) was computed as a metric to assess the nonlinear fit of Eq. (4.4) to the chordae tendineae's mechanical data. Herein, the NRMSD, defined as the square root of the average of squared errors, was normalized with respect to the maximum stress value.

4.1.5 Statistical Analysis

Physical quantities, such as the measured CT thickness and the quantified tissue stress and stretch, were reported as mean±standard error of the mean (SEM). Note that the peak stretch $\lambda^{(0\text{-}2)}$ quantified in Section 4.1.3 is defined as the stretch at peak loading state Ω_2 with respect to the tissue mounting configuration Ω_0. Previous studies have reported a difference in the tissue's stretch responses between preconditioning and the applied loading [28]. Thus, we further decomposed the peak stretch into the following two components for statistical analyses: (i) the preconditioning stretch $\lambda^{(0\text{-}1)}$, defined as the stretch at the end of the preconditioning Ω_1, and (ii) the stretch $\lambda^{(1\text{-}2)}$ associated with the peak tension with respect to Ω_0, such that $\lambda^{(0\text{-}2)}=\lambda^{(1\text{-}2)}\lambda^{(0\text{-}1)}$. The stretch was used in the constitutive modeling described in Section 4.1.4, and the three components of the tissue stretch were then considered in the subsequent statistical analyses.

Residual plots were developed for each of the above-mentioned parameters associated with the CT tissues to examine the data normality and constant variance. Significant departure from normality resulted in the use of the non-parametric Wilcoxon rank-sum test for the statistical analyses with the null hypothesis that the means of the two compared groups are identical.

Statistical analyses were performed using SAS 9.4 (SAS Institute Inc., NC), and the significance was defined as *significant* ($p<0.05$).

4.2 Results

4.2.1 Mechanical Testing Results and CT Thickness Measurement

From our uniaxial mechanical testing, the Cauchy stress-stretch responses of the CT tissues followed a nonlinear, exponential trend (**Fig. 4-2**), with the stress values at F_{max} reported as follows: 1.59±0.16 MPa (MVAL-LG), 1.04±0.08 MPa (MVAL-RG), 2.71±0.10 MPa (TVAL-LG), and 2.89±0.01 MPa (TVAL-RG). Mechanical testing responses were further examined by means of the peak stretches $\lambda^{(0\text{-}2)}$, the decoupled two stretches, the preconditioning stretches $\lambda^{(0\text{-}1)}$, and the stretches $\lambda^{(1\text{-}2)}$.

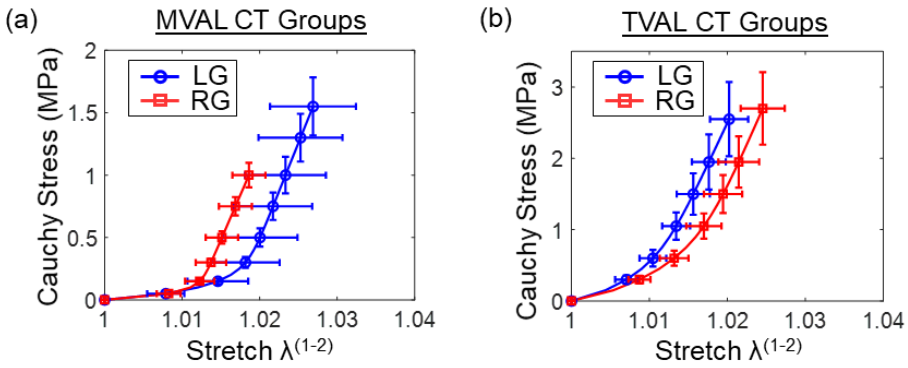

Figure 4-2. Cauchy stress versus stretch responses of (a) the MVAL strut CT, and (b) the TVAL strut CT. Values are reported as mean±SEM (n=12).

The peak stretches were (**Fig. 4-3a**): 1.09±0.02 (MVAL-LG), 1.16±0.02 (MVAL-RG), 1.08±0.02 (TVAL-LG), and 1.11±0.01 (TVAL-RG). Statistically significant difference in the median was found between the two MVAL CT tissue groups ($p=0.046$), while no significant difference in the median was observed between the TVAL CT tissue groups ($p=0.112$). Moreover, the preconditioning stretches were 1.07±0.02 for the MVAL-LG, 1.14±0.02 for the MVAL-RG,

1.06±0.02 for the TVAL-LG, and 1.08±0.01 for the TVAL-RG (**Fig. 4-3b**). Significant difference in the median was found between the two MVAL CT tissue groups (p=0.03), but there was no significant difference in the median between the TVAL tissue groups (p=0.26). Furthermore, the stretches for various CT tissue groups were reported as follows (**Fig. 4-3c**): 1.03±0.01 (MVAL-LG), 1.02±0.01 (MVAL-RG), 1.02±0.01 (TVAL-LG), and TVAL-RG, 1.03±0.01 (TVAL-RG). No significant differences in the median were found in the stretch between the MVAL CT tissue groups (p=0.507) or between the TVAL tissue groups (p=0.371).

Finally, the measured CT thicknesses were 1.08 ± 0.08 mm for the MVAL-LG, 1.32±0.07 mm for the MVAL-RG, 0.76±0.09 mm for the TVAL-LG, and 0.74±0.07 mm for the TVAL-RG (**Fig. 4-3d**). Comparing the two tissue groups, statistically significant difference in the median was found only for the MVAL groups (p=0.040), but not for the TVAL groups (p=0.931).

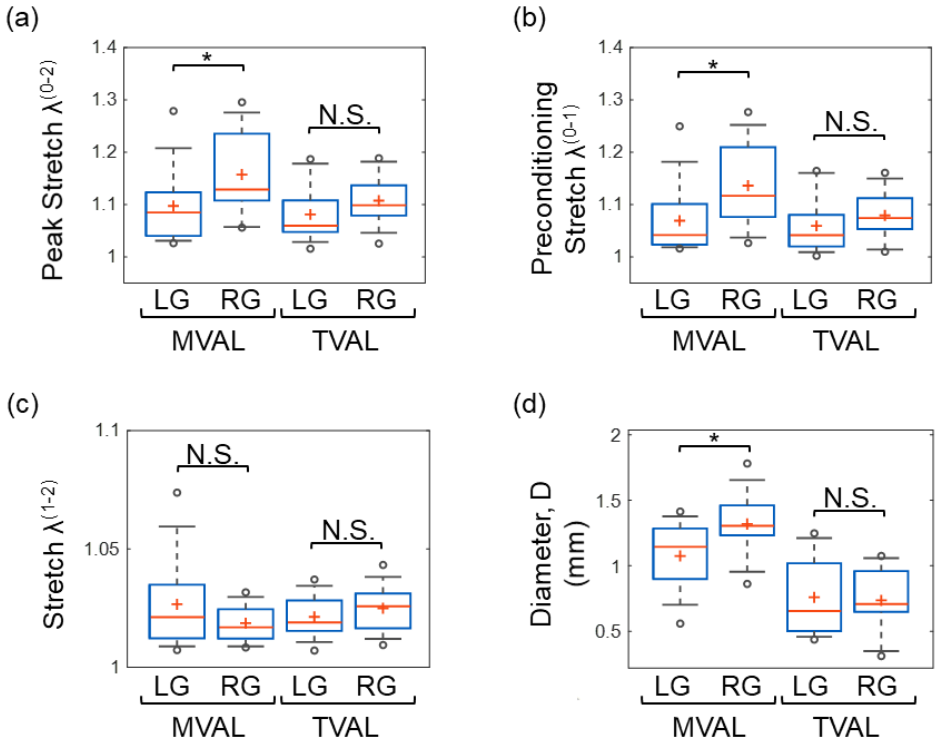

Figure 4-3. Box plots of the (a) peak stretch, (b) preconditioning stretch, (c) stretch, and (d) diameter *D* of the left chordae group (LG) and right chordae group (RG) of the MVAL and TVAL strut CT tissues. (*: $p<0.05$, N.S.: not significant)

4.2.2 Constitutive Modeling Results

The estimated Ogden model parameters for each tissue specimen are summarized in **Table 4-1** and **Table 4-2**, with representative fitting results demonstrated in **Figure 4-4a** and **Figure 4-4b** for the MVAL and TVAL strut CT tissues, respectively. In general, the Ogden model was able to accurately capture the nonlinear Cauchy stress-stretch behavior of the strut CT tissues, with parameter μ: 86.2±46.7 kPa (MVAL-LG), 29.9±12.0 kPa (MVAL-RG), 494.8±131.8 kPa (TVAL-LG), and 457.2±304.8 kPa (TVAL-RG), and parameter α: 200.6±16.9 (MVAL-LG), 271.3±16.4 (MVAL-RG), 132.8±13.0 (TVAL-LG), and 134.8±16.3 (TVAL-RG).

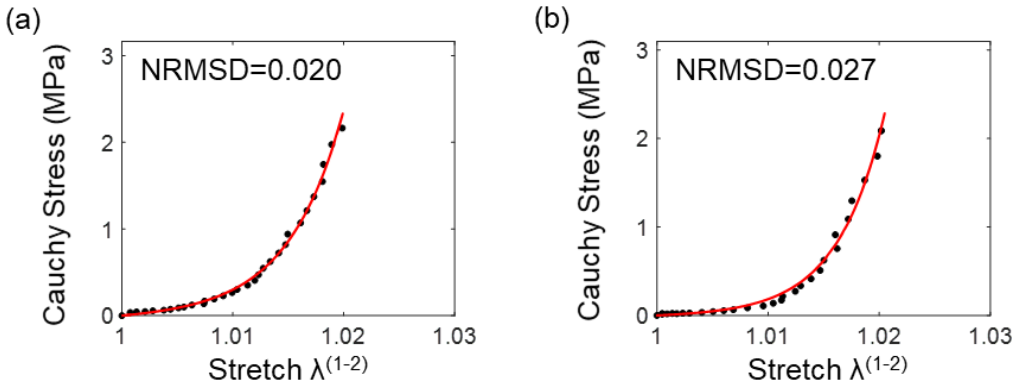

Figure 4-4. Representative Ogden model fits to the Cauchy stress-stretch data: (a) MVAL-LG #5 (μ=40.8 kPa; α=205.2), and (b) TVAL-LG #1 (μ=17.7 kPa; α=241.2). (black dots (•) denote experimental data, and red solid curves (–) refer to the Ogden constitutive model fits).

Table 4-1. Estimated Ogden model parameters for the MVAL strut CT, together with comparisons to other studies in the literature. (NRMSD: normalized root-mean-square deviation)

	MVAL-LG			MVAL-RG		
ID	μ (kPa)	α	NRMSD	μ (kPa)	α	NRMSD
1	581.8	217.5	0.029	2.1	267.8	0.042
2	8.7	221.5	0.019	63.4	212.1	0.052
3	27.8	220.7	0.017	5.9	331.6	0.027
4	1.5	193.7	0.028	4.2	239.6	0.016
5	40.8	205.2	0.020	13.3	407.6	0.043
6	4.6	87.5	0.015	88.6	302.7	0.034
7	13.0	130.1	0.024	10.7	257.8	0.023
8	0.2	179.8	0.017	36.3	271.3	0.023
9	66.4	206.6	0.029	127.0	294.1	0.039
10	79.6	160.6	0.022	1.5	221.0	0.029
11	143.9	288.3	0.084	5.6	213.2	0.034
12	65.9	295.5	0.049	0.4	236.6	0.024
Mean	86.2	200.6	–	29.9	271.3	–
SEM	46.7	16.9	–	12.0	16.4	–

Other studies in the literature	μ (kPa)	α
Porcine MVAL Strut CT (n=20) Pokutta-Paskaleva *et al.* (2019)	20.0	65.3
Ovine MVAL Strut CT (n=18) Zuo *et al.* (2016)	0.9±2.7	28.0±27.1

Table 4-2. Estimated Ogden model parameters for the TVAL strut CT, together with comparisons to other studies in the literature.

	TVAL-LG			TVAL-RG		
ID	μ (kPa)	α	NRMSD	μ (kPa)	α	NRMSD
1	17.1	241.2	0.027	159.4	90.3	0.039
2	698.0	130.8	0.028	188.3	86.1	0.022
3	174.7	146.9	0.043	16.6	172.6	0.039
4	764.9	101.3	0.042	72.6	110.0	0.051
5	1321.7	158.1	0.153	3797.4	107.6	0.046
6	1104.1	142.8	0.028	291.2	152.3	0.030
7	63.3	163.2	0.042	77.3	210.8	0.069
8	129.7	113.6	0.029	146.7	94.9	0.023
9	936.2	55.4	0.044	82.0	106.2	0.032
10	250.8	121.1	0.046	180.9	69.7	0.035
11	449.1	113.7	0.071	140.9	255.5	0.106
12	27.6	105.7	0.051	333.2	161.6	0.094
Mean	494.8	132.8	–	457.2	134.8	–
SEM	131.8	13.0	–	304.8	16.3	–

Other study in the literature	μ (kPa)	α
Porcine TVAL Strut CT (n=18) Pokutta-Paskaleva *et al.* (2019)	150.0	86.5

4.3 Discussion

4.3.1 Overall Findings and Comparisons to Existing Literature

First, we found that the MVAL strut CT were about 45% larger than the TVAL counterparts (MVAL: D=1.20±0.06 mm vs. TVAL: D=0.75±0.05 mm, **Fig. 4-3d**), which is consistent with a higher pressure gradient in the mitral valve residing in the left side of the heart. We also noticed for the MVAL that the right chordae group was generally thicker (MVAL-RG: D=1.32±0.07 mm, and MVAL-LG: D=1.08±0.08 mm) and more extensible (MVAL-RG: $\lambda^{(0\text{-}2)}$=1.16±0.02, and MVAL-LG: $\lambda^{(0\text{-}2)}$=1.10±0.02) in comparison to the left chordae group (**Fig. 4-3a**, **Fig. 4-3b**, and **Fig. 4-3c**), whereas this trend was not observed in the strut chordae of the TVAL. Furthermore,

the mechanical responses of the strut CT tissues followed an exponential, nonlinearly elastic trend (**Fig. 4-2**). As for the constitutive modeling, the Ogden model was successful in capturing the nonlinear stress-stretch responses of the tested strut CT (**Fig. 4-4**, **Table 4-1**, and **Table 4-2**). Overall, the TVAL strut chordae had a larger μ parameter (476.0±162.4 kPa) compared to the MVAL counterparts (58.0±24.3 kPa), indicating a higher stress transition in the stress-stretch curve (**Table 4-1** and **Table 4-2**). In contrast, parameter α was less varied between the MVAL and TVAL strut CT (235.9±13.7 vs. 133.8±10.2).

As opposed to other testing schemes, such as using individual segments [15, 44, 93, 102] or using leaflet-chordae-papillary muscle entities [94] (where the PM and leaflet deformations are restricted as depicted in **Figure 4-5a**), there are some differences in the quantified CT mechanics when our leaflet-chordae-papillary muscle entity testing method (**Fig. 4-5b**) was used. In general, the stretch was smaller in this study than that reported in the previous porcine and ovine studies on characterizing *individual* CT (**Table 4-3**). However, when comparing to human individual CT testing results, our stretch values were more comparable to those found in Prot *et al*. (2010) [85].

Comparing the constitutive parameters, our estimated parameter values are within a similar range to those reported in the previous studies (**Tables 4-1** and **4-2**) [15, 93]. In our study we provided constitutive parameters for each CT specimen, whereas Pokutta-Paskaleva *et al*. (2019) [15] and Zuo *et al.* (2016) [93] reported constitutive parameters for the *averaged* stress-stretch responses.

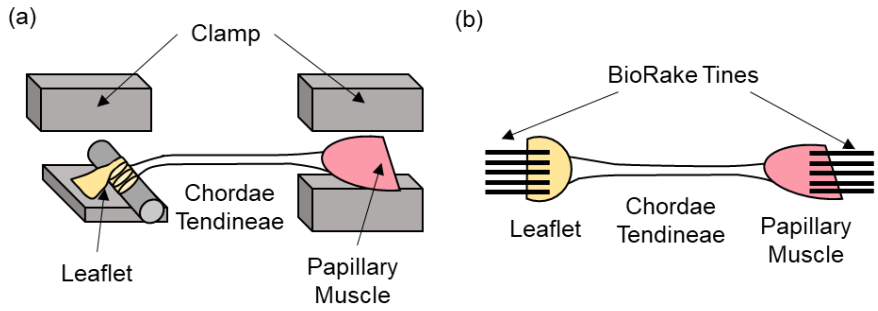

Figure 4-5. (a) Schematic of the clamp-based testing configuration used in [94]. (b) Comparison to the uniaxial testing setup of the present study, which allows the analysis of tissue deformation of strut CT, especially for the CT-leaflet insertion and the chordae-PM attachment.

Table 4-3. Comparisons of tissue stretches and Cauchy stresses. Values are reported as either mean±SEM or mean±standard deviation (SD), as indicated.

Study (Species)	MVAL Strut CT (n=12)		TVAL Strut CT (n=12)	
	$\lambda^{(1-2)}$ (-)	Cauchy Stress (MPa)	$\lambda^{(1-2)}$ (-)	Cauchy Stress (MPa)
Present Work (Porcine)	LG: 1.03±0.01 RG: 1.02±0.01 (mean±SEM)	LG: 1.59±0.16 RG: 1.04±0.08 (mean±SEM)	LG: 1.02±0.01 RG: 1.03±0.01 (mean±SEM)	LG: 2.71±0.10 RG: 2.89±0.01 (mean±SEM)
Pokutta-Paskaleva *et al.* (2019) (Porcine, MVAL, n=20; TVAL, n=18)	1.09*	3.50	1.037	3.35
Ritchie *et al.* (2006) (Porcine, n = not provided)	1.05	0.89 to 1.18	–	–
Liao and Vesely (2003) (Porcine, n=16)	1.16±0.03 (mean ± SD)	11.24	–	–
Zuo *et al.* (2016) (Ovine, n=18)	1.07±0.08 [1.02±0.08] (mean ± SD)	24.00 [1.20]	–	–
Prot *et al.* (2010) (Human, n=1)	1.06 [1.05]	3.00 [1.50]	–	–

*Stretch and stress values are associated with the peak loading for each study.
†Values in the square brackets are data in the Cauchy stress range comparable to the present study.

4.3.2 Potential Advantages of the Proposed CT-Entity Testing Method

Results of this study provide some new insight into the interrelationship of the CT tissue mechanics with the connected papillary muscle and the valve leaflet. The presented method of testing the chordae tendineae offers several potential advantages. For example, this leaflet-CT-PM entity testing method could be used to understand the varying stretches in each segment of the CT (e.g., our results presented in **Figures 4-6** and **4-7**) and to examine the distribution of mechanical loading to the three subvalvular components (i.e., among chordae tendineae, leaflet, and papillary muscles). Moreover, collagen fiber microstructural imaging techniques, such as polarized spatial frequency domain imaging (pSFDI) [103], could be integrated with this CT-entity testing scheme to quantify the collagen fiber reorientations of the chordae insertion regions. Our group is currently performing pilot investigations to explore such potential advantages of our CT-entity testing method. Our preliminary results, as presented in Chapter 5, summarize the quantified reorientations and realignment of the collagen fiber networks for the CT-leaflet insertion at two representative loading states. These results from this internal pilot study demonstrate that for the MVAL CT-leaflet insertion region, collagen fibers become better aligned under an increased uniaxial load, as evidenced by the increase in the degree of optical anisotropy. For more details about the pSFDI-based collagen fiber imaging technique and the corresponding data analyses, the reader is referred to our recent publication [103] and the previous work by Goth *et al.* (2019) [35].

We have used the presented method to perform some preliminary analyses of the deformations of both the valve leaflet and the PM segments in our leaflet-chordae-papillary muscle entity testing. Specifically, we used a surgical pen to construct a 2x2 marker array on each of the leaflet and PM regions, and then employed a four-node single finite element to calculate the tissue strains based on marker coordinates determined by the digital image correlation method [104, 105]. For the

leaflet segment, the stretches were 1.09±0.07 (MVAL, n=3), and 1.06±0.01 (TVAL, n=5). As for the papillary muscles, the stretches were 1.03±0.07 (MVAL, n=3) and 1.06±0.01 (TVAL, n=5). Comparing to the CT segment stretches, the papillary muscles and leaflet stretches were generally higher than that of the CT segment, suggesting the essential interactions among the AHV leaflets, the papillary muscles, and the chorda tendinea segment. Further investigations with a larger sample size would be useful to confirm the observed trends.

Another uniqueness of our leaflet-chordae-papillary muscle entity testing setup and spline-based tissue deformation calculation was that the variations in the tissue stretch across the CT specimen were, for the first time, quantified (**Fig. 4-6**). From these novel results, we observed that the largest stretch occurred primarily near the leaflet insertion. This observation was further confirmed when the stretches were averaged across four quarter-segments of the CT domain, where the leaflet insertion (1Q) exhibited the highest stretch (**Fig. 4-7**). Previous failure analyses of the CT found the leaflet insertion region to be the most rupture-vulnerable area, which is consistent with our observed trend [106]. This is also consistent with where chordae typically rupture in the human mitral valves.

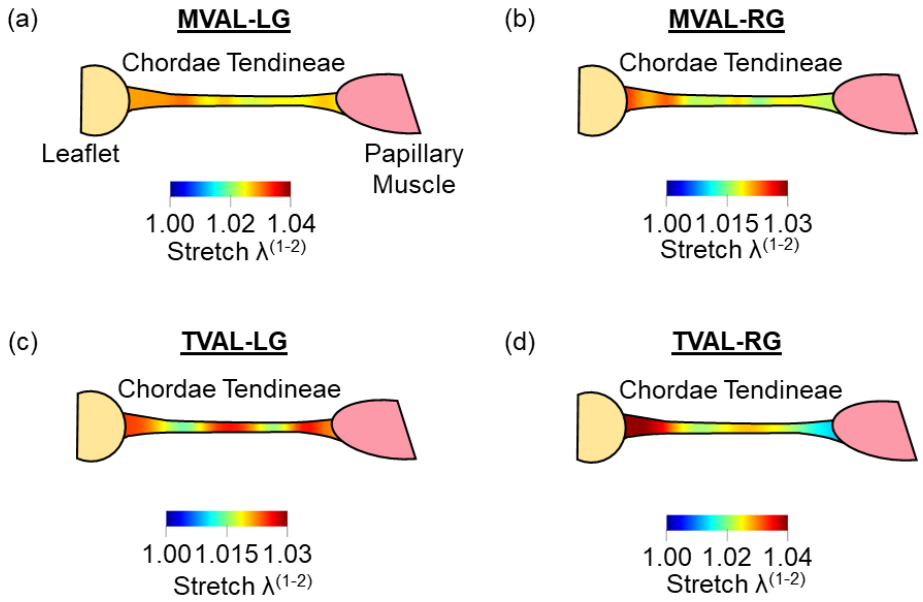

Figure 4-6. Distributions of the stretch across the CT domain determined by the cubic B-spline fitting (n=12): (a) MVAL-LG, (b) MVAL-RG, (c) TVAL-LG, and (d) TVAL-RG.

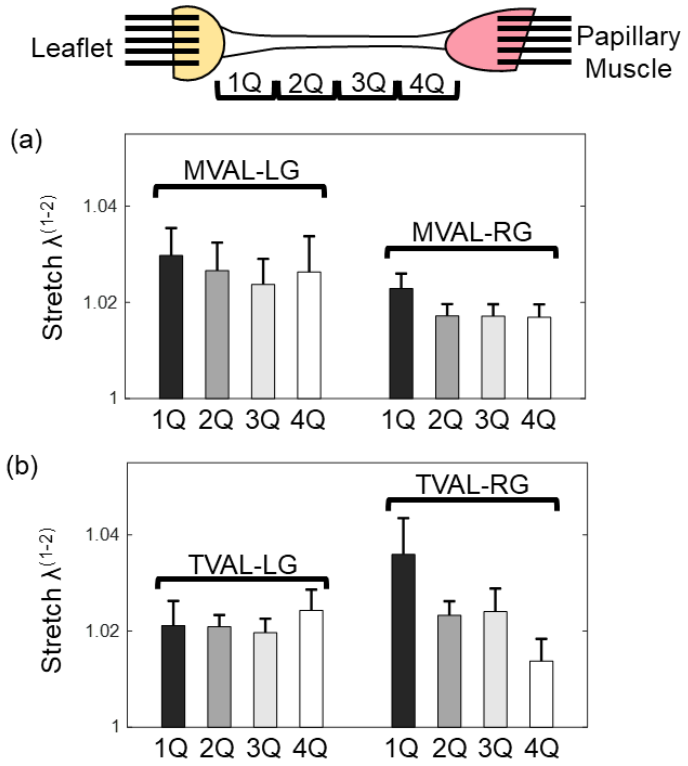

Figure 4-7. Variations in the stretch of the four quarter-sections of the CT segment: (a) MVAL strut chordae, and (b) TVAL strut chordae. Values are reported as mean ± SEM (n=12)

4.3.3 Study Limitations

There are a few limitations in this study. First, freezing of the porcine hearts was used prior to the mechanical testing for prolonged preservation of tissues. Previous studies have found that freezing does not affect the mechanics of soft tissues, such as skin and arterial tissue [63, 64], but papillary muscles included in this study may be affected by the freezing-storage procedure, which warrants future investigations. Secondly, the testing configuration we used did not represent the three-dimensional movement of the CT structure may experience *in vivo*. It may be beneficial to perform the mechanical characterizations of the leaflet-chordae-papillary muscle entity by using a left-heart or right-heart simulator [107] to further evaluate the findings of the present study. Specifically, it would be worthwhile to investigate how the papillary muscles interact with the

ventricular attachment, along with the papillary muscles' non-uniform contractile motions, and to examine how the left-sided ventricular pathologies influence the right-sided sub-valvular components. Thirdly, the testing method proposed cannot be used to evaluate the CT rupture mechanics as the papillary muscles or leaflets would tear from their tine insertions before the CT would break. Nevertheless, the methodology presented in this study is useful for investigating the mechanics under physiologically representative loading, as there is no tearing of the attachments at the targeted forces. Another minor limitation is the use of the spline-based approach to quantify the tissue stretch, by which errors may be introduced during the spline-based curve smoothing/fitting process. Nonetheless, we have verified internally that minimal differences (<3%) in the calculated tissue stretches of the chordae tendineae were found between the finite element-based and splined-based methods (see Section 4.1.3).

4.4 Concluding Remarks

In this study the chordae tendineae have been characterized in a unique manner that allows for better insight to the *in vivo* mechanical interactions between the CT and the leaflet or papillary muscle attachments. The potential advantage of this method can be evidenced through the differences in CT mechanics between the present study and the previous studies on *individual* CT. We have also provided a detailed understanding of the spatial variations in the CT stretch, finding localized stretches near the leaflet insertion or PM attachment, which may be an indicator of potential *in vivo* failure modes. These findings facilitate a greater understanding of the CT mechanics, which can be incorporated into existing AHV computational models for a refined simulation of valve behaviors. With future extensions, such models could also be used to guide and evaluate refinements of current therapies for diseases CT, such as the ePTFE suture.

CHAPTER 5 – MICROSTRUCTURE-MECHANICS RELATIONSHIPS OF THE CT-LEAFLET INSERTION

Earlier works on the mechanics of the CT-leaflet insertion were conducted by using mechanical testing devices or *in vitro* flow loops. For example, Sedransk *et al.* (2002) performed uniaxial tensile testing of the connected MV CT and leaflet and found the CT-leaflet insertion as the most rupture-vulnerable area of the chordae [106]. In another study, Chen *et al.* (2004) used a unique biaxial testing system where three edges of an MV anterior leaflet (MVAL) were attached via sutures, and the strut CT was mounted as the fourth edge using string [40]. From optical tracking-based surface strain quantification, they found that approaching the CT-leaflet insertion, the radial extensibility of the tissue decreased while the derived tangent modulus increased. In contrast to the use of mechanical testing devices, Padala *et al.* (2010) studied the MVAL strut CT-leaflet insertion using an *in vitro* flow loop in conjunction with marker-based optical tracking and found higher stretches in the edges of the insertion than in the center of the insertion [43]. Despite these research efforts, there is very limited information about connecting the load-dependent changes in the CFA to the mechanics of the CT-leaflet insertion.

Thus, the overall objective of this study is to fill this gap in knowledge for the CT-leaflet insertion of the AHVs (**Fig. 5-1a**) by establishing the interrelationship between the quantified mechanical properties of leaflet-CT-papillary muscle entities (**Fig. 5-1b**) and the changes in the underlying CFAs in response to the applied loading. This is achieved by utilizing an integrated instrument (**Fig. 5-1c**) that facilitates uniaxial mechanical testing and collagen fiber microstructural quantification based on polarized spatial frequency domain imaging (pSFDI) [108]. Through this pSFDI method, the load-dependent changes in the CFA, including the collagen

fiber orientation and the degree of optical anisotropy, of the CT-leaflet insertion are quantified by using the *same specimen* without the use of chemical fixatives, offering an advantage compared to the previous histological or *in vitro* flow loop study [40, 43]. Findings of the present work will be useful for gaining a better understanding of the microstructure-mechanics relationships in the atrioventricular heart valves, especially the CT-leaflet insertion, and ultimately would lead to an improvement of treatments for heart valve disease, such as the synthetic chordae replacements [109, 110].

The remaining of this chapter is organized as follows. Section 5.1 contains the experimental procedures for the polarized spatial frequency domain imaging and uniaxial testing. Then, the results are detailed in Section 5.2, including the quantified changes in the load-dependent collagen fiber architectures of the chordae-leaflet insertion, and findings on the mechanics of the leaflet-CT-PM entities. The implications of the results for the AHV biomechanics field are then summarized in Section 5.3.

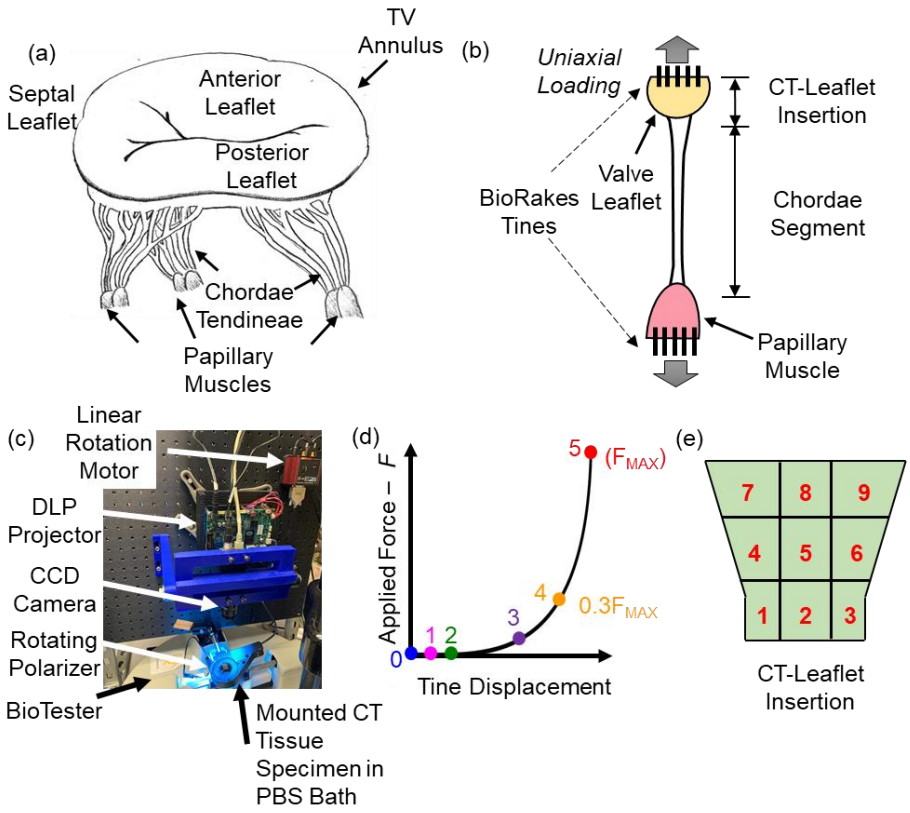

Figure 5-1. (a) Illustration of a tricuspid valve and its sub-valvular components. (b) Schematic of the leaflet-strut CT-papillary muscle entity-based tissue specimen dissected from porcine mitral valves and tricuspid valves under investigation. (c) Integrated instrument for conducting uniaxial mechanical testing and collagen fiber microstructural quantification. (d) Six loading points defined along the force-displacement curve for acquiring load-dependent CFAs. (e) Schematic of the sub-regions for analyzing the regional variations in the quantified CFAs for the CT-leaflet insertion.

5.1 Methods

5.1.1 Tissue Preparation

Healthy porcine hearts (80-140 kg of weight, 1-1.5 years of age, 1:1 female-to-male ratio) were obtained from a local USDA-approved abattoir (Chickasha Meat Co., Chickasha, OK, USA)

within 12 hours of animal sacrifice. Hearts were transported to the laboratory, cleansed of blood clots, and stored in a freezer at -20 °C until later testing. Freezing has been a common practice for effective tissue storage, and prior studies have shown minimal changes in the tissue mechanics of heart valve leaflets and other connective tissues following freezer storage [17, 63, 64, 111, 112].

At the time of tissue testing, hearts were thawed and dissected to remove the leaflet-CT-papillary muscle entities from the MV and TV anterior leaflets (**Fig. 5-1a**) according to our previously-developed procedure [113]. In brief, the strut chordae tendineae were extracted such that the attachments to the leaflet and papillary muscle (PM) were preserved, allowing for the specimen to be considered as a whole entity (**Fig. 5-1b**). In this work, strut chordae tendineae were used, as opposed to the basal or marginal chordae, because the strut CT are the most critical subset for carrying the mechanical load *in vivo* [92]. Once the leaflet-CT-PM entity specimens were prepared, the chordae thickness was optically measured using a 12-megapixel camera under microscopy (AmScope, Irvine, CA, USA) and analyzed in the ImageJ software (National Institute of Health, Bethesda, MD, USA). Thickness measurements were taken at three locations along the central portion of the strut CT segment, and an average of the three thickness measurements was used for the subsequent tissue stress analysis (see Section 5.1.3).

By using tined-based BioRakes that pierced the leaflet and papillary muscles under a uniaxial testing setup (**Fig. 5-1b**), the leaflet-CT-PM entity specimens were then mounted to a commercial biaxial mechanical testing system equipped with 1.5N load cells – BioTester (CellScale Biomaterials Testing, Waterloo, ON, Canada). This tine-based tissue mounting mechanism allowed for planar, uniaxial deformation of the leaflet and papillary muscle attachments, emulating their respective *in vivo* mechanical interactions. The leaflet-CT-PM entity specimens were then submerged in phosphate-buffered saline (PBS) and heated to 32 °C. A temperature slightly lower

than the body temperature (37 °C) was used to avoid issues related to fogging of the polarizer lens during the pSDFI-based collagen microstructural quantification procedure, as will be described in Section 5.1.5.

5.1.2 Uniaxial Mechanical Testing of the Leaflet-CT-PM Entity Specimens

For uniaxial mechanical testing (**Fig. 5-1c**), MVAL and TVAL strut chordae entities (n=12 for each valve) were tested in the following three steps: preconditioning, pSFDI at various deformation states, and mechanical testing. In the preconditioning step, leaflet-CT-PM entity specimens were cyclically loaded and unloaded 10 times at a rate of 4.42 N/min to reach the targeted force, $F_{\max}$, of 1.4 or 1.2N for the MVAL or TVAL strut chordae, respectively. The targeted force was selected based on the physiologic loading experienced by the strut CT, as determined in a previous *in vitro* study [97]. The last unloading cycle was then considered for determining the six loading points from the force-tine displacement curve (**Fig. 5-1d**) that were used in the subsequent pSFDI-based collagen microstructural quantifications. Following the pSFDI procedure (see Section 5.1.5), fiducial markers were positioned on the strut CT segment using a surgical pen, and five additional loading-unloading cycles were performed that targeted the same $F_{\max}$ as the one used in the preconditioning step. For the subsequent stress-stretch analysis, the final unloading cycle was used. Throughout testing, load cell force readings and CCD camera-captured images were recorded at 5 Hz by the LabJoy program of the CellScale BioTester.

5.1.3 Tissue Stress and Stretch Calculations for the Strut CT Segments

Following the mechanical testing, tissue stress and stretch were quantified following the methods in our previous work [113]. In brief, the digital image correlation (DIC) module of the LabJoy program was used to obtain the time-dependent coordinates of the centroid of the fiducial markers, i.e., (x_i, y_i) for the i^{th} fiducial marker. Then, the fiducial marker's *x*- and *y*-

displacements, (u_i, v_i), between any two loading states were determined. The tissue stretch, λ_i, of the CT segment between marker i and $i+1$ was calculated by using a 1D two-node linear finite element [114]

$$\lambda_i = 1 + \frac{1}{L_i}\left(d_{i+1} - d_i\right), \tag{5.1}$$

where $L_i = \sqrt{(x_{i+1} - x_i)^2 + (y_{i+1} - y_i)^2}$ is the distance between the two adjacent markers, and d_i are the displacements of these markers along the direction parallel to the CT segment's direction, i.e., $d_i = u_i \cos\theta + v_i \sin\theta$, $d_{i+1} = u_{i+1} \cos\theta + v_{i+1} \sin\theta$, and $\tan\theta = (y_{i+1} - y_i)/(x_{i+1} - x_i)$, and θ is the angle between the markers. Then, the tissue stretch of the CT segment was obtained by averaging the stretch values of those finite elements associated with the fiducial markers, i.e., $\lambda = \frac{1}{m}\sum_{i=1}^{m} \lambda_i$, where *m* is the number of 1D linear finite elements. The tissues' Cauchy stresses were determined by

$$\sigma = \left(\frac{F}{A_0}\right)\lambda \ , \tag{5.2}$$

where *F* is the applied force, and A_0 is the undeformed cross-sectional area. Chordae were idealized as a circular cross-sectional area, $\pi D^2/4$, where *D* is the measured (undeformed) thickness of the CT (see Section 5.1.2).

5.1.4 Constitutive Modeling of Tissue Mechanics for Strut CT Segments

To supplement the information on the tissue mechanics for the strut CT, constitutive modeling was performed, in which the CT were considered as nonlinear, isotropic, incompressible solids, modeled by the one-term Ogden hyperelastic model (p=1) [115]

$$\sigma = \mu\left(\lambda^{\alpha} - \lambda^{-\alpha/2}\right), \tag{5.3}$$

where σ is the Cauchy stress, λ is the tissue stretch as determined from Section 5.1.3, and μ and α are the two Ogden model parameters. The parameters μ and α represent the stress transition between the low- and high-tension regimes and the post-transition stiffness, respectively.

The two model parameters were determined by nonlinear least-squares fitting to the tissue stress-stretch data by using an in-house differential evolution optimization program (**Fig. 5-2**), considering a residual error tolerance of 10^{-10} [101]. To examine the goodness of fit, the normalized root-mean-square-deviation (NRMSD) was used, which is the square root of the average of the squared errors, normalized with respect to the maximum Cauchy stress value.

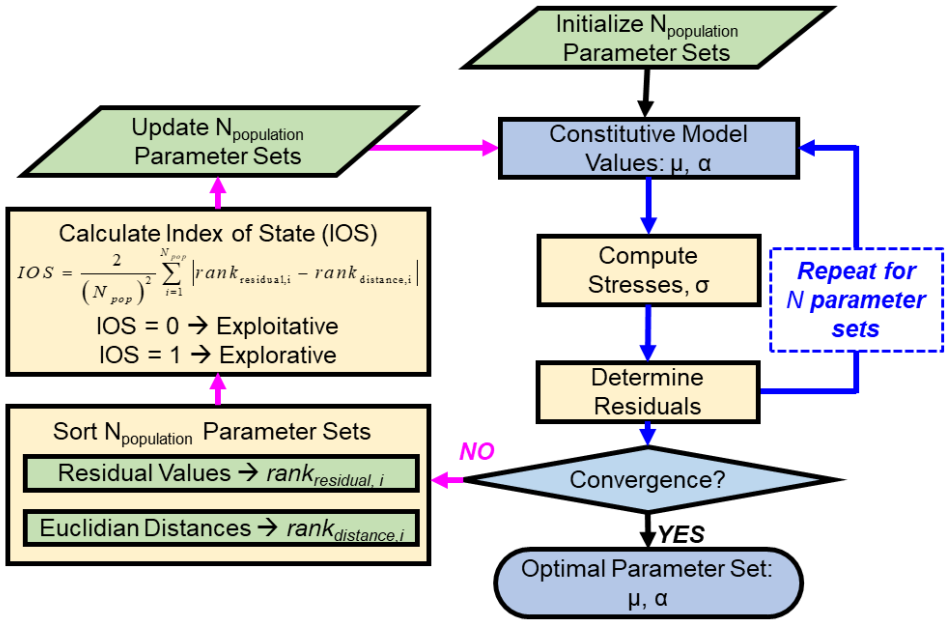

Figure 5-2. Algorithmic flowchart for the differential evolution optimization framework used in determining the Ogden-type constitutive model parameters.

5.1.5 pSFDI-based Collagen Fiber Microstructural Quantification

Following the procedure our lab developed for characterizing bovine tendon and representative MVALs [103], the pSFDI system (**Fig. 5-1c**) operates as follows: (i) the light shines

from a projector, (ii) the light passes through a polarizer at an angle $\theta_{\text{polarizer}}$ and onto the sample, (iii) the polarized light reflects from the sample's collagen fibers back through the same polarizer, and (iv) the intensity of the reflected light is captured by a camera. Steps (i-iv) are repeated with $\theta_{\text{polarizer}}$ ranging from 0° to 180° with a 5° increment.

The above-mentioned loading points of the force-displacement curve (**Fig. 5-1d**) were determined from an intermediate study, in which 9 different deformation states between the unloaded (relaxed) state Ω_0 and the peak loading $F_{\max}$ were considered. The above pSFDI procedure was performed at each of these deformation states, in which the MVAL or TVAL strut chordae entity was stretched at the corresponding tine displacement. Then, the CFA was analyzed from the acquired pSFDI data (see more details in Section 5.1.6), and the changes in the predicted collagen fiber angle θ_{fiber} and degree of optical anisotropy were quantified. The loading points were selected based on those with the most noteworthy changes, while keeping the total test duration to a reasonable timeframe. From our internal study, the loading points were determined as (**Fig. 5-1d**):

- *Loading Point 0* – tissue mounting configuration Ω_0
- *Loading Point 1* – intermediate point between Ω_0 and the post-preconditioning configuration Ω_1
- *Loading Point 2* – post-preconditioning configuration Ω_1
- *Loading Point 3* – intermediate point between Ω_1 and $0.3F_{\max}$
- *Loading Point 4* – 30% of the peak force $0.3F_{\max}$
- *Loading Point 5* – peak force $F_{\max}$.

After the preconditioning cycle, the integrated pSFDI-biaxial testing system (**Fig. 5-1c**) was used for capturing the birefringent light intensity responses of the CFA of the MVAL and TVAL leaflet-CT-PM entity specimens. The pSFDI procedure, as described previously, was repeated at

each of the six loading points, and the acquired images (1280x1024 pixels) were further analyzed. The images were then processed to determine the pixel-wise fiber orientation angle θ_{fiber} and the degree of optical anisotropy (DOA), a metric that is related to the alignment of the collagen fiber networks of the tissue (i.e., smaller values of DOA denote a random fiber network, whereas larger values of DOA signify highly-aligned fibers). The pSFDI image data analysis is described in Section 5.1.6. After the pSFDI procedure, the CT entity specimens were uniaxially tested using the procedure described in Section 5.1.2.

5.1.6 Analysis of pSFDI-based Collagen Microstructural Data

Tissue collagen fiber orientations were determined following the methods described in our previous work [103], and the theory outlined in Goth *et al*. (2016) [108]. In pSFDI, as $\theta_{\text{polarizer}}$ is rotated from 0° to 180° the intensity of the reflected polarized light *I* returns a bimodal response due to the birefringent response of the collagen fibers (**Fig. 5-3**).

The bimodal response contains a global maximum when $\theta_{\text{polarizer}}$ is equal to θ_{fiber}, and a local maximum when $\theta_{\text{polarizer}}$ is 90° offset from θ_{fiber}. The bimodal intensity response *I* can then be described using the 3-term Fourier series:

$$I = \gamma_0 + \gamma_2\left[2\left(\theta_{fiber} - \theta_{polarizer}\right)\right] + \gamma_4\left[4\left(\theta_{fiber} - \theta_{polarizer}\right)\right], \tag{5.4}$$

where the Fourier constants are γ_0, which represents the mean light intensity, and γ_2 and γ_4, which describe the optical anisotropies. The degree of optical anisotropy (DOA) can then be computed by

$$DOA = \frac{\gamma_2 + \gamma_4}{\gamma_0 + \gamma_2 + \gamma_4}. \tag{5.5}$$

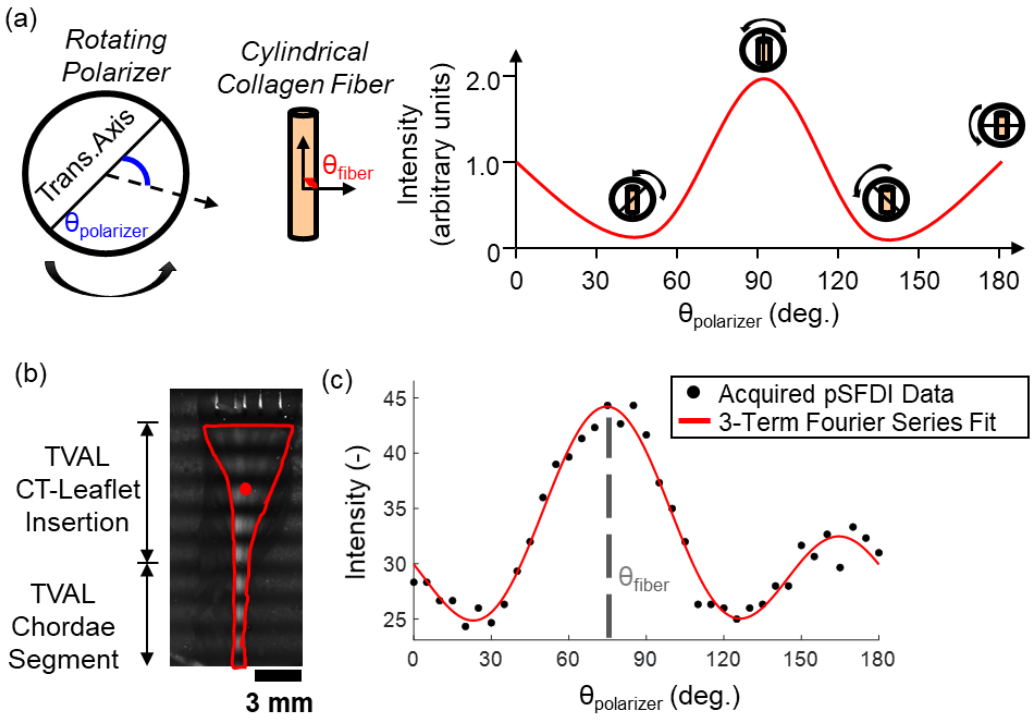

Figure 5-3. (a) Illustration of the birefringent reflected light intensity versus polarizer angle $\theta_{polarizer}$ for an example of a (cylindrical) collagen fiber with an orientation angle θ_{fiber}=90°, where the maximum intensity occurs when $\theta_{polarizer}$ and θ_{fiber} match each other. (b) pSFDI image from a representative TVAL strut CT-leaflet insertion, with the region of interest (ROI) of the tissue outlined in red, together with a selected pixel (red circle). (c) Measured reflected light intensity versus $\theta_{polarizer}$ from the analyzed pixel (red circle in (b)), superimposed with the 3-term Fourier series fit that shows how θ_{fiber} was determined.

For the investigations of the load-dependent changes in the CFA of the MVAL/TVAL strut chordae entities, two regions of interest (ROIs) were defined (**Fig. 5-1b** and **Fig. 5-3b**): (i) the CT segment (n=7 for MVAL; n=7 for TVAL) and (ii) the CT-leaflet insertion (n=10 for MVAL; n=8 for TVAL). Variations in the number of available specimens in the pSFDI data analysis were due to the limited field of view within the polarizer lens window. Within the analyzed ROIs, the

average θ_{fiber}, the average DOA, and the percent differences in the DOA were quantified to evaluate changes in the CFA in response to mechanical loads.

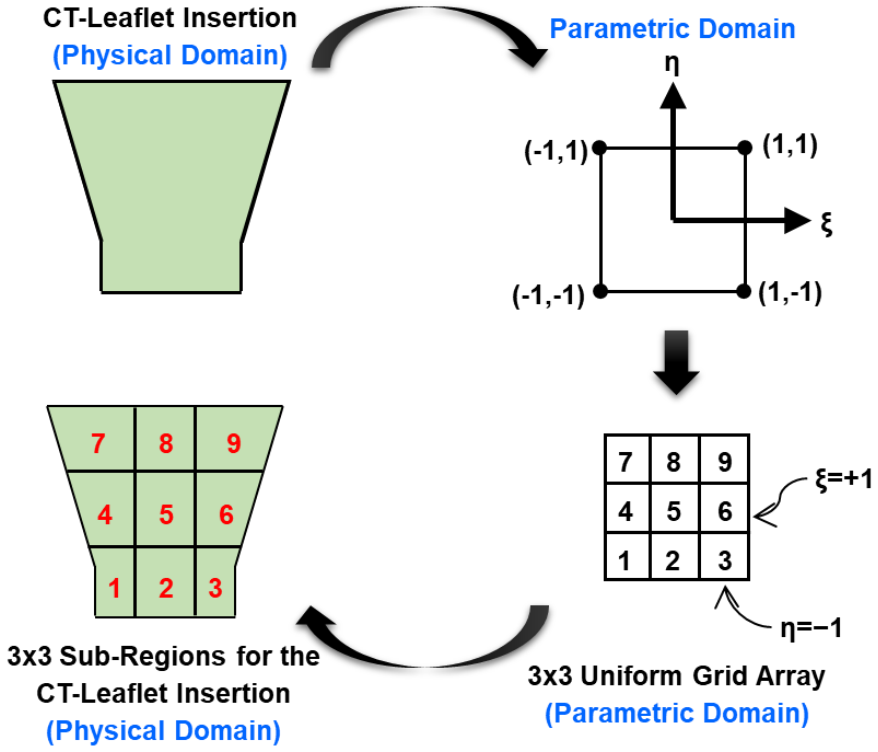

Figure 5-4. Schematic of the procedure for generating the sub-regions of the load-dependent CFAs of the CT-leaflet insertions. The isoparametric mapping concept was adopted, and the uniform 3x3 grid was generated in the parametric domain and mapped back to the CT-leaflet insertion in the physical domain.

To further examine the spatial variations in the CFA, the CT-leaflet insertion was subdivided into 9 sub-regions using a uniform 3x3 grid (**Fig. 5-1e**). To elaborate, the ROI of the CT-leaflet insertion was transformed to a parametric space (similar to the isoparametric mapping concept in the finite element methods [114]), and the 3x3 grid array was generated to ensure uniformity in

the physical domain (**Fig. 5-4**). Within each sub-region, the average θ_{fiber}, the average DOA, and the percent changes in the DOA were analyzed and reported.

5.1.7 Statistical Analysis

Data from the uniaxial mechanical testing of the chordae entities was visualized using whisker box plots to depict the mean, median, the first and third quartiles, the minimum and maximum, and the individual data points. Statistical comparisons were not performed for the uniaxial mechanical data due to the differences in the testing conditions between the MVAL and TVAL chordae entities.

To determine statistically-significant changes in θ_{fiber} and the DOA between the six loading points for the MVAL or TVAL chordae entities, one-way analysis of variance (ANOVA) was performed using an in-house MATLAB program (MathWorks, Natick, MA). For ANOVA, comparisons were only made between specimens within their respective groups: the MVAL or the TVAL chordae entities. To verify the use of one-way ANOVA, quantile-quantile (QQ) plots were generated to confirm the general normality of the data. If a p-value <0.05 was found in the one-way ANOVA, a multiple comparison was next performed by using the `multcompare` function of MATLAB to determine significant differences pairwise between each loading point. In this study, we considered p-values <0.05 as statistically significant, indicating that the quantified DOA or the predicted fiber orientation angle was significantly different between the compared loading points.

5.2 Results

5.2.1 Thickness Measurement, Mechanical Testing and Constitutive Modeling Results

The tissue thicknesses were found as 0.86±0.07 mm and 1.19±0.08 mm for the TVAL and the MVAL strut CT, respectively (**Fig. 5-5a**). Using the tissue thicknesses and the recorded load cell force readings from uniaxial testing, the Cauchy stresses were computed and reported as follows: 2.54±0.32 MPa for the TVAL strut CT entities and 1.49±0.21 MPa for the MVAL strut CT entities (**Fig. 5-5b**). In addition, the stretches for the TVAL and MVAL strut CT entities were 1.027±0.004 and 1.028±0.005, respectively (**Fig. 5-5c**). The Ogden model parameters (**Fig. 5-5d-e**), were reported as follows: parameter μ =176.54±42.11 kPa and parameter α =128.53±13.43 for the TVAL strut CT, and μ =26.10±7.95 kPa and α = 210.94±19.02 for the MVAL strut CT. For all the parameter estimations, the NRMSD was less than 0.1, suggesting a good fit in our estimations.

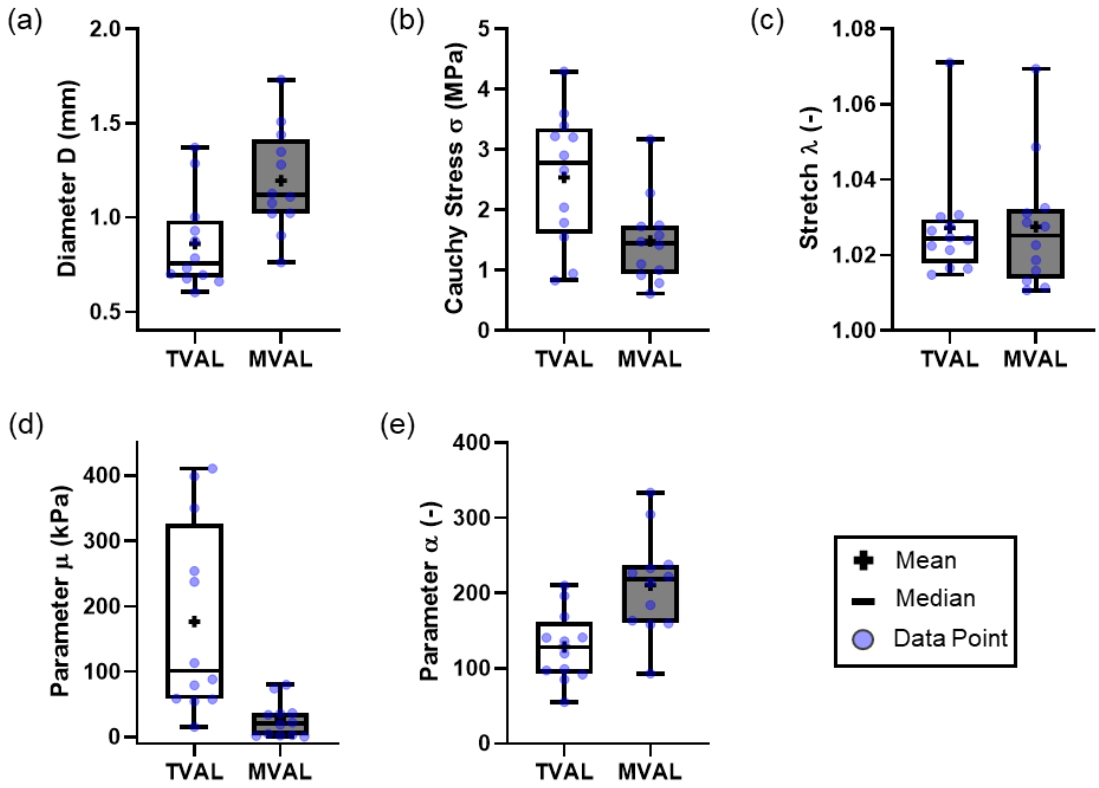

Figure 5-5. Whisker box plots for (a) the thickness, (b) the Cauchy stress σ, (c) the tissue stretch λ, and (d-e) the Ogden model parameters, μ and α, for the TVAL and MVAL CT segments.

5.2.2 Collagen fibers architecture quantification results

Representative pSFDI-quantified load-dependent CFA results from an individual TVAL and MVAL strut CT entity are shown in **Figs. 5-6**, **5-7**, respectively. We noticed that the collagen fibers in both the CT-leaflet insertion and the CT segment were predominantly oriented towards the loading direction (i.e., θ_{fiber} =90°). Interestingly, the average θ_{fiber} for the strut CT entity had a minimal change in response to the applied uniaxial loading (i.e., changes between tissue mounting and peak loading: <4% for the representative TVAL and <1% for the representative MVAL). In contrast, noticeable changes were found in the quantified DOA with increased loading (i.e., up to

29 and 45% changes for the representative TVAL and MVAL CT segments, respectively, between tissue mounting and peak loading). Furthermore, for both representative specimens, we saw the largest increase in the DOA between Loading Point 4 ($0.3F_{max}$) and Loading Point 5 (F_{max}).

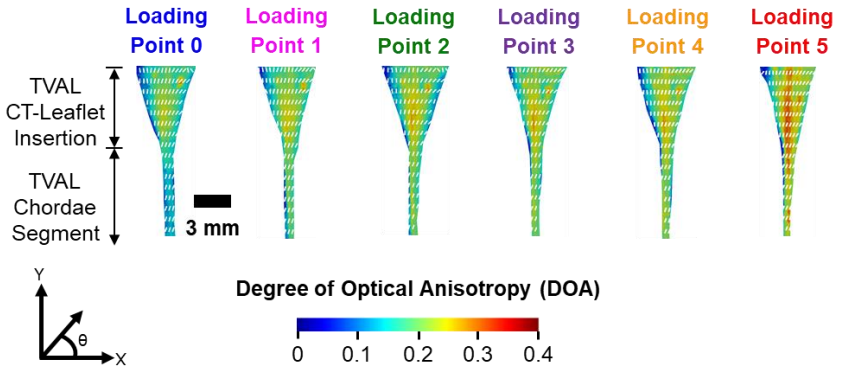

Figure 5-6. Progressive CFAs of a representative TVAL strut chordae entity specimen under uniaxial mechanical testing (~38,000 pixels in the analyzed region). The white lines represent the predicted collagen fiber orientations of the selected coarser pixels (for visualization purpose), and the colormap intensities signify the degree of optical anisotropy (DOA). Values of the predicted θ_{fiber} and DOA are presented as mean±SEM.

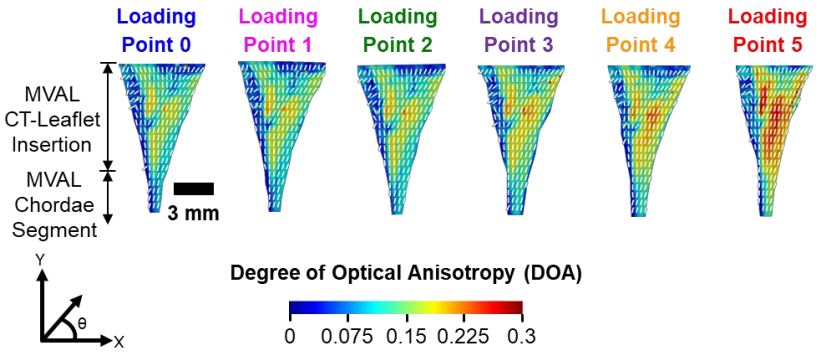

Figure 5-7. Progressive CFAs of a representative MVAL strut chordae entity specimen under uniaxial mechanical testing (~15,000 pixels in the analyzed region). The white lines represent the predicted collagen fiber orientations of selected coarser pixels (for visualization purpose), and the colormap intensities signify the degree of optical anisotropy (DOA). Values of the predicted θ_{fiber} and DOA are presented as mean±SEM.

In the following subsections the load-dependent CFA results, as quantified by pSFDI, are presented for the *CT segment*, the *CT-leaflet insertion*, and the *sub-regions of the CT-leaflet insertion*, respectively. In these results, we focused on comparing the changes in the quantified θ_{fiber} and DOA between any two sequential loading points, or between two selected non-sequential loading points, i.e., between Loading Point 0 and Loading Point 5 (i.e., tissue mounting vs. peak loading), and between Loading Point 2 and Loading Point 5 (i.e., post-preconditioning vs. peak loading).

5.2.2.1 Load-dependent changes in the CFA for the CT segment

For the CT segments (see the schematic definition in **Fig. 5-1b**), we did not notice significant changes in θ_{fiber} with increased loading (TVAL, p=0.975; MVAL, p=0.998, **Table 5-1**). In general, across all the six loading points, the predicted θ_{fiber} was ~66° for the TVAL CT segments, and ~73° for the MVAL CT segments. On the other hand, we did observe notable changes in the

quantified DOA in response to the applied loads, with several key findings summarized as follows. First, we found that the DOAs in the TVAL CT segments are generally larger than those in the MVAL CT segments, suggesting a better alignment of collagen fibers in the TVAL CT than their MVAL counterparts (TVAL, DOA=0.14-0.20; MVAL, DOA=0.09-0.15, **Table 5-1**). Note that statistical comparisons were not made between the TVAL and the MVAL, because the target peak loads were different for the specimens from the two AHVs. Second, when considering changes in the DOA between the sequential loading points, the TVAL CT segments had larger increases between Loading Point 4 and Loading Point 5 (20.4±2.6%) than between the other sequential loading points (-0.5-7.1%) (**Table 5-2**). In contrast, for the MVAL CT segments, the increases in the DOA between the sequential loading points were very similar, i.e., 13.9±3.5% changes between Loading Point 2 and Loading Point 3, 13.3±9.5% changes between Loading Points 3 and 4, and 11.4±5.5% changes between Loading Point 4 and Loading Point 5. Thirdly, when comparing the changes in the DOA between the non-sequential loading points, there were statistically-significant changes found in the TVAL CT segments both between Loading Point 0 and Loading Point 5 (35.6±7.0%, $p<0.001$), and between Loading Point 2 and Loading Point 5 (25.3±4.2%, $p=0.001$). For the MVAL CT, a statistically-significant change in the DOA was only found between Loading Point 0 and Loading Point 5 (46.4±8.7%, $p=0.036$), but not between Loading Point 2 and Loading Point 5 (38.3±7.5%, $p=0.126$).

Table 5-1. Quantified collagen fiber architecture, including the predicted collagen fiber orientation angle θ_{fiber} and the predicted degree of optical anisotropy (DOA), for the CT segments (see **Fig. 5-1b**). Values are reported as mean±SEM.

		Loading Point					
		0	1	2	3	4	5
TVAL (n=7)	θ_{fiber}	65.6±2.3°	66.5±1.9°	66.6±1.8°	66.1±1.7°	66.1±2.1°	64.4±1.3°
	DOA	0.14±0.01	0.15±5E-3	0.16±0.01	0.17±0.01	0.17±0.01	0.20±0.01
MVAL (n=7)	θ_{fiber}	71.9±3.0°	72.3±2.8°	72.1±2.9°	72.4±2.9°	73.9±3.6°	72.7±3.3°
	DOA	0.09±0.01	0.09±0.01	0.10±0.01	0.11±0.01	0.13±0.02	0.15±0.01

Note: Variations in the number of specimens were due to limitations with the camera field of view not allowing a full visibility of the ROIs within the polarizer lens window.

Table 5-2. Percentage changes in the predicted degree of optical anisotropy (DOA) between two consecutive states of the 5 loading points for the CT segments (see **Fig. 5-1b**). Values are reported as mean±SEM, and p-values determined from the one-way ANOVA are given in square brackets.

TVAL Strut Chordae Tendineae ROI (n=7)					
Loading Point	Loading Point as the Reference (Baseline)				
	0	1	2	3	4
0	–	–	–	–	–
1	7.1±4.7% [0.932]	–	–	–	–
2	10.7±7.8% [0.622]	3.6±5.6% [0.987]	–	–	–
3	16.1±6.8% [0.195]	9.1±3.8% [0.712]	5.5±2.3% [0.968]	–	–
4	15.7±6.8% [0.214]	8.7±3.3% [0.741]	5.0±4.0% [0.976]	-0.5±2.6% [1.000]	–
5	35.6±7.0% [1E-5]*	28.9±4.5% [2E-4]*	25.3±4.2% [0.002]*	19.9±3.1% [0.013]*	20.4±2.6% [0.012]*
MVAL Strut Chordae Tendineae ROI (n=7)					
Loading Point	Loading Point as the Reference (Baseline)				
	0	1	2	3	4
0	–	–	–	–	–
1	0.3±3.1% [1.000]	–	–	–	–
2	8.7±6.0% [0.993]	8.4±4.3% [0.996]	–	–	–
3	22.5±5.6% [0.790]	22.3±4.0% [0.821]	13.9±3.5% [0.976]	–	–
4	35.1±11.4% [0.167]	35.0±10.3% [0.187]	26.6±11.5% [0.420]	13.3±9.5% [0.851]	–
5	46.4±8.7% [0.036]*	46.3±7.5% [0.042]*	38.3±7.5% [0.126]	25.0±5.1% [0.444]	11.4±5.5% [0.982]

Note: Variations in the number of specimens were due to limitations with the camera field of view not allowing a full visibility of the ROIs within the polarizer lens window.

* statistically-significant changes ($p<0.05$).

5.2.2.2 Load-dependent changes in the CFA for the CT-leaflet insertion

For the strut CT-leaflet insertion (see the schematic definition in **Fig. 5-1b**), the predicted θ_{fiber} did not vary significantly with the applied loading (TVAL, p=0.615; MVAL, p=0.990). Across all the six loading states, θ_{fiber} was found to be ~72° and ~78° for the TVAL and MVAL CT-leaflet insertions, respectively (**Table 5-3**). In contrast, there were some noticeable increases in the quantified DOAs with increased applied loads (**Table 5-3**). For example, considering the sequential loading points, we observed the largest increase in the DOA for the CT-leaflet insertions between Loading Point 4 and Loading Point 5 (TVAL: 18.3±2.6%, p=0.202; MVAL: 15.6±2.4%, p=0.039) (**Table 5-4**). For the TVAL CT-leaflet insertions, the second largest increase in the DOA was from Loading Points 0 to 1 (7.4±1.2%, p=0.980), whereas it was from Loading Points 2 to 3 for the MVAL CT-leaflet insertions (9.9±2.5%, p=0.567).

Considering the non-sequential loading points, there were statistically-significant differences in the DOA for the TVAL CT-leaflet insertions between Loading Point 0 and Loading Point 5 (i.e., tissue mounting vs. peak loading, 37.7±4.0%, p=0.002), and between Loading Points 2 and 5 (i.e., post-preconditioning vs. peak loading, 25.3±3.7%, p=0.032). Similarly, for the MVAL CT-leaflet insertions, statistically-significant differences in the DOA were found between Loading Point 0 and Loading Point 5 (37.5±2.8%, p<0.001), and between Loading Point 2 and Loading 5 (30.2±2.4%, p<0.001).

Table 5-3. Quantified collagen fiber architecture, including the predicted collagen fiber orientation angle θ_{fiber} and the predicted degree of anisotropy (DOA), for the CT-leaflet insertions (see **Fig. 5-1b**). Values are reported as mean±SEM.

		Loading Point					
		0	1	2	3	4	5
TVAL (n=8)	θ_{fiber}	73.7±2.4°	73.2±2.3°	72.6±2.7°	70.9±2.3°	70.5±2.1°	68.6±1.75°
	DOA	0.13±0.01	0.14±0.01	0.14±0.01	0.15±0.01	0.15±0.01	0.19±0.01
MVAL (n=10)	θ_{fiber}	78.2±1.8°	78.0±1.7°	77.9±1.9°	78.2±1.5°	78.1±1.6°	76.6±2.0°
	DOA	0.11±4E-3	0.11±5E-3	0.12±5E-3	0.13±0.01	0.14±0.01	0.16±0.01

Note: Variations in the number of specimens were due to limitations with the camera field of view not allowing a full visibility of the ROIs within the polarizer lens window.

Table 5-4. Percentage changes in the predicted degree of optical anisotropy (DOA) between two consecutive states of the 5 loading points for the CT-leaflet insertions (see **Fig. 5-1b**). Value are reported as mean±SEM, and p-values, determined from the one-way ANOVA, are given in square brackets.

TVAL Strut CT-Leaflet Insertion (n=8)					
Loading Point	Loading Point as the Reference (Baseline)				
	0	1	2	3	4
0	–	–	–	–	–
1	7.4±1.2% [0.980]	–	–	–	–
2	12.7±2.1% [0.833]	5.3±2.0% [0.996]	–	–	–
3	18.6±2.6% [0.393]	11.2±2.2% [0.821]	5.9±1.6% [0.976]	–	–
4	19.9±2.6% [0.345]	12.5±2.1% [0.774]	7.2±2.1% [0.961]	1.3±1.2% [1.000]	–
5	37.7±4.0% [0.001]*	30.5±3.8% [0.009]*	25.3±3.7% [0.032]*	19.6±2.7% [0.171]	18.3±2.6% [0.202]
MVAL Strut CT-Leaflet Insertion (n=10)					
Loading Point	Loading Point as the Reference (Baseline)				
	0	1	2	3	4
0	–	–	–	–	–
1	3.2±2.5% [0.996]	–	–	–	–
2	7.5±3.4% [0.855]	4.4±1.8% [0.985]	–	–	–
3	17.3±2.8% [0.071]	14.2±2.6% [0.205]	9.9±2.5% [0.567]	–	–
4	22.2±3.5% [0.006]*	19.1±3.0% [0.024]*	14.7±2.9% [0.119]	4.9±1.4% [0.938]	–
5	37.5±2.8% [1E-7]*	34.4±2.5% [8E-7]*	30.2±2.4% [9E-6]*	20.5±2.7% [0.003]*	15.6±2.4% [0.004]*

Note: Variations in the number of specimens were due to limitations with the camera field of view not allowing a full visibility of the ROIs within the polarizer lens window.

* statistically-significant changes ($p<0.05$).

5.2.2.3 Load-dependent changes in the predicted fiber orientation angle for the sub-regions in the CT-leaflet insertion

From the sub-regional analysis of the load-dependent CFA results of the TVAL and MVAL CT-leaflet insertions (**Fig. 5-1e**), we observed that collagen fibers were more aligned toward the primary loading direction (i.e., 90°) on the left edge (sub-regions 1, 4, and 7) than in the center (sub-regions 2, 5, and 8) and on the right edge (sub-regions 3, 6, and 9) (**Tables 5-6**, **5-7**). Interestingly, although we did not notice discernible changes in the predicted θ_{fiber} when the CT-leaflet insertion was analyzed as one whole entity in Section 5.2.2.2, there were some statistically-significant changes in the predicted θ_{fiber} after dividing the CT-leaflet insertion into the sub-regions. For example, when we analyzed the sequential loading points, statistically-significant changes in θ_{fiber} were found between Loading Point 4 and Loading Point 5: sub-region 8 of the TVAL CT-leaflet insertion (-1.19±0.95%, p=0.037), and sub-region 5 (0.71±1.16%, p=0.018) and sub-region 8 (-4.61±1.69%, p=0.002) of the MVAL CT-leaflet insertion.

Table 5-5. Regional analyses of the quantified collagen fiber architecture for the TVAL CT-leaflet insertion (n=8, see **Fig. 5-1e**). Values are reported as mean±SEM.

Quantified Collagen Fiber Orientation Angle (θ_{fiber})						
Loading Point	0	1	2	3	4	5
Sub-region 1	77.3±3.5°	77.5±2.9°	77.1±3.4°	77.3±3.0°	75.4±3.1°	72.4±2.8°
Sub-region 2	68.2±2.9°	68.4±2.6°	67.6±3.3°	67.0±2.9°	64.6±3.1°	64.1±2.3°
Sub-region 3	64.9±2.9°	62.5±2.7°	64.4±2.8°	60.7±2.1°	66.6±3.2°	61.4±2.0°
Sub-region 4	86.3±2.5°	86.4±2.3°	85.8±3.2°	85.0±3.0°	83.5±3.5°	80.9±3.0°
Sub-region 5	69.7±3.4°	69.0±3.2°	67.8±2.8°	66.3±3.4°	65.6±3.3°	64.9±2.2°
Sub-region 6	65.1±4.7°	63.9±4.9°	66.5±6.4°	63.9±4.8°	63.1±4.0°	61.8±3.0°
Sub-region 7	89.6±2.6°	89.9±2.5°	87.7±2.9°	86.3±2.3°	85.0±2.3°	83.6±2.3°
Sub-region 8	72.2±2.9°	71.9±2.9°	70.0±2.4°	69.5±3.4°	69.2±3.3°	68.3±2.9°
Sub-region 9	69.7±4.4°	69.1±5.6°	66.8±5.4°	62.4±5.1°	61.2±3.8°	60.3±2.3°
Quantified Degree of Optical Alignment (DOA)						
Loading Point	0	1	2	3	4	5
Sub-region 1	0.11±0.01	0.12±0.01	0.13±0.01	0.14±0.01	0.15±0.01	0.18±0.01
Sub-region 2	0.16±0.01	0.17±0.01	0.17±0.01	0.18±0.01	0.18±0.01	0.23±0.02
Sub-region 3	0.12±0.01	0.14±0.01	0.13±0.01	0.16±0.01	0.14±0.01	0.18±0.02
Sub-region 4	0.11±0.01	0.12±0.01	0.13±0.01	0.14±0.01	0.14±0.01	0.17±0.01
Sub-region 5	0.15±0.01	0.16±0.01	0.17±0.01	0.17±0.01	0.18±0.01	0.22±0.01
Sub-region 6	0.12±0.01	0.13±0.01	0.13±0.01	0.14±0.02	0.13±0.02	0.16±0.02
Sub-region 7	0.10±0.01	0.11±0.01	0.12±0.01	0.13±0.01	0.13±0.01	0.14±0.02
Sub-region 8	0.14±0.01	0.15±0.01	0.16±0.01	0.16±0.01	0.18±0.01	0.22±0.01
Sub-region 9	0.12±0.01	0.13±0.01	0.14±0.01	0.15±0.01	0.15±0.01	0.18±0.02

Note: Variations in the number of specimens were due to limitations with the camera field of view not allowing a full visibility of the ROIs within the polarizer lens window.

Table 5-6. Regional analyses of the quantified collagen fiber architecture for the MVAL CT-leaflet insertion (n=10, see **Fig. 5-1e**). Values are reported as mean±SEM.

Quantified Collagen Fiber Orientation Angle (θ_{fiber})						
Loading Point	0	1	2	3	4	5
Sub-region 1	82.2±2.8°	83.1±2.8°	83.1±2.5°	83.7±2.7°	84.0±2.9°	83.3±2.6°
Sub-region 2	72.6±3.2°	73.0±3.3°	73.3±3.3°	73.1±3.3°	73.0±3.5°	73.6±3.6°
Sub-region 3	68.2±1.9°	67.6±1.6°	66.2±2.0°	69.3±3.5°	69.6±3.2°	67.0±3.3°
Sub-region 4	93.3±1.5°	92.6±1.5°	92.6±1.8°	92.6±1.2°	91.2±1.6°	89.9±1.4°
Sub-region 5	73.3±3.6°	71.6±3.4°	73.0±3.3°	73.0±3.3°	72.3±3.4°	72.8±3.3°
Sub-region 6	65.9±2.3°	68.4±3.4°	67.1±3.3°	66.5±4.1°	67.9±4.0°	66.9±3.1°
Sub-region 7	100.2±2.9°	101.9±1.6°	100.3±1.8°	99.8±2.1°	98.0±1.7°	95.2±2.0°
Sub-region 8	80.0±4.3°	77.1±4.0°	78.5±4.2°	77.7±4.0°	77.0±3.3°	73.6±3.1°
Sub-region 9	67.8±2.9°	66.5±2.3°	67.3±3.2°	67.7±3.1°	69.5±2.8°	67.5±2.6°
Quantified Degree of Optical Alignment (DOA)						
Loading Point	0	1	2	3	4	5
Sub-region 1	0.10±0.01	0.10±0.01	0.11±0.01	0.13±0.01	0.13±0.01	0.14±0.01
Sub-region 2	0.12±0.01	0.13±0.01	0.14±0.01	0.16±0.01	0.17±0.01	0.20±0.01
Sub-region 3	0.11±0.01	0.12±0.01	0.12±0.01	0.14±0.01	0.15±0.01	0.18±0.01
Sub-region 4	0.11±0.01	0.11±0.01	0.11±0.01	0.12±0.01	0.13±0.01	0.14±0.01
Sub-region 5	0.14±0.01	0.14±0.01	0.15±0.01	0.16±0.01	0.17±0.01	0.21±0.01
Sub-region 6	0.12±0.01	0.12±0.01	0.13±0.01	0.14±0.01	0.15±0.01	0.18±0.01
Sub-region 7	0.09±0.01	0.09±0.01	0.09±0.01	0.10±0.01	0.11±0.01	0.11±0.01
Sub-region 8	0.11±0.01	0.11±3E-3	0.12±3E-3	0.12±3E-3	0.13±0.01	0.16±3E-3
Sub-region 9	0.10±0.01	0.10±0.01	0.11±0.01	0.12±0.01	0.12±0.01	0.14±0.01

Note: Variations in the number of specimens were due to limitations with the camera field of view not allowing a full visibility of the ROIs within the polarizer lens window.

Considering the non-sequential loading points, statistically-significant differences in θ_{fiber} were found in several sub-regions of the TVAL CT-leaflet insertion between Loading Point 0 and Loading Point 5 (i.e., tissue mounting vs. peak loading, sub-region 1: -6.35±1.85%, p=0.015, sub-region 2: -5.99±1.48%, p=0.005, sub-region 4: -6.60±1.98%, p=0.008, sub-region 5: -6.73±2.26%, p=0.008, and sub-region 8: -5.70±1.95%, p<0.001), as well as between Loading Point 2 and Loading Point 5 (i.e., post-preconditioning vs. peak loading, sub-region 8: -2.69±1.63%, p<0.001). On the other hand, in the MVAL CT-leaflet insertions, statistically-significant differences in θ_{fiber} were found between Loading Point 0 and Loading Point 5 (sub-region 1: 1.38±2.78%, p=0.025,

sub-region 2: 1.11±1.42%, p<0.001, sub-region 3: -2.51±3.46%, p<0.001, sub-region 5: -0.59±1.62%, p<0.001, sub-region 6: 1.17±2.09%, p=0.008, and sub-region 8: -7.79±1.98%, p<0.001), and between Loading Point 2 and Loading Point 5 (sub-region 2: 0.21±1.13%, p<0.001, sub-region 3: 0.55±2.54%, p<0.001, sub-region 5: -0.32±1.27%, p<0.001, sub-region 6: -0.14±1.87%, p=0.023, and sub-region 8: -5.90±1.95%, p<0.001).

5.2.2.4 Load-dependent changes in the quantified DOA for the sub-regions in the CT-leaflet insertion

Considering the load-dependent changes in the quantified DOAs between the sequential loading points, we observed the largest change from Loading Points 4 to 5, and the smallest from Loading Points 3 to 4 (**Fig. 5-8** and **Tables 5-5**, **5-6**). Specifically, we found a statistically-significant increases in the DOA between Loading Point 4 and Loading Point 5 for sub-region 8 (20.63±3.87%, p=0.037) of the TVAL CT-leaflet insertions, as well as sub-region 5 (18.19±3.05%, p=0.018) and sub-region 8 (20.47±4.26%, p=0.017) of the MVAL CT-leaflet insertions. We generally found an increase in the DOA with increased loading; however, we did notice decreases in the DOA between some sequential loading points, i.e., between Loading Point 0 to Loading Point 1: sub-region 4 (-1.76±2.65%, p=0.999) and sub-region 6 (-1.39±4.31%, p=0.999) of the MVAL CT-leaflet insertions; between Loading Point 3 to Loading Point 4: sub-region 3 (-17.32±7.90%, p>0.05) of the TVAL CT-leaflet insertions, and sub-region 1 (0.05±7.92%, p=0.999) and sub-region 6 (6.00±3.24%, p=0.994) of the MVAL CT-leaflet insertions.

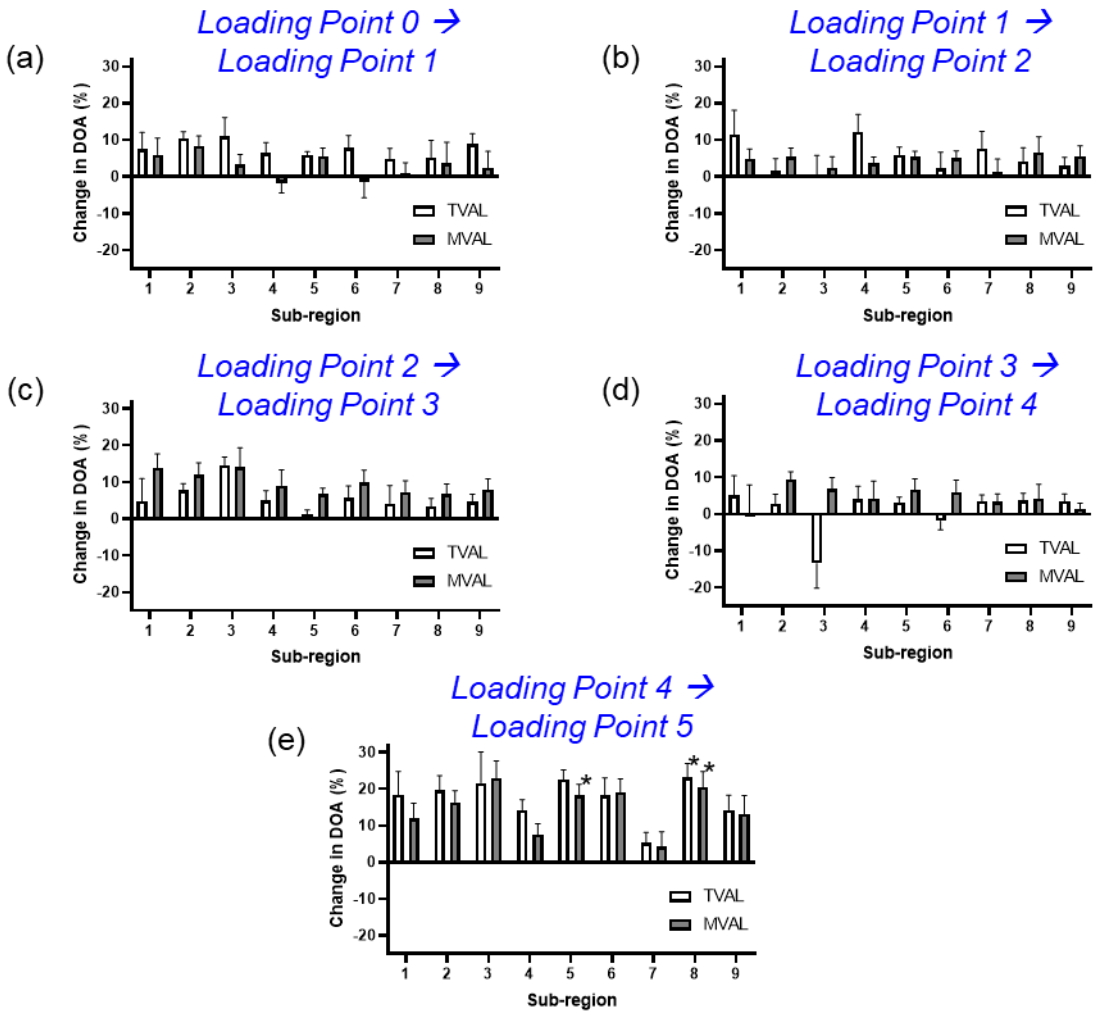

Figure 5-8. Comparison of the predicted DOAs of the CT-leaflet insertions between the sequential loading points from the 3x3 sub-regional analysis: (a) Loading Points 0 vs. 1, (b) Loading Points 1 vs. 2, (c) Loading Points 2 vs. 3, (d) Loading Points 3 vs. 4, and (e) Loading Points 4 vs. 5. Values are presented as mean±SEM, and * denotes a statistically significant change, as obtained through one-way ANOVA ($p<0.05$).

Additionally, changes in the quantified DOA between the non-sequential loading states were also found between Loading Point 0 and Loading Point 5 (i.e., tissue mounting vs. peak loading), and between Loading Point 2 and Loading Point 5, i.e., post-preconditioning vs. peak loading

(**Table 5-7**). Specifically, for the TVAL CT-leaflet insertions, the largest increase in the DOA was found to be sub-region 1 (46.3±6.2%, $p=0.015$) between Loading Point 0 and Loading Point 5, and sub-region 2 (50.1±4.8%, $p=0.053$) between Loading Point 2 and Loading Point 5. In contrast, for the MVAL CT-leaflet insertions, the largest increase in the DOA was observed in sub-region 2 from Loading Points 0 to 5 (37.3±2.6%, $p<0.001$) and from Loading Points 2 to 5 (30.0±3.1%, $p<0.001$). Moreover, statistically-significant increases in the quantified DOA for the non-sequential loading were found between Loading Point 0 to Loading Point 5: sub-regions 1, 2, 4, 5, 8, and 9 of the TVAL CT-leaflet insertions ($0.001<p<0.016$), and sub-regions 1, 2, 3, 5, 6, and 8 of the MVAL CT-leaflet insertions ($0.001<p<0.025$), as well as between Loading Points 2 and Loading Point 5: sub-region 8 of the TVAL CT-leaflet insertions ($p<0.001$), and sub-regions 2, 3, 5, 6, and 8 of the MVAL CT-leaflet insertions ($0.001<p<0.023$).

Table 5-7. Percentage changes in the predicted degree of optical anisotropy (DOA) between two non-sequential loading states for sub-regions of the CT-leaflet insertion (see **Fig. 5-1e**). Values are reported as mean±SEM, and p-values are determined from the one-way ANOVA and multiple comparisons are given in square brackets.

	TVAL Strut CT-Leaflet Insertion (n=8)		MVAL Strut CT-Leaflet Insertion (n=10)	
	Loading Point 0 → Loading Point 5	Loading Point 2 → Loading Point 5	Loading Point 0 → Loading Point 5	Loading Point 2 → Loading Point 5
Sub-region 1	46.3±6.2% [0.015]*	36.0±7.8% [0.233]	25.6±7.6% [0.025]*	28.0±7.1% [0.184]
Sub-region 2	41.2±6.2% [0.006]*	50.1±4.8% [0.053]	37.3±2.6% [1E-7]*	30.0±3.1% [2E-5]*
Sub-region 3	33.0±15.0%	48.5±5.6%	43.1±5.7% [3E-5]*	22.9±11.9% [2E-4]*
Sub-region 4	41.1±6.1% [0.008]*	22.6±4.6% [0.234]	20.7±4.8% [0.119]	23.2±4.0% [0.150]
Sub-region 5	38.3±2.9% [0.008]*	41.8±3.6% [0.087]	31.3±2.3% [5E-8]*	26.7±2.5% [8E-6]*
Sub-region 6	31.8±6.5%	38.2±3.7%	34.6±4.7% [0.008]*	22.0±7.7% [0.023]*
Sub-region 7	25.2±6.0%	17.1±5.9%	14.8±5.7%	12.9±5.6%
Sub-region 8	39.2±3.9% [2E-5]*	41.0±5.1% [6E-4]*	31.3±2.5% [2E-8]*	30.0±3.6% [8E-7]*
Sub-region 9	33.7±6.0% [0.003]*	29.9±7.7% [0.071]	22.3±4.0%	22.1±5.9%

Note: Variations in the number of specimens were due to limitations with the camera field of view not allowing a full visibility of the ROIs within the polarizer lens window. In addition, entries without p-values indicate that multiple comparisons were not performed, as the initial ANOVA was insignificant.

* statistically-significant changes ($p<0.05$).

5.3 Discussion

5.3.1 General Findings and Comparisons with Existing Literature

We found that the stretches of the MVAL and TVAL strut CT were similar under their respective targeted tension (**Fig. 5-5**). Comparing to previous studies on characterizing the

mechanics of chordae tendineae, lower stretches were observed in our study than those reported in the previous testing of individual strut chordae segments [15, 44, 93, 102, 116-118], but the stretches were similar to our previous study on the leaflet-CT-PM entities [113]. In addition, the Ogden constitutive model parameters were determined from nonlinear least-squares fitting to uniaxial mechanical data, and the parameter μ was generally larger for the TVAL strut CT than their MVAL counterparts, while the parameter α was larger for the MVAL strut CT. This suggests that the MVAL strut CT have a lower stress-transition in the low- and high-tension regimes, and that the TVAL strut CT have a higher post-transition stiffness. Additionally, the constitutive model parameters determined in the present study were similar to those reported in our previous study [113], and within a similar range from other mechanical testing studies on individual strut CT segments [15, 93].

From the pSFDI-based collagen microstructural quantifications, we examined the load-dependent changes in the CFAs of both the CT segments and the CT-leaflet insertions. Specifically, collagen fibers of both the CT segments and the CT-leaflet insertions were mostly oriented towards the primary loading direction of 90° (**Figs. 5-6**, **5-7**), with indiscernible changes in the collagen fiber orientations with increased loading (**Tables 5-1**, **5-3**). The minimal changes in θ_{fiber} and the slight deviation of the collagen fibers in the CT segments from the 90° direction may be explained by collagen fiber crimping and uncrimping or by planar waves of collagen fibers as previously described by Millington-Sanders *et al*. (1998) [37]. Interestingly, we did notice changes in θ_{fiber} when the CT-leaflet insertion was divided into nine sub-regions; however, there was no clear and consistent trend in the collagen fiber reorientations within the CT-leaflet insertions.

In addition, we observed increases in the quantified DOA with the applied loading, indicating a better alignment of the collagen fibers from the unloaded to the loaded states (**Tables 5-1**, **5-2**, **5-3**, **5-4**). Generally, the greatest increase in the quantified DOA was from Loading Points 4 and 5 (i.e., $0.3F_{max}$ vs. F_{max}) for both the CT segments and the CT-leaflet insertions, suggesting more rapid alignments of the collagen fibers in the high-tension than in the low-tension regime. Comparing the tissue mounting and post-preconditioning configurations to the peak loading, the DOA increased up to 50%. Those increases in the DOA without major collagen fiber reorientations may be explained by the uncrimping of collagen fibers in response to the increased loads. This findings agree with the observations in our previous study on testing the central, belly region of the MVAL tissue under equibiaxial loading [103]. In that study, the collagen fiber orientations of the tissue mostly remained the same between the unloaded and loaded states, whereas clear increases in the DOA were found.

Furthermore, previous studies are limited when compared to our collagen microstructural quantification results. In particular, no study has yet quantified the load-dependent behaviors of the collagen fibers in the strut CT-leaflet insertion for the AHVs. Padala *et al.* (2010) investigated the mechanical behaviors of the MVAL strut CT-leaflet insertion by using an *in vitro* flow loop together with optical marker tracking of the CT-leaflet insertion to obtain surface strains [43]. They found that the edges of the CT-leaflet insertion stretched more than the central portions. To complement their findings of the regional variations in the tissue extensibility, we observed some greater increases in DOA in central portions of the CT-leaflet insertion, as well as the increases in some of the edge regions (**Fig. 5-8** and **Table 5-7**). Padala *et al.* (2010) also analyzed the CT-leaflet insertion using small angle light scattering and noted a higher alignment of collagen fibers in the CT segment, and that the collagen fibers transitioned into a more disorganized network in

the leaflet insertion [43]. In another previous study using light microscopy, Chen *et al.* (2004) found similar orientations of collagen fibers in the MVAL strut CT-leaflet insertion to those reported by Padala *et al.* (2010); however, Chen *et al.* (2004) also noticed the circumferentially-oriented collagen fibers in the leaflet tissue closer to the annulus [40, 43]. In our study, we noticed some higher DOA values in the CT segments than the CT-leaflet insertions, but the differences in the predicted θ_{fiber} were not noticeable (**Figs. 5-6**, **5-7** and **Tables 5-1**, **5-3**). The difference in the findings between our present study and the two previous studies may be attributed to the amount of leaflet tissue preserved beyond the CT-leaflet insertion, i.e., from the belly region of the leaflet up to the annulus.

5.3.2 Study Limitations and Future Extensions

There are a few limitations existent in this study. First, the integrated pSFDI-biaxial testing system had a limited field of view of the camera that did not allow for imaging of the entire CT-leaflet insertion for some tissues specimens, resulting in a slightly reduced sample size for the CT segments or the CT-leaflet insertions. Second, there were some small mispredictions in the collagen fiber orientations (**Figs. 5-6**, **5-7**), which may be due to the birefringent response of the collagen fibers, or tissue surface imperfections such as tissue folding. In our work, tissues were mounted to the system with care to ensure that minimal surface imperfections were present to limit the potential for mispredictions of θ_{fiber}. Third, the physical interpretation of the quantified DOA is not yet fully established as to how it is related to the degree of collagen fiber alignment. The DOA is a function of the optical anisotropy, as opposed to structural anisotropy-based metrics such as the normalized orientation index (NOI) described in previous works [35, 119].

Future extensions of the present work include the analysis of the leaflet deformations, increasing the polarizer field of view, assessing the CT failure mechanics, and testing other CT

subsets (i.e., the marginal and basal CT). To elaborate, in our study we did not provide a detailed strain mapping for the leaflet-insertion, such as performed with the optical marker approach used by Padala *et al.* (2010), and thus, it would be a useful extension to further enhance our findings [43]. In addition, the pSFDI-modality could be useful in connecting the CT failure mechanics to the underlying microstructural changes. Use of the leaflet-CT-PM entity method performed in this work would be a good supplement to the solely mechanics-based findings from the previous investigation of CT failure [106].

5.4 Concluding Remarks

In this study, *for the first time*, we have quantified the load-dependent changes in the collagen fiber architecture of the strut CT-leaflet insertions of the AHV anterior leaflets by using the integrated pSFDI-uniaxial testing and the leaflet-CT-PM entity approach. The pSFDI-based collagen microstructural quantifications in our study for both the CT segments and the CT-leaflet insertions could serve useful for understanding the recruitment of collagen fibers by emulating physiological loading conditions. Moreover, we have also provided information on the stress-stretch behaviors of the CT segments through the tine-based, cyclic uniaxial testing, which allowed for predictions of the Ogden-type constitutive model parameters. Results from this study will be beneficial in developing a better understanding of the tissue mechanics-microstructure relationships of the AHVs – a field of increasing interest in the biomechanics community, such as in growth and remodeling frameworks [120, 121]. Furthermore, the information from this study could be useful as a first look into better understanding of chordae rupture, based on the quantified DOA of the CT-leaflet insertions, or for incorporating the collagen fiber kinematics into the AHV computational models.

CHAPTER 6 – CONCLUSIONS AND FUTURE WORK

6.1 Conclusions

The results presented in this thesis further our fundamental knowledge of AHV biomechanics, specifically for the leaflets and the chordae tendineae, which will lead to the future development and refinement of AHV computational models, and consequently improve patient outcome. The AHV anterior leaflets have been characterized with regards to the spatial mechanical heterogeneity, the individual layer mechanics, and the contributions of the GAGs to the mechanical behavior of the AHV leaflets. Furthermore, the chordae tendineae have been characterized using a unique method that better preserves the *in vivo* interactions, resulting in different uniaxial tensile characteristics compared to those reported in the previous studies. Finally, the complex load-dependent changes in the collagen fiber architecture of the chordae-leaflet insertion has been, *for the first time*, analyzed using pSFDI. The key research developments of each study are summarized as follows.

(1) *Mechanical Characterizations of the AHV Leaflet Tissues*

Through the studies on characterizing the stress-stretch and stress-relaxation behaviors of the atrioventricular heart valve leaflets, richer information about the tissue biomechanics has been obtained. Specifically, we have noted that the leaflets exhibited spatially varying mechanics, with a significant difference in the material anisotropy when comparing the central tissue regions to the edge regions. Variance has been observed in the peak mechanical stretch across the six tissue regions, with the greater extensibility observed close to the annulus of the MVAL. Further, we have also quantified the mechanical properties of individual tissue layers of both the MVAL and the TVAL. The elastin-rich

atrialis/spongiosa layer has been shown to be the most compliant and anisotropic examined layer. Accordingly, the fibrosa and ventricularis layers has been found to have a smaller toe region and a nearly-isotropic behavior. Additionally, we have quantified the effects of the glycosaminoglycans in overall leaflet mechanical function. Specifically, it has been found that the GAGs play a notable role in the mechanical characteristics of both the MVAL and the TVAL: (i) under biaxial mechanical testing, tissues with GAGs removed had the greater extensibility, and (ii) under stress relaxation testing, tissues with GAGs removed had a reduced stress decay behavior. Information from these studies will be critical for refining existing microstructure-based constitutive models [34, 62, 69, 79-87], or a growth and remodeling framework for soft tissues [88, 89]. These models could then be employed for predictive simulations of the AHV function and to inform improved valve replacement therapeutics.

(2) *Mechanics of Leaflet-CT-Papillary Muscle Entities*

The stress-stretch responses of the AHV's chordae tendineae have been analyzed as a tissue entity by preserving the papillary muscles and leaflet for considering the mechanical interactions between the CT and the leaflet and the PMs. We have observed that the quantified tissue stretches were not uniformly distributed across the CT, and that the chordae stretches were different as compared to previous literature. Findings of this study suggest that preservation of the papillary muscles and leaflet attachments could have a direct impact on the observed mechanical properties of the strut chordae tendineae. The results of this work could be useful for the refinement of valvular disease therapeutics. For example, the CT replacement ePTFE sutures could be constructed to better handle the physiological environment, remedying the issues of excessive elongation or rupture.

(3) *Load-Dependent Collagen Fiber Architecture of the Chordae-Leaflet Insertion*

The load-dependent changes in the CFA of the CT-leaflet insertion have been quantified *for the first time* using the integrated pSFDI-uniaxial testing approach. We found that collagen fibers in the CT-leaflet insertion and in the CT segment became significantly more aligned with increased loading, as quantified through the DOA. Further, the collagen fiber kinematics derived in this study are more representative, as the pSFDI method does not require tissue fixation. The information obtained in this study is especially useful for better understanding collagen fiber recruitments under the physiologically emulating conditions, expanding the knowledge in AHV biomechanics research. Future impacts of the work include incorporating the collagen fiber kinematics information to microstructurally informed computational models, which can be especially helpful in understanding the tissue growth and remodeling.

6.2 Recommendations for Future Research

This thesis is concluded with recommendations for future work.

(1) *More Extensive Testing of Valvular Tissues*

While we have provided detailed information on the complex mechanics of the valve leaflets, we only investigated the anterior leaflets. Regional, layer-based, and GAG-contribution investigations into the other untested leaflets will provide researchers with richer information regarding regional variance, and microstructure-mechanics relationships for all five AHV leaflets. Other useful studies for understanding the GAG contributions would involve a treatment of the tissues until the complete removal of the GAGs. Future studies could also be warranted to investigate the effect of GAG removal on

collagen fiber recruitment using the dynamic collagen microstructure imaging technique [35]. Finally, testing of human AHV tissues would be useful to corroborate the findings from the porcine valve structures.

(2) *Testing of All Chordae Tendineae Subsets*

The leaflet-CT-PM entity testing procedure developed in this thesis could be extended to analyze the previously-categorized CT of each AHV not yet considered in this study (e.g., the basal and marginal CT) [95, 122]. Another future extension includes further analyses of the strains of both the leaflet and the PMs during the uniaxial testing of the CT tissue entity, as a limited number of samples were used in the presented work. Additionally, the testing method could also be used to study human leaflet-CT-PM entities.

(3) *Development and Refinement of AHV Computational Models*

Integration of spatially varied leaflet mechanical properties, individual layer contributions, microstructural contributions to the leaflet behaviors, collagen fiber reorientations, and chordae mechanics into the constitutive model development will facilitate more accurate representation of the heart valve function than those existing models based on mechanical data of bulk leaflet tissues or individual chordae segments. AHV computational models utilizing such more realistic tissue mechanics could provide insights into regionally-dependent treatments for valvular disease, such as suture-based valvuloplasty or annuloplasty surgical repair [123, 124]. Further, these computational models could be useful in evaluating the effectiveness of tissue-engineered valves.

APPENDIX A – NOMENCLATURE

Table A-1. Description of the abbreviations used throughout the thesis.

Category	Abbreviation	Description
Anatomy	AHV	Atrioventricular heart valve
	CT	Chordae tendineae
	ECM	Extracellular matrix
	LG	Left group (chordae)
	MV	Mitral valve
	MVAL	Mitral valve anterior leaflet
	MVPL	Mitral valve posterior leaflet
	PM	Papillary muscle
	RG	Right group (chordae)
	TV	Tricuspid valve
	TVAL	Tricuspid valve anterior leaflet
	TVPL	Tricuspid valve posterior leaflet
	TVSL	Tricuspid valve septal leaflet
	AI	Anisotropy index
	D	Chordae thickness
	circ	Circumferential direction
	-C	Control specimen
	rad	Radial direction
	t	Specimen thickness (leaflet)
	-T	Treated specimen
Microstructure	A	Atrialis
	F	Fibrosa
	GAG	Glycosaminoglycan
	PG	Proteoglycan
	S	Spongiosa
	V	Ventricularis
	VIC	Valvular interstitial cell
Mechanics	**C**	Right Cauchy-Green deformation tensor
	E	Green-Lagrange strain tensor
	F	Deformation gradient tensor
	I	Identity tensor
	J	Jacobian of the Deformation Gradient **F**
	λ	Tissue stretch
	$\lambda^{1\text{-}2}$	Mechanical stretch (stretch)
	$\lambda^{0\text{-}2}$	Peak stretch
	$\lambda^{0\text{-}1}$	Preconditioning stretch
	P	First-Piola Kirchhoff stress tensor

	S	Second-Piola Kirchhoff stress tensor
	σ	Cauchy stress tensor
	T	Membrane tension
	T_{circ}	Membrane tension in the circumferential direction
	$T_{circ,max}$	Maximum membrane tension in the circumferential direction
	T_{rad}	Membrane tension in the radial direction
	$T_{rad.max}$	Maximum membrane tension in the radial direction
Imaging	DOA	Degree of optical anisotropy
	pSFDI	polarized spatial frequency domain imaging
Miscellaneous	2D	Two-dimensional
	3D	Three-dimensional
	ANOVA	Analysis of variance
	CCD	Charge-coupled device
	DIC	Digital image correlation
	ePTFE	Expanded polytetrafluoroethylene
	FDA	Food and Drug Administration
	NIH	National Institutes of Health
	NRMSD	Normalized root mean square deviation
	N.S.	Not significant (statistics)
	PBS	Phosphate-buffered saline
	SD	Standard deviation
	SEM	Standard error of the mean
	USDA	United States Department of Agriculture

APPENDIX B – DETAILED BIAXIAL MECHANICAL TESTING PROCEDURES FOR VALVE LEAFLETS

In Appendix B, the detailed procedures for the biaxial mechanical testing of the AHV leaflets are described. The procedures are excerpted from a previous journal publication from our lab [16].

1. Tissue Acquisition and Cleaning

1.1) Retrieve the animal hearts on the same day as the animal is slaughtered and store the hearts in an ice chest to ensure the tissue freshness. Transport the hearts to the laboratory space.

1.2) Upon arrival to the lab, submerge the heart in the bucket of phosphate-buffered saline (PBS) solution to rinse off any excess blood. Retrieve forceps, a placemat, a surgical blade, a bucket of PBS solution, bleach and a plastic bag. Prepare the placemat by laying it on the dissection counter, allowing for easier cleanup of blood-related mess. After the heart has been sufficiently rinsed, place the heart on the placemat (**Fig. B-1a**).

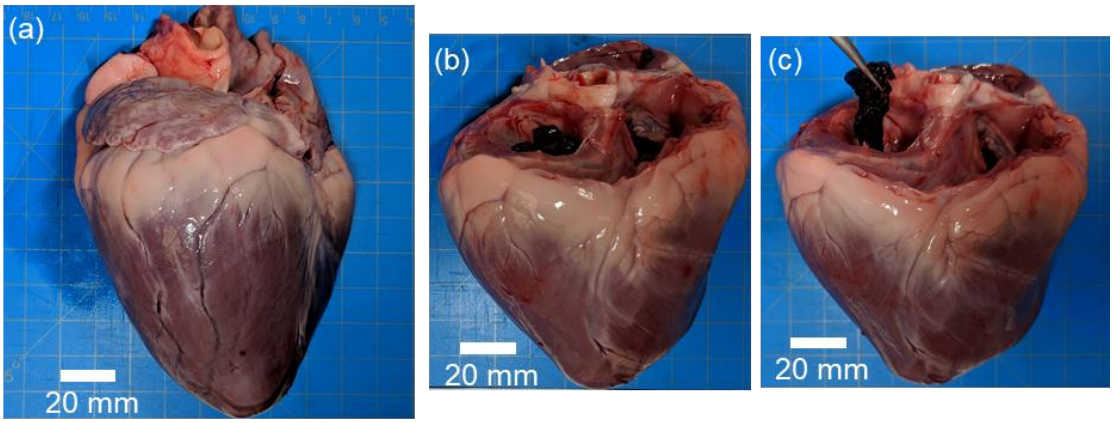

Figure B-1. Experimental photos of porcine hearts retrieved from a local slaughterhouse: (a) whole heart is rinsed of blood with PBS, (b) a cut is made between the atria and ventricle to reveal both the MV and the TV, and (c) blood clots are removed from the heart before storage.

1.3) Using the forceps, locate the parting line between the atria and the ventricle on each side of the heart. Using a razor blade, make an incision carefully along this parting line and reveal the heart valves and the ventricles (**Fig. B-1b**). Make the incision along the entire outer circumference of the heart, such that the atria and all heart material superior to the ventricles may be removed.

1.4) With the forceps, carefully pull out any observed blood clots in the ventricles (**Fig. B-1c**). If an attempt is made to remove a blood clot but it does not move, ensure chordae tendineae or leaflets have not been grabbed. Place blood clots in the biohazard bag for waste disposal.

1.5) When all blood clots have been removed from the ventricles, rinse the heart one final time in the bucket of PBS solution. Place the clean heart in the plastic bag and store it in a freezer.

1.6) Using a solution of 10% bleach and 90% water, mix the blood with the bleach solution and stir continuously for about 10 minutes. Successful bleach treatment is indicated by the solution transitioning from red to yellow. Dispose the bleach-treated blood through drainage.

CAUTION: Bleach is a toxic substance and can be harmful if ingested.

2. Heart Dissection and Examination of Anatomy

2.1) Retrieve the previously cleaned heart and allow it to thaw in a warm water bath. The required materials for dissection include forceps, surgical blades, placemats, phosphate-buffered saline, and small storage containers. After the heart is completely thawed, put it on a placemat to absorb remaining blood.

2.2) Hold the heart for a top-down (superior) view to optimally observe the valve structures. Beginning with the MV on the left side of the heart, use forceps to carefully manipulate the leaflets and identify a commissure, or parting line, between the leaflets.

2.3) Make an incision along the commissure and carefully cut through the ventricular wall, being sure not to damage the leaflets. It may be necessary to cut chordal attachments during this process to fully open the ventricle. Once the incision is made, open the ventricle (**Fig. B-2a**).

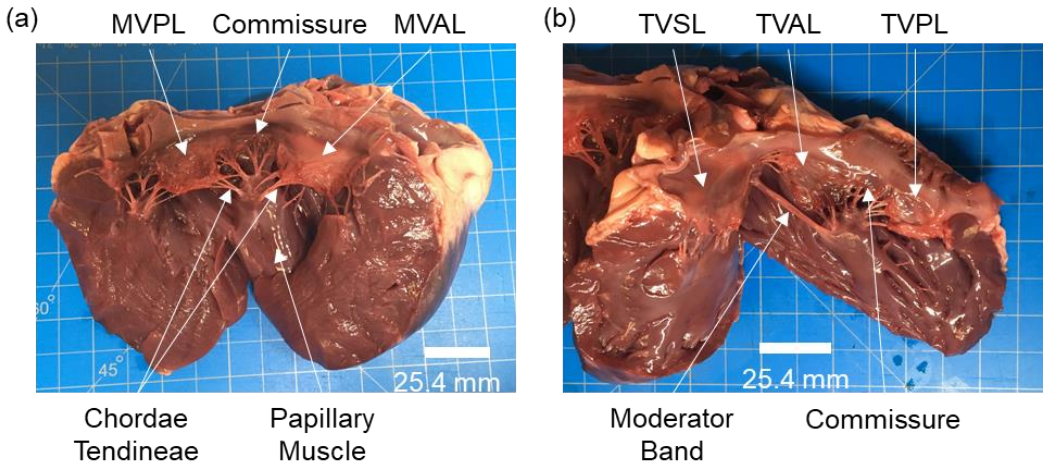

Figure B-2. Experimental photos of the opened porcine heart, showing the five AHV leaflets and other sub-valvular components: (a) the MV with dissection of the left heart along the commissure between the two leaflets , and (b) the TV with similar dissection on the right heart.

2.4) Identify the MV anterior and posterior leaflets and use a surgical blade to sever the chordal attachments to the papillary muscles. Using forceps, stretch the leaflets taut and make cuts to separate the leaflets from the annulus. Place excised leaflets in an appropriately labeled container filled with PBS solution and store in a refrigerator at approximately 4 °C.

2.5) Hold the heart in the top-down view and identify the TV on the right side of the heart. Locate the commissures and make an incision through one of the commissures and the ventricular wall (**Fig. B-2b**).

2.6) Identify the TV septal, posterior, and anterior leaflets, and perform the leaflet extraction as done in Step 2.4. Place all obtained leaflets in a labeled container filled with PBS solution and store the container in a refrigerator at approximately 4 °C.

3. Tissue Dissection

3.1) Retrieve the leaflet from the fridge, the tissue cutter for the specified sectioning size, surgical pen, forceps, razor blades, and a cutting mat.

3.2) Using forceps, remove the specimen from the PBS and lay it flat on the cutting mat with radial direction (Rad.) aligned to the *Y*-direction, and the circumferential direction (Circ.) aligned to the *X*-direction (**Fig. B-3a**). Identify the leaflet's *central region* as the testing section.

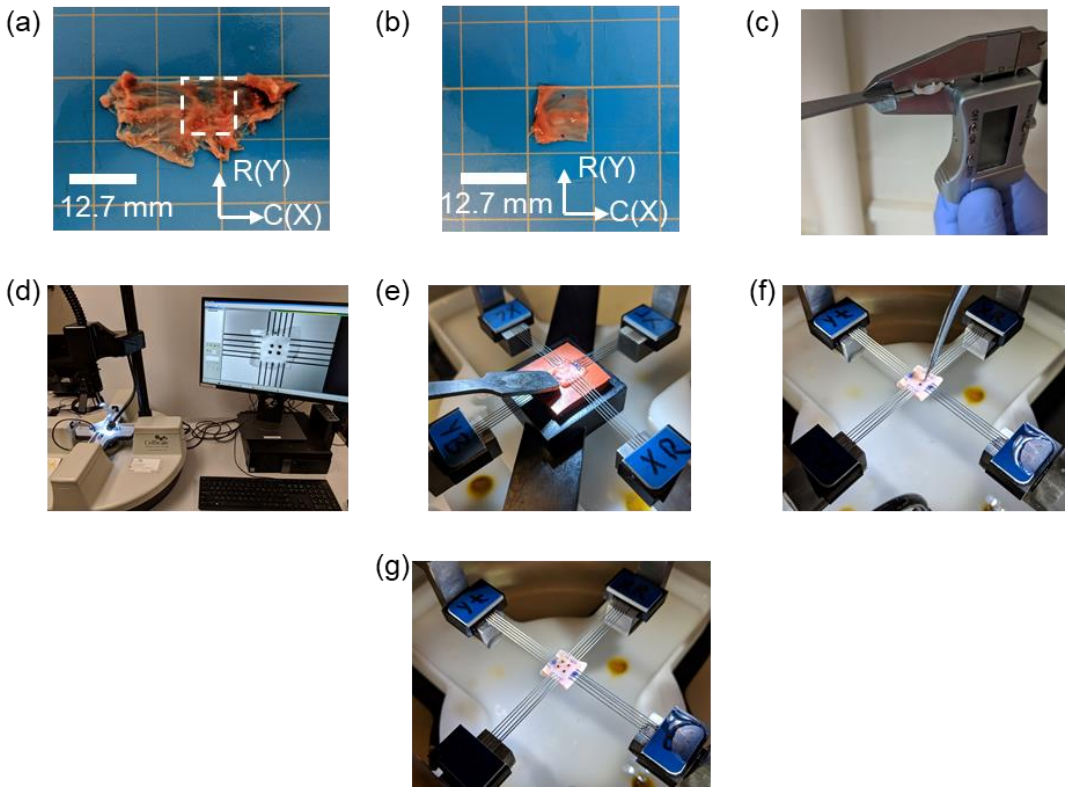

Figure B-3. Photos of the excised leaflet being prepared for biaxial mechanical testing: Heart valve leaflet testing requires the (a) bulk leaflet be sectioned into a (b) 10mm x 10mm testing region (radial direction noted by surgical pen markers). (c) The leaflet thickness is measured. Specimens are mounted to (d) the biaxial testing system by (e) piercing the tissue with metal tines. After mounting, (f) fiducial markers are glued onto the surface of the tissue before (g) submersion in PBS solution at 37 °C.

3.3) Align the tissue cutter such that the desired tissue testing region is within the boundaries of the razor blades. Make one cut horizontally and another vertically to form a square region of desired dimension (**Fig. B-3b**). Using the surgical pen, label the tissue's radial direction (**Fig. B-3b**).

3.4) Using the razor blade, trim chordal attachments by stretching the chordae from the leaflet with the forceps and making a careful cut without causing damage to the leaflet.

Note: The protocol can be paused here. If the protocol is paused, store the sectioned tissue in a labeled container filled with PBS solution, and store the container in a refrigerator at approximately 4 °C (as explained in Step 2.6). However, tissue testing should occur within two days of dissection.

4. Thickness Measurement and Biaxial Tester Setup

4.1) Retrieve the sectioned tissue specimen, digital calipers, and a small metal spatula. Using the digital calipers, measure and record the thickness of the metal spatula.

4.2) Using forceps, lay the tissue specimen flat on the metal spatula. Using a digital caliper measure the thickness of the spatula-tissue pair (**Fig. B-3c**) at three different leaflet locations. Subtract the spatula's thickness from the pair and record the average thickness.

4.3) Prepare a PBS bath at 37 °C, which is correspondent to the tissue's physiologic conditions.

5. Tissue Mounting and Fiducial Marker Placement

5.1) Retrieve forceps, tissue specimen, mounting hardware, fine-tipped tool, glass beads (diameters of 300-500 μm), and super glue.

5.2) Mount the tissue to the biaxial testing system (**Fig. B-3d** and **Fig. B-3e**). While mounting, ensure the tissue's circumferential and radial directions are aligned with the machine's *X*- and *Y*-directions, respectively.

5.3) For fiducial marker placement, place glass beads into one small open-faced container and a small pool of super glue in another container. Using the fine-tipped tool, coat the tip with a small amount of super glue and stick an individual bead to the tip of the tool.

5.4) Carefully use the tool to transfer the bead to one corner of the middle third of the tissue's testing region (**Fig. B-3f**). Repeat this step until a square array of four beads is formed (**Fig. B-3g**).

NOTE: It is crucial that excess glue be avoided, and that fiducial markers do not stick together as later data image correlation (DIC) techniques will produce useless tracking results. It is important that the square array must be within the middle third of the tissue's testing region.

6. Preconditioning Step and Duration Timing

6.1) To compute the appropriate membrane tension, obtain the tissue's effective testing edge length and use the equation:

$$T = diag[T_C, T_R] = diag[f_C, f_R] / L \tag{B.1}$$

Herein, T is the membrane tension in a unit of force/length, f is the force, and L is the specimen's effective testing length.

6.2) Create a preconditioning protocol such that the tissue will undergo ten loading/unloading cycles at the forces associated with peak membrane tension at a loading rate of 4.42 N/min, including a preload of 2.5% of the maximum force (**Fig. B-4**).

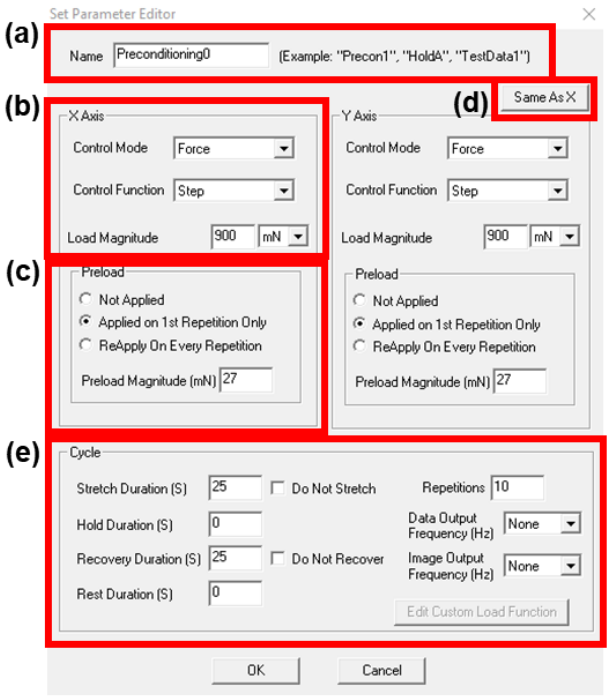

Figure B-4. Example protocol parameters for the preconditioning testing of an MVAL with a 7.5x 7.5mm testing region: The preconditioning protocol is created by setting (a) the protocol name, (b) the testing control mode and force in the *X*-axis, (c) the preload conditions, (d) the *Y*-axis parameters to be the same as in the *X*-axis, and (e) the cycle parameters.

6.2.1) Create a new arbitrary testing directory to temporarily to store the preconditioning data because it is not necessary for future calculations. Establish a loading rate of 4.42 N/min for subsequent testing.

6.2.2) Create a new set of testing parameters and set the name of the protocol as Preconditioning0 (**Fig. B-4a**). For the *X*- and *Y*-axes, set the control mode to be force and the control function to be step. Set the load magnitude as the force associated with targeted peak membrane tension (see Step 6.1, **Fig. B-4b**). Set the preload magnitude as 2.5% of the maximum force for the first repetition only (**Fig. B-4c**). Set the stretch duration and recovery duration to both be 25 seconds. Set the number of repetitions to be 10 (**Fig. B-4e**).

6.3) When the preconditioning step finishes, make a note of the tissue's deformation in the *X*- and *Y*-directions. Prepare a protocol to move the specimen to the maximum force beginning from the recorded size.

6.3.1) Retrieve a stopwatch for timing purposes. Begin the maximum force loading protocol and start the stopwatch simultaneously when the machine begins actuation (**Fig. B-5a**). Stop the stopwatch when actuation stops. Stopping will be obvious through auditory cues.

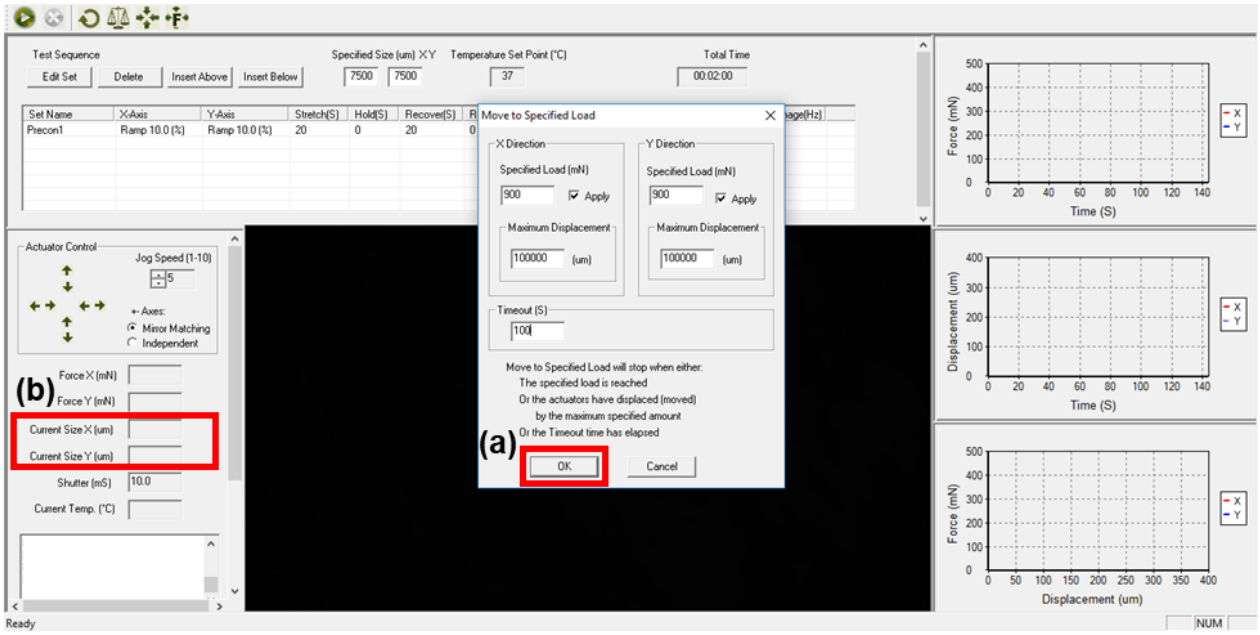

Figure B-5. Example protocol parameters for the timing step for an MVAL with a 7.5x7.5mm testing region: The timing step requires (a) moving the tissue from the post preconditioning deformation to the peak membrane tension (and corresponding peak deformation) while simultaneously starting a stopwatch to record the stretch time. When the target force has been reached, (b) the post-preconditioning deformation is recorded.

6.3.2) Record the post preconditioning peak tissue deformation, alongside the time from the stopwatch representing the tissue's optimal stretch time (**Fig. B-5b**).

7. Biaxial Mechanical Testing

7.1) Prepare a force-controlled protocol at a loading rate of 4.42 N/min:

7.1.1) Open a new testing directory and name the test. Set the data to save to a known location for use in later stress and strain calculations. Move the specimen back to the original mounting configuration.

7.1.2) Create a protocol set titled “FirstImage”. Set the *X*-axis and *Y*-axis control mode to force and the control function to step. Set the load magnitude to 0 mN. Set the stretch duration and recovery duration each to 1 second. Set the number of repetitions to 1. Set the data output frequency and image output frequency each to 1 Hz

7.1.3) Construct a new testing set named “PreconditioningA”. Establish the testing parameters such that the tissue will undergo 10 repetitions of cyclic loading/unloading to the targeted force for desired membrane tension exactly as was prepared in Step 6.2. Note that now, the stretch time and recover time should be the time recorded in Step 6.4. No images are captured in the “A” testing set, but data is captured at 15 Hz.

7.1.4) Construct another testing set named “PreconditioningB”. All testing parameters should be identical to as found in the previous step, with the exception that image output frequency is set to 15Hz, and no preload is applied.

7.1.5) After the preconditioning protocol, create testing protocols such that the tissue is loaded to peak membrane tension in the following circumferential-to-radial loading ratios at a loading rate of 4.42 N/min: 1:1, 0.75:1, 1:0.75, 0.5:1, 1:0.5 (**Fig. B-6**). Retrieve data from the last

two cycles of each loading ratio for subsequent data processing and analyses described in Step 10. Refer to **Table B-1** for a detailed description of the protocols to be established.

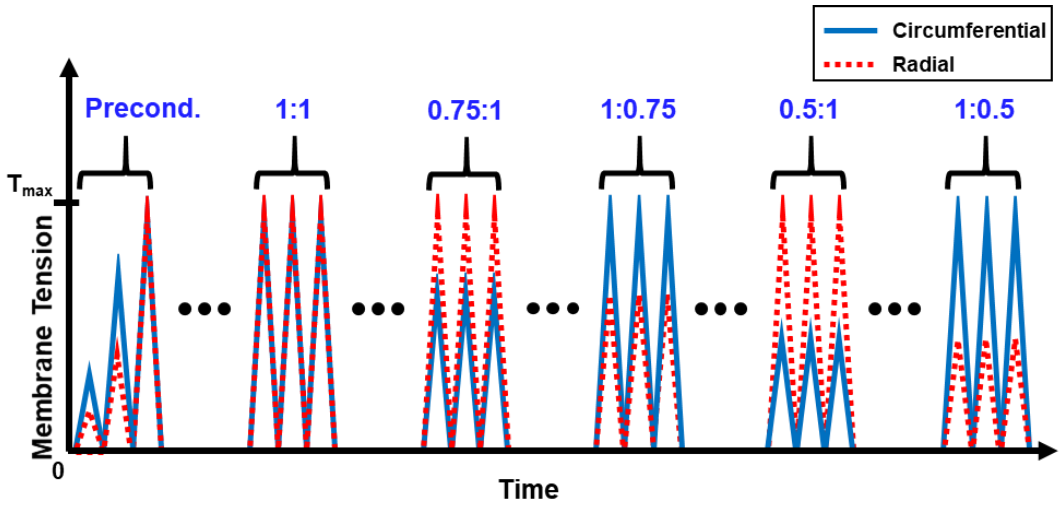

Figure B-6. Schematic of the force-controlled biaxial testing procedure for testing mitral and tricuspid valve leaflets: The testing protocol consists of an equibiaxial loading preconditioning step to exercise the tissue to its in vivo state, followed by various loading ratios of the peak membrane tension in each tissue direction (T_x:T_y): 1:1, 0.75:1, 1:0.75, 0.5:1, and 1:0.5. Each subsection of the force-controlled testing protocol is performed for 10 loading/unloading cycles.

Table B-1. Full testing parameters for all protocols of the force-controlled testing scheme: Testing parameters for the force-controlled testing scheme. Forces (in millinewtons) are written as F to represent the force associated with targeted peak membrane tension. Stretch time is written as t to represent the stretch time (in seconds) specific to the tissue being tested.

Set Name	*X*-Axis	*Y*-Axis	Stretch (S)	Hold (S)	Recover (S)	Rest (S)	XPreload (mN)	YPreload (mN)	Reps	Data (Hz)	Image (Hz)
FirstImage	Step 0.0 (mN)	Step 0.0 (mN)	1	0	1	0	0.0 (First)	0.0 (First)	1	1	1
PreconditioningA	Step *F* (mN)	Step *F* (mN)	*t*	0	*t*	0	0.025**F* (First)	0.025**F* (First)	8	15	0
PreconditioningB	Step *F* (mN)	Step *F* (mN)	*t*	0	*t*	0	None	None	2	15	15
1:1A	Step *F* (mN)	Step *F* (mN)	*t*	0	*t*	0	None	None	10	15	0
1:1B	Step *F* (mN)	Step *F* (mN)	*t*	0	*t*	0	None	None	2	15	15
0.75:1A	Step (0.75**F*) (mN)	Step *F* (mN)	*t*	0	*t*	0	None	None	10	15	0
0.75:1B	Step (0.75**F*) (mN)	Step *F* (mN)	*t*	0	*t*	0	None	None	2	15	15
1:0.75A	Step *F* (mN)	Step (0.75**F*) (mN)	*t*	0	*t*	0	None	None	10	15	0
1:0.75B	Step *F* (mN)	Step (0.75**F*) (mN)	*t*	0	*t*	0	None	None	2	15	15
0.5:1A	Step (0.5**F*) (mN)	Step *F* (mN)	*t*	0	*t*	0	None	None	10	15	0
0.5:1B	Step (0.5**F*) (mN)	Step *F* (mN)	*t*	0	*t*	0	None	None	2	15	15
1:0.5A	Step *F* (mN)	Step (0.5**F*) (mN)	*t*	0	*t*	0	None	None	10	15	0
1:0.5B	Step *F* (mN)	Step (0.5**F*) (mN)	*t*	0	*t*	0	None	None	2	15	15

7.2) Prepare a displacement-controlled testing protocol at a loading rate of 4.42 N/min:

7.2.1) Biaxial stretching in the *X*-direction and *Y*-direction to the displacements associated with the peak circumferential and radial stretches, respectively (**Fig. B-7a**).

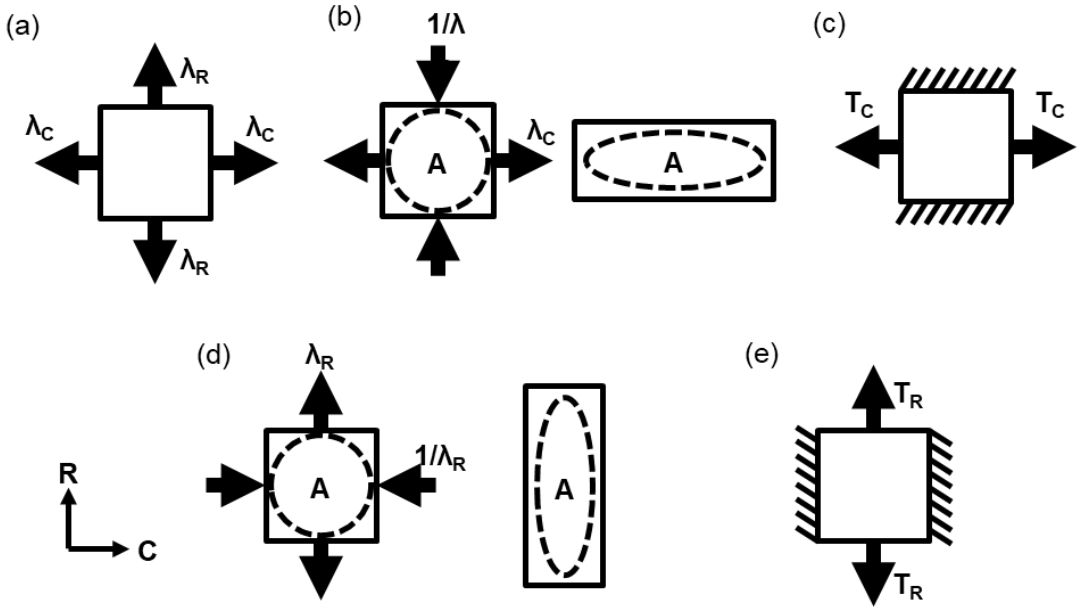

Figure B-7. Schematic of displacement-controlled biaxial testing procedure for testing mitral and tricuspid valve leaflets: The testing protocol consists of an (a) biaxial displacements associated with the peak membrane tensions, (b) pure shear in the *X*-direction, (c) constrained uniaxial displacement in the *X*-direction, (d) pure shear in the *Y*-direction, and (e) constrained uniaxial displacement in the *Y*-direction. Each subsection of the displacement-controlled testing protocol is performed for 10 loading/unloading cycles.

7.2.2) Pure shear along the *X*-direction — stretching in the *X*-direction associated with the peak circumferential stretch and shortening in the *Y*-direction, *while keeping the dashed area constant under deformation* (**Fig. B-7b**).

7.2.3) Constrained uniaxial stretching along the *X*-direction (**Fig. B-7c**).

7.2.4) Pure shear along the *Y*-direction (**Fig. B-7d**).

7.2.5) Constrained uniaxial stretching along the *Y*-direction (**Fig. B-7e**).

7.2.6) Between each of these steps, construct a rest "cycle" of one minute that holds the tissue at the original mounted configuration. Retrieve data from the last two cycles of each loading ratio for data processing and analyses (Step 9). Refer to **Table B-2** for a detailed description of the protocols to be established.

7.3) Prepare a stress-relaxation protocol such that the tissue is loaded in each direction, at a loading rate of 4.42 N/min, to the displacements associated with the peak membrane tensions (Step 7.2) and held at that displacement for 15 minutes (**Fig. B-8** and **Fig. B-9**). After 15 minutes the protocol should be set to recover the tissue to its original mounting configuration.

NOTE: In the case of tissue tearing, abort the test immediately to prevent any potential damage caused to the biaxial testing system.

Table B-2. Displacements (in percentages) are written as *dx* and *dy* to represent the peak post-preconditioning percent elongation in the *X*- and *Y*-directions, respectively. Stretch time is written as *t* to represent the stretch time (in seconds) specific to the tissue. Abbreviations are: PS, pure shear; CU, constrained uniaxial.

Set Name	X-Axis	Y-Axis	Stretch (S)	Hold (S)	Recover (S)	Rest (S)	XPreload (mN)	YPreload (mN)	Reps	Data (Hz)	Image (Hz)
FirstImage	Step 0.0 (mN)	Step 0.0 (mN)	1	0	1	0	0.0 (First)	0.0 (First)	1	1	1
1:1A	Ramp d_x (%)	Ramp d_y (%)	*t*	0	*t*	0	0.025**F* (First)	0.025**F* (First)	10	15	0
1:1B	Ramp d_x (%)	Ramp d_y (%)	*t*	0	*t*	0	None	None	2	15	15
Rest	Ramp 0.0 (%)	Ramp 0.0 (%)	0	0	0	60	None	None	1	15	0
PSXA	Ramp d_x (%)	Ramp $1/d_y$ (%)	*t*	0	*t*	0	None	None	10	15	0
PSXB	Ramp d_x (%)	Ramp $1/d_y$ (%)	*t*	0	*t*	0	None	None	2	15	15
Rest	Ramp 0.0 (%)	Ramp 0.0 (%)	0	0	0	60	None	None	1	15	0
PSYA	Ramp $1/d_x$ (%)	Ramp d_y (%)	*t*	0	*t*	0	None	None	10	15	0
PSYB	Ramp $1/d_x$ (%)	Ramp d_y (%)	*t*	0	*t*	0	None	None	2	15	15
Rest	Ramp 0.0 (%)	Ramp 0.0 (%)	0	0	0	60	None	None	1	15	0
CUXA	Ramp d_x (%)	Ramp 0.0 (%)	*t*	0	*t*	0	None	None	10	15	0
CUXB	Ramp d_x (%)	Ramp 0.0 (%)	*t*	0	*t*	0	None	None	2	15	15
Rest	Ramp 0.0 (%)	Ramp 0.0 (%)	0	0	0	60	None	None	1	15	0
CUYA	Ramp 0.0 (%)	Ramp d_y (%)	*t*	0	*t*	0	None	None	10	15	0
CUYB	Ramp 0.0 (%)	Ramp d_y (%)	*t*	0	*t*	0	None	None	2	15	15

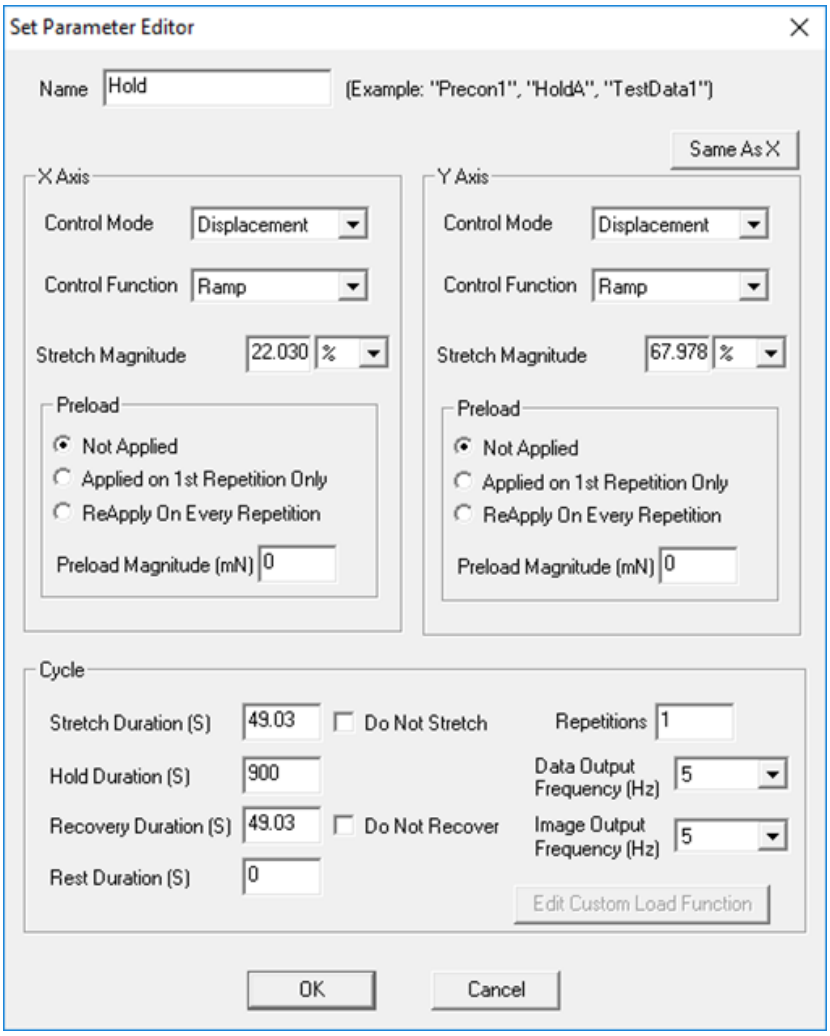

Figure B-8. Example stress-relaxation testing parameters for a mitral valve anterior leaflet with effective testing region of 7.5x7.5mm: Testing set parameters for stress-relaxation testing for a mitral valve anterior leaflet where targeted displacement is the peak tissue deformation specific to this tissue.

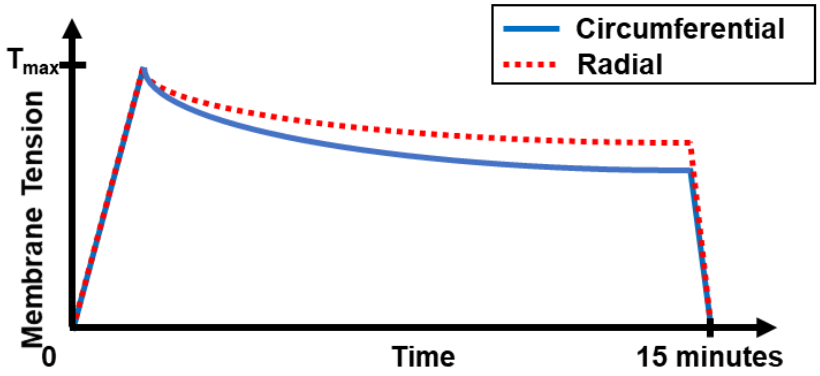

Figure B-9. Schematic of the 15-minute stress-relaxation testing procedure for testing mitral and tricuspid valve leaflets: The testing protocol involves holding biaxial displacements associated with the peak membrane tensions for 15 minutes, after which the tissue is returned to the mounting configuration.

8. Tissue Fixation for Histology Analysis

8.1) Unmount the tissue from the biaxial testing system. Place the tissue into a container filled with 10% formalin, and then place the container in a refrigerated environment at approximately 4 °C. Let the tissue be fixed for 24-48 hours, depending on the tissue's thickness.

CAUTION: Formalin is a known carcinogen and if breathed in excess may cause lungs to become fixed. All work with formalin should be performed in a fume hood with adequate ventilation.

8.2) After the tissue has been fixed in formalin for 24-48 hours, transfer the tissue to an 80% ethanol solution for later histology. The tissue should be stored in solution in a refrigerated environment at 4 °C.

Note: The protocol can be paused here. Once tissues are fixed, specimens can be analyzed at any time. If the protocol is paused, store the tissue in a labeled container filled with 80% ethanol, and store the container in a refrigerator at approximately 4 °C (as explained in Step 8.2).

8.3) Prepare the tissue for commercial histology analysis as per the vendor's instructions. If a certain leaflet constituent, such as collagen, elastin, glycosaminoglycans, etc., is of the study's interest, ensure that the appropriate histology stain is employed.

*NOTE: Histology slides may be visualized using a microscope to observe desired constituents (**Fig. B-10**).*

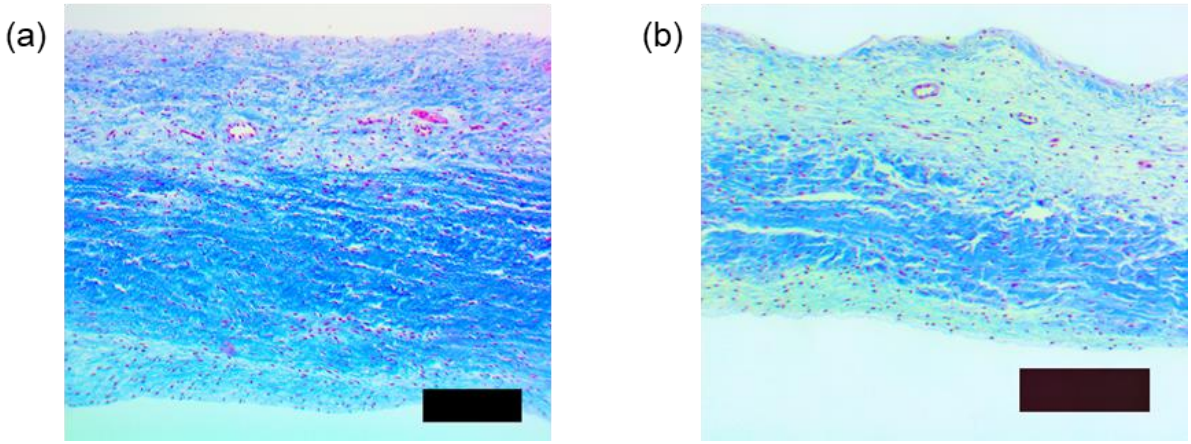

Figure B-10. Example histological data from the atrioventricular heart valves' anterior leaflets: Representative histology images of (a) the mitral valve anterior leaflet, and (b) the tricuspid valve posterior leaflet. Both are stained with a Masson's trichrome stain: collagen in blue, cytoplasm and keratin in red, and nuclei in black. Scale bar=200 μm.

8.4) Using an image processing program ImageJ (National Institute of Health, Bethesda, MD), perform color deconvolution methods to determine the percentage of each stained constituent in the tissue. For greater detail on these procedures, please refer to Ruifrok & Johnston [71].

9. Biaxial Testing Data Post Processing Procedures

9.1) Perform data image correlation (DIC) based tracking on the four fiducial markers from the images taken during the biaxial mechanical testing (**Fig. B-11**) to determine the time-dependent marker positions:

$$x_I = X_I + d_I, I = 1,2,3,4, \tag{B.2}$$

where X_I and x_I are the undeformed and deformed positions of the markers, respectively, and d_I is the displacement vector of each marker.

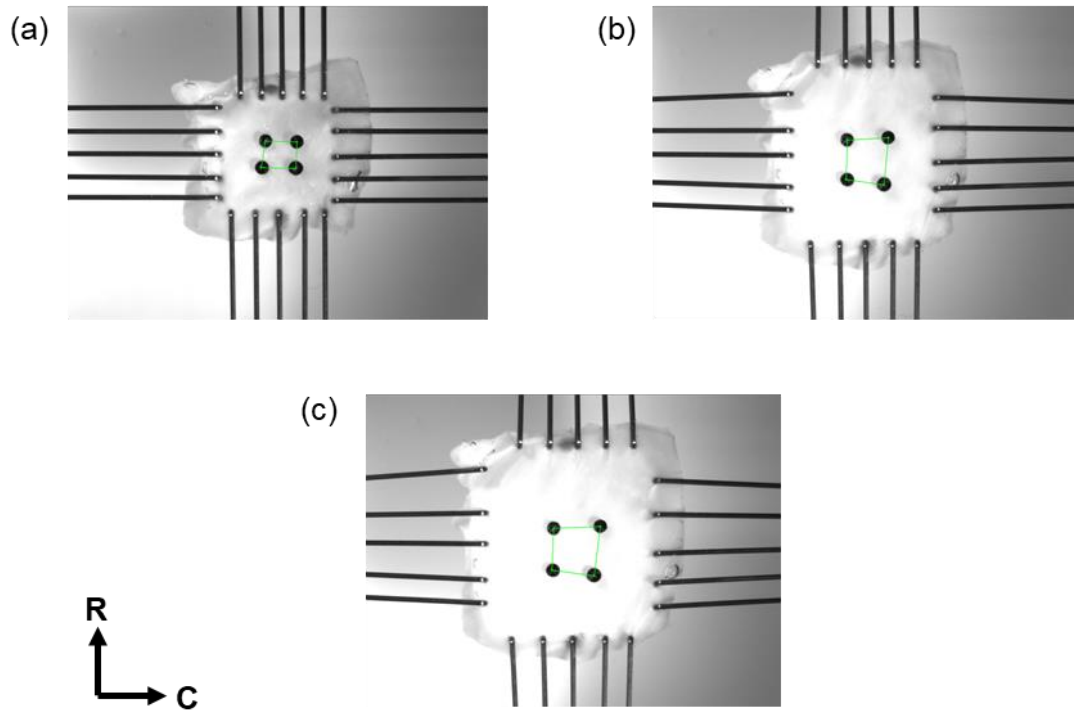

Figure B-11. Representative images illustrating the tracking of the coordinates of four fiducial markers during biaxial mechanical testing using a DIC technique: (a) the tissue mounting configuration, (b) the configuration after the preconditioning step, and (c) the deformed configuration associated with the tissue specimen under mechanical loading.

9.1.1) If it is desired to perform the analysis with respect to the mounting configuration, let X_I be the marker positions in the undeformed state at the beginning of the biaxial test. If it is

desired to perform the analysis with respect to the post-preconditioning deformation, let X_I be the marker positions at the end of the preconditioning protocol.

NOTE: The subsequent steps will be conducted in the same manner, regardless of the reference configuration chosen.

9.2) Compute the deformation gradient (**F**) of the fiducial markers using a four-node bilinear finite element [12, 105, 125]:

$$F = F(X,t) = \frac{\partial x}{\partial X} = \begin{bmatrix} \sum_{I=1}^{4} B_{XI} u_I(t) & \sum_{I=1}^{4} B_{YI} u_I(t) \\ \sum_{I=1}^{4} B_{XI} v_I(t) & \sum_{I=1}^{4} B_{YI} v_I(t) \end{bmatrix}. \quad \text{(B.3)}$$

Herein, B_{xI}'s and B_{yI}'s are the finite element shape function-derivatives in the *X*- and *Y*-directions for node *I*, respectively, and $u_I(t)$ and $v_I(t)$ are the time-dependent *X*- and *Y*-displacements, respectively, as previously determined from Step 9.1. Note the *X* and *Y* coordinates were aligned to the tissue's circumferential and radial directions.

9.3) Compute the right Cauchy-Green deformation tensor (**C**) and the Green strain tensor (**E**):

$$\mathbf{C} = \mathbf{F}^{\mathrm{T}}\mathbf{F}, \text{ and } \mathbf{E} = \frac{1}{2}(\mathbf{C}\text{-}I). \quad \text{(B.4)}$$

where *I* is the second-order identity tensor. Determine the circumferential and radial stretches by taking the square roots of the principle values of **C**.

9.4) Determine the first Piola-Kirchhoff (1st-PK) stress tensor (**P**)

$$\mathbf{P} = \frac{1}{t}\begin{bmatrix} T_{circ} & 0 \\ 0 & T_{rad} \end{bmatrix}, \quad \text{(B.5)}$$

where t is the specimen's thickness, and T_{Circ} and T_{Rad} are the applied membrane tensions in the circumferential and radial directions, respectively.

9.5) Also, compute other stress tensors, such as the Cauchy stress tensor ($\boldsymbol{\sigma}$) and the second Piola-Kirchhoff (2^{nd}-PK) stress tensor ($\mathbf{S}$), using:

$$\boldsymbol{\sigma} = J^{-1}\mathbf{P}\mathbf{F}^{T} \text{ and } \mathbf{S} = \mathbf{F}^{-1}\mathbf{P}, \tag{B.6}$$

where J is the Jacobian of the deformation gradient tensor $\mathbf{F}$.

APPENDIX C – UNIAXIAL MECHANICAL TESTING AND POLARIZED SPATIAL FREQUENCY DOMAIN IMAGING PROCEDURES FOR THE LEAFLET-CT-PAPILLARY MUSCLE ENTITY

In this appendix, the detailed procedures for the mechanical testing and polarized spatial frequency domain imaging of the chordae entities are presented.

1. Tissue Acquisition and Cleaning

Please see Section 1 of Appendix B.

2. Heart Dissection and Examination of Anatomy

2.1) Retrieve the previously cleaned heart and allow it to thaw in a warm water bath. The required materials for dissection include forceps, surgical blades, placemats, phosphate-buffered saline, and small storage containers. After the heart is completely thawed, put it on a placemat to absorb remaining blood.

2.2) Hold the heart for a top-down (superior) view to optimally observe the valve structures. Beginning with the mitral valve on the left side of the heart, use forceps to carefully manipulate the leaflets and identify a commissure, or parting line, between the leaflets.

2.3) Using a razor blade, make an incision through the commissure and the ventricle wall, opening the left ventricle (**Fig. C-1**), revealing the leaflets and the chordae tendineae structures.

2.4) Using forceps, carefully manipulate the leaflets and chordae to reveal the two thickest, strut chordae tendineae attaching on either side of the anterior leaflet apex.

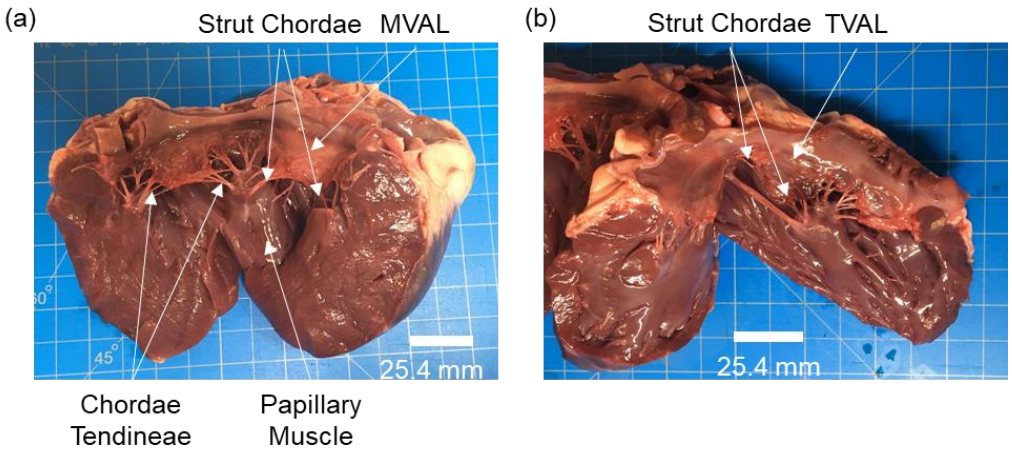

Figure C-1. The anatomical structures of a porcine: (a) mitral valve, and (b) tricuspid valve, with the strut chordae highlighted.

2.5) With a razor blade, carefully cut the non-strut chordal attachments to the leaflet.

2.6) Using forceps, stretch the leaflets taut and make cuts to separate the leaflets from the annulus. Then, make cuts to separate the papillary muscle tips with the strut chordae insertion from the surrounding valve apparatus. Place excised leaflets in an appropriately labeled container filled with PBS solution and store in a refrigerator at approximately 4 °C.

2.7) Repeat Steps 2.1-2.6 for the tricuspid valve.

3. Tissue Dissection

3.1) Retrieve the leaflet from the fridge, an incising tool such as a razor blade, forceps, and a cutting mat.

3.2) Use forceps to remove the specimen from the PBS solution and lay it flat on the cutting mat with the ventricular surface facing up, and the papillary muscle tips pulled away to make the chordae tendineae taut (**Fig. C-2**).

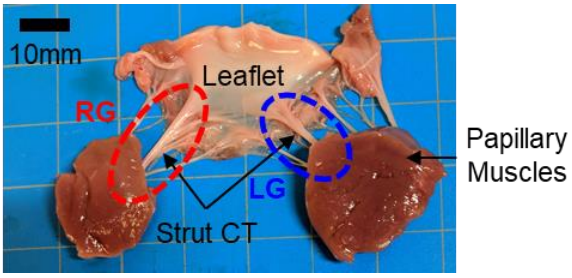

Figure C-2. The leaflet-CT-papillary muscle entity, with the ventricular surface of the leaflet facing upwards, showing the CT left group (LG) and the CT right group (RG).

3.3) Identify the insertion of the chordae into the leaflet tissue and using a razor blade make a careful cut through the leaflet tissue to bisect the tissues into two distinct groups. Keep track of these groups as the left and right groups, based on their original anatomic locations.

NOTE: With the leaflet's ventricular surface facing upwards, the orientation is flipped, so the left group will be visually on the right side, and the right group will be visually on the left side.

3.4) Take the left chordae entity group and remove any excess leaflet or papillary muscle tissues, or extra chordae attachments from the leaflet using careful cuts with a razor blade. Repeat for the right group (**Fig. C-3**).

NOTE: Be careful not to cut the strut chordae tendinea of interest or cut the leaflet or papillary muscle tip too small for mounting to the biaxial testing system.

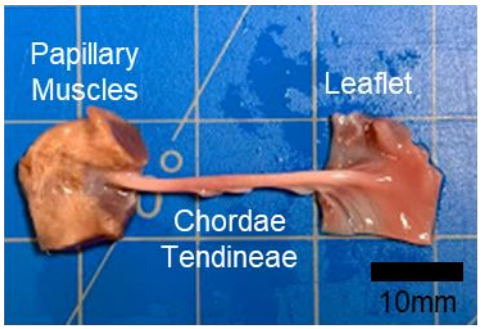

Figure C-3. A sectioned leaflet-CT-papillary muscle entity.

4. Thickness Measurements and Tester Setup

4.1) Retrieve one of the sectioned tissues specimens, a camera or digital microscope, and a small metal spatula. Using the digital calipers, measure and record the thickness of the metal spatula.

4.2) Using forceps, lay the leaflet portion of the tissue entity flat on the metal spatula. Using a digital caliper, measure the thickness of the spatula-tissue pair at three different leaflet locations. Subtract the spatula's thickness from the pair and record the average thickness value (**Fig. C-4**). It is important to minimize or avoid compression of the tissue using the digital calipers to obtain accurate thickness measurements.

Figure C-4. Measuring the CT thickness with a digital caliper.

4.3) Using a camera or digital microscope, take a picture of the chordae entity group, ensuring the use of a scalebar for appropriate measurement of the chordae thickness. Using image analysis software, measure the chordal thickness at three distinct locations. Average the thickness measurements and record the averaged thickness.

4.4) Prepare a PBS bath at 32 °C, just below the tissue's physiologic conditions.

NOTE: The physiologic temperature is 37 °C but heating the PBS to this temperature will interfere with the polarizer by causing the fogging of the lens when performing the pSFDI procedure.

5. Tissue Mounting and Fiducial Marker Placement

5.1) Retrieve forceps, tissue specimen, mounting hardware, and a surgical pen.

5.2) Mount the tissue to the testing system using tined BioRakes. While mounting, ensure the leaflet portion is mounted on the portion of the tester that is aligned with the pSFDI system (**Fig. C-5**).

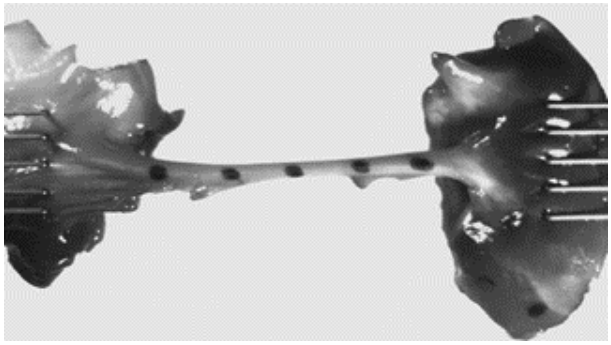

Figure C-5. The leaflet-CT-papillary muscle entity mounted to the BioTester via BioRakes.

5.3) Using the surgical pen, place 4-7 fiducial markers along the chordae length, ensuring even spacing.

6. Preconditioning Step, Duration Timing, and Mechanical Testing

6.1) Create a preconditioning protocol such that the tissue will undergo 10 loading/unloading cycles at physiologically emulating forces of 1.4 N for the mitral valve and 1.2 N with a loading rate of 4.42 N/min.

6.2) After preconditioning, note the post-preconditioning deformation, and perform a step in which the time for the tissue to move from the post-preconditioned zero force state to the maximum loading state can be recorded.

6.3) Using the recorded stretching time, create another protocol for the mechanical testing that will perform cyclic loading and unloading using the same parameters as in Step 6.1, starting from the post-preconditioning configuration, and with 5 loading/unloading cycles.

7. Polarized Spatial Frequency Domain Imaging

7.1) Once mechanical testing has been performed, identify the imaging points of interest along the final unloading force-deformation curve. Examples include the maximum loading deformation, the post-preconditioning deformation, and the deformation at one-third of the maximum loading.

7.2) Situate the pSFDI device above the testing specimen in such a way that the leaflet-CT insertion is clearly viewed through the polarizer (**Fig. C-6**), as verified with the camera software (Pylon Viewer, Basler, Germany) (**Fig. C-7**).

Note: The polarizer lens should be thoroughly checked for smudging, dust, or other imperfections that could cause interference with the pSFDI results. Using the linear rotation motor, manually turn the polarizer from 0 ° to 180 ° while observing within the camera software. If there are any interferences, use a microfiber cloth and lens cleaning solution to clean the polarizer lens.

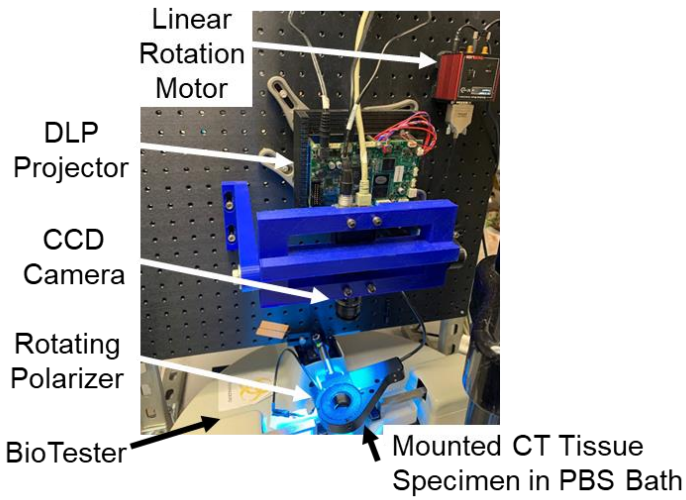

Figure C-6. Experimental photo of the integrated pSFDI-biaxial testing system.

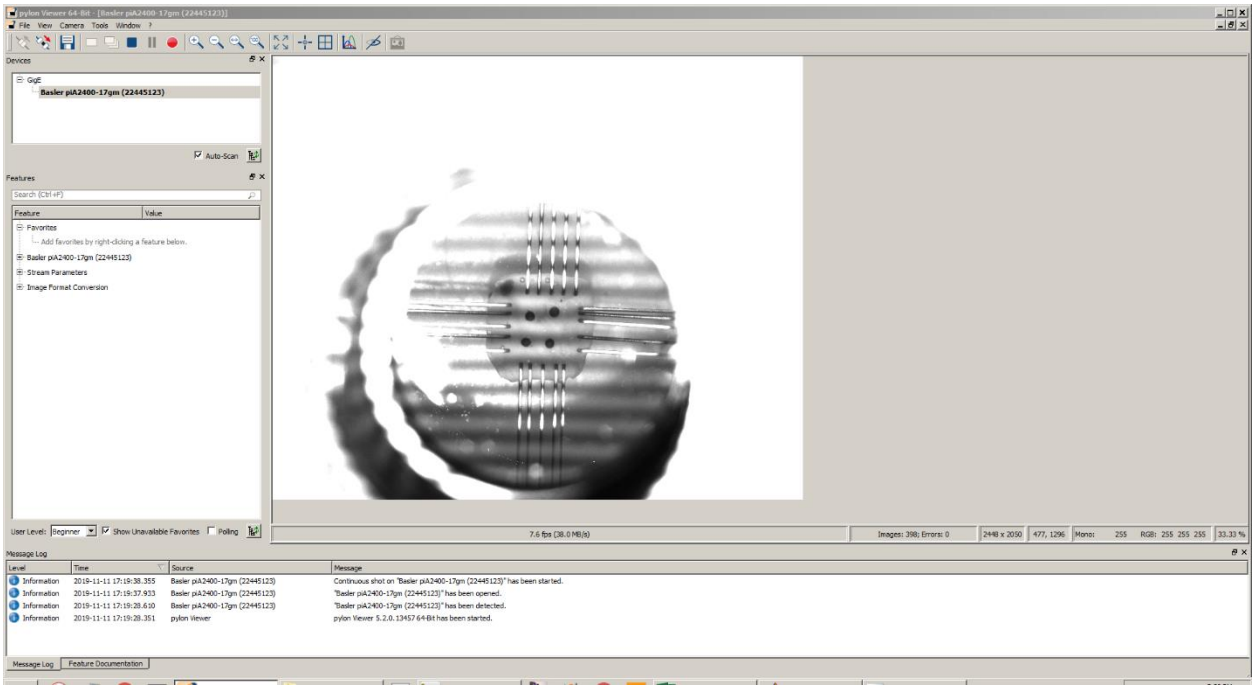

Figure C-7. The camera software used for verifying the tissue within the polarizer lens

7.3) Using the LightCrafter software (Texas Instruments, Texas, USA) prepare the cyan light projection by using the RGB color code (0, 196, 204), a flash index of 36 (corresponding to a spatial frequency of 12), and a bit depth of 8 (**Fig. C-8**).

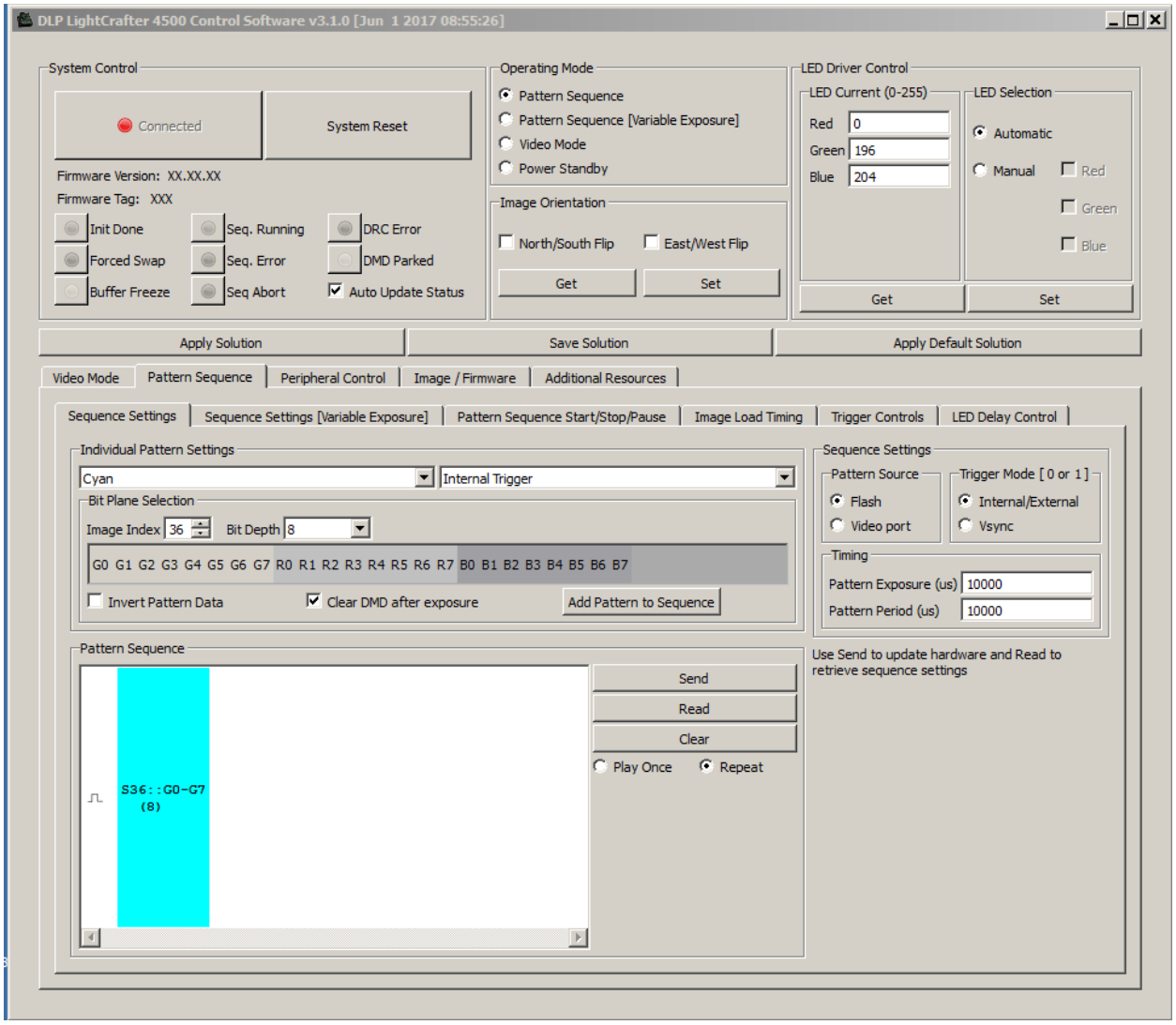

Figure C-8. The LightCrafter software, being used to project cyan light at a spatial frequency index of 12.

7.4) A custom LabView program (National Instruments, TX, USA) is used for capturing three images at each of 5 ° increments of the polarizer lens, ranging from 0 ° to 180 °, with one photo taken at each of the three phase shifts of the projected spatial frequency pattern (**Fig. C-9**). For details on the spatial frequency domain imaging theory, and the selection of the appropriate spatial frequency for the desired imaging depth, please refer to Goth *et al*. and Jett *et al*. [103, 108].

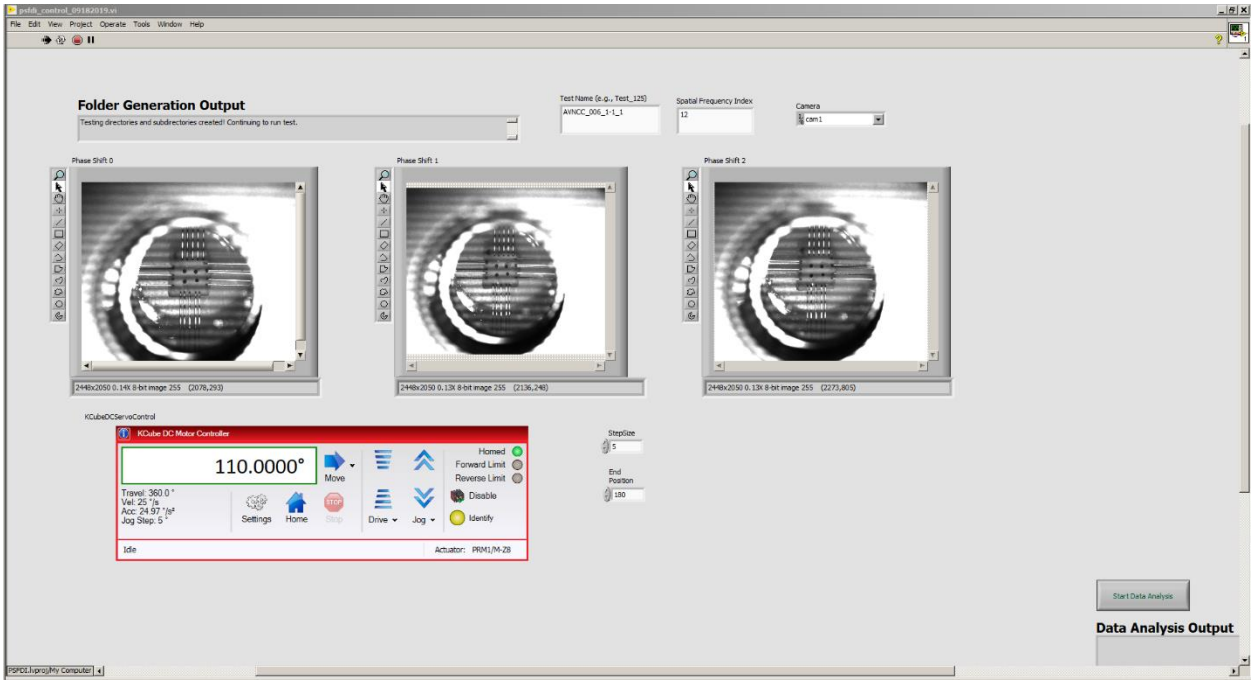

Figure C-9. The custom LabView program used for the pSFDI

7.5) Repeat Step 7.4 and perform pSFDI for all the deformations of interest.

NOTE: Fiducial markers can interfere with the degree of optical anisotropy predictions from the processing described in Appendix D. To avoid these issues, the following step order would be beneficial: Steps 5.1-2, 6.1-2, 7.1-4, and then Step 6.3. In this case, the deformations to be analyzed will be based on the final unloading cycle from the preconditioning Step 6.1.

7.6) Following the pSFDI, the images can be analyzed using in-house MATLAB programs (MathWorks, MA, USA) as described in **Appendix D**, which is in accordance to the theory outlined in Section 5.1.6.

APPENDIX D – POST-PROCESSING PIPELINE FOR MECHANICAL AND PSFDI DATA OF THE LEAFLET-CT-PAPILLARY MUSCLE ENTITIES

In Appendix D, processing scripts in MATLAB are described for quantifying the mechanical and the pSFDI information from the leaflet-CT-papillary muscle entity testing.

- For quantifying the tissue stretches of the leaflet-CT-papillary muscle entity, the BioTester-generated `CSV` file and the tracked locations of fiducial markers (`Coords`) are loaded into the MATLAB environment. First, the information from the post-preconditioning (PPC) state is used to obtain: (i) the timepoint for the beginning of the final unloading cycle, (ii) the load cell force readings and the test times, and (iii) the *x*- and *y*-pixel locations of the fiducial markers.

```
%Get the loading timepoints
folder2 = ['..\UNIAXIAL_DATA\' test_name '-MECH\'];
file3 = [folder2 test_name '-MECHData.csv'];
[num,txt,raw] = xlsread(file3);

%Find last unloading cycle
prot = raw{end,2};

%Peak loading timepoint from Data.csv
for ii = 1:length(raw)
    if strcmp(raw{ii,1},'Uniaxial')==1 && strcmp(raw{ii,2},prot) ==
1
        time_pk = raw{ii,3};
        kktemp = ii-1;
        break;
    end
end

%Get the full cycle's Data.csv info
ktemp = 1; force = []; time = [];
for ii = kktemp:length(raw)
    force(ktemp,1) = raw{ii,9};
    time(ktemp,1) = raw{ii,3}; ktemp = ktemp + 1;
end

%Load the Coords file
file2 = [folder2 'Coords1.csv'];
[coords2,txt,raw] = xlsread(file2);
tempx = 1; tempy = 1;
```

```
%Get the X and Y Coordinates from Coords
for ii = 2:size(coords2,2)
    if mod(ii,2) == 0
        x_old(:,tempx) = coords2(:,ii); tempx = tempx + 1;
    else
        y_old(:,tempy) = coords2(:,ii); tempy = tempy + 1;
    end
end

for ii = 1:length(x_old)
    if isnan(x_old(ii,1))
        temp2 = ii; break;
    end
end

x_old(temp2:end,:) = []; y_old(temp2:end,:) = [];

%Get only the x and y coords on the CT
iltemp = 1; kktemp = kktemp - 1;
for jj = kktemp:size(x_old,1)
    ix = 1; iy = 1;
    for ii = 2:2:size(x_old,2)
        x(iltemp,ix) = x_old(jj,ii); ix = ix + 1;
        y(iltemp,iy) = y_old(jj,ii); iy = iy + 1;
    end
    iltemp = iltemp + 1;
end
```

- Then, the process is repeated for the preconditioning cycles.

```
%Open the preconditioning Coords file
folder = ['..\UNIAXIAL_DATA\' test_name '-PC\'];
file = [folder 'Coords1.csv'];
[coords,txt,raw] = xlsread(file);
x_old = []; y_old = [];

%Get the mounting configuration X and Y coordinates
tempx = 1; tempy = 1;
for ii = 2:size(coords,2)
    if mod(ii,2) == 0
        x_old(:,tempx) = coords(:,ii); tempx = tempx + 1;
    else
        y_old(:,tempy) = coords(:,ii); tempy = tempy + 1;
    end
end

ix = 1; iy = 1;
for ii = 2:2:size(x_old,2);
    x_temp(1,ix) = x_old(1,ii); ix = ix + 1;
    y_temp(1,iy) = y_old(1,ii); iy = iy + 1;
end
```

```
x = [x_temp; x]; y = [y_temp; y];
%Avoid giving the spline a duplicate number (later)
for ii = 1:length(x)
    for jj = 1:size(x,2)-1
        if x(ii,jj) == x(ii,jj+1)
            x(ii,jj) = x(ii,jj)+0.000001*(ii+jj);
        end
        if y(ii,jj) == y(ii,jj+1)
            y(ii,jj) = y(ii,jj)+0.000001*(ii+jj);
        end
    end
end

%Setting things up for spline-based stretch analyses
numcol = size(coords2,2)-1;
xx = zeros(length(x),numcol/2);
for ii = 1:length(x)
    temppp = 1;
    for jj = 1:2:numcol/2
        xx(ii,jj) = x(ii,temppp);
        temppp = temppp + 1;
    end
end

for ii = 1:length(x)
    temppp = 1;
    for jj = 2:2:numcol/2
        xx(ii,jj) = y(ii,temppp);
        temppp = temppp + 1;
    end
end
```

- The information is then used in the tissue stretch calculation, with the diameter of the chordae segment is imported from the testing log file.

```
[xx, force] = get_CT_coords(testing_name{iitesting,1});
    %Function to get the CT coordinates

    %Get diameters
    file23 = ['..\UNIAXIAL_DATA\Chordae Sizes.xlsx'];
    [n,t,r] = xlsread(file23, 'InsertionRegion - Fall 19');
    for ii = 1:size(r,1)
        if strcmp(r{ii,1},testing_name{iitesting,1}) == 1
            diameter = r{ii,4}; break;
        end
    end

    nn = length(xx) / 2;
```

- Tissue stretch is then calculated with respect to the peak, the PPC, and the mounting deformations, as described in Chapters 3-5, by using a spline with 31 material points. First, the tissue stretch is determined for the individual deformation states (no continuous information for the full force loading-unloading curve).

```
    [strain_1] = compute_strain_2_node(xx(1,:), xx(2,:)); %peak
    [strain_2] = compute_strain_2_node(xx(1,:), xx(end,:)); %ppc
    [strain_3] = compute_strain_2_node(xx(end,:), xx(2,:)); %mech

    stretch_1 = sqrt(1 + 2 * strain_1);
    stretch_2 = sqrt(1 + 2 * strain_2);
    stretch_3 = sqrt(1 + 2 * strain_3);

    disp([mean(stretch_1) std(stretch_1)])
    disp([mean(stretch_2) std(stretch_2)])
    disp([mean(stretch_3) std(stretch_3)])

    ngrid = 31;

    xxyy_1 = [xx(1,1:2:end); xx(1,2:2:end)]; %MOUNTING
    xxyy_2 = [xx(2,1:2:end); xx(2,2:2:end)]; %PEAK
    xxyy_3 = [xx(end,1:2:end); xx(end,2:2:end)]; %PPC

    curve_cc_1 = cscvn(xxyy_1);
    curve_cc_2 = cscvn(xxyy_2);
    curve_cc_3 = cscvn(xxyy_3);

ss_grid_1 = linspace(curve_cc_1.breaks(1), ...
                     curve_cc_1.breaks(end), ngrid);
ss_grid_2 = linspace(curve_cc_2.breaks(1), ...
                     curve_cc_2.breaks(end), ngrid);
ss_grid_3 = linspace(curve_cc_3.breaks(1), ...
                     curve_cc_3.breaks(end), ngrid);

    grid_info_1 = fnval( curve_cc_1, ss_grid_1 )'; %MOUNTING
    grid_info_2 = fnval( curve_cc_2, ss_grid_2 )'; %PEAK
    grid_info_3 = fnval( curve_cc_3, ss_grid_3 )'; %PPC

    temp1 = [];
    temp2 = [];
    temp3 = [];

    for jj = 1:ngrid
        temp1 = [temp1, grid_info_1(jj,:)];
        temp2 = [temp2, grid_info_2(jj,:)];
        temp3 = [temp3, grid_info_3(jj,:)];
    end
```

```
        grid_info_1 = temp1;
        grid_info_2 = temp2;
        grid_info_3 = temp3;

        [strain_grid_1] = compute_strain_2_node(grid_info_1,
grid_info_2);
        [strain_grid_2] = compute_strain_2_node(grid_info_1,
grid_info_3);
        [strain_grid_3] = compute_strain_2_node(grid_info_3,
grid_info_2);

        stretch_grid_1 = sqrt(1 + 2 * strain_grid_1);
        stretch_grid_2 = sqrt(1 + 2 * strain_grid_2);
        stretch_grid_3 = sqrt(1 + 2 * strain_grid_3);

        disp([mean(stretch_grid_1) std(stretch_grid_1)])
        disp([mean(stretch_grid_2) std(stretch_grid_2)])
        disp([mean(stretch_grid_3) std(stretch_grid_3)])
```

- Then, the stretches through the full force loading-unloading curve are determined.

```
for gg = 2:size(xx,1)

            xxyy_1 = [xx(end,1:2:end); xx(end,2:2:end)];
            xxyy_2 = [xx(gg,1:2:end); xx(gg,2:2:end)];

            curve_cc_1 = cscvn(xxyy_1);
            curve_cc_2 = cscvn(xxyy_2);

            ss_grid_1 = linspace(curve_cc_1.breaks(1), ...
                                 curve_cc_1.breaks(end), ngrid);
            ss_grid_2 = linspace(curve_cc_2.breaks(1), ...
                                 curve_cc_2.breaks(end), ngrid);

            grid_info_1 = fnval( curve_cc_1, ss_grid_1 )';
            grid_info_2 = fnval( curve_cc_2, ss_grid_2 )';

            temp1 = [];
            temp2 = [];

            for jj = 1:ngrid
                temp1 = [temp1, grid_info_1(jj,:)];
                temp2 = [temp2, grid_info_2(jj,:)];
            end

            grid_info_1 = temp1;
            grid_info_2 = temp2;

            [strain_grid_all(gg,:)]=compute_strain_2_node(grid_info_1,
...
                                        grid_info_2);
```

```
            stretch_grid_all(gg,:) = sqrt(1 + 2 *
strain_grid_all(gg,:));

        end
        stretch_grid_all(1,:) = [];
        force(end) = [];
        force(end) = [];

            avg_m(1,1) = 1;
            for ii = 2:size(stretch_grid_all,1)
                avg_m(ii,1) = mean(stretch_grid_all(ii,:));
            end
            avg_m(1) = [];

            for ii = 2:length(avg_m)
                for jj = 2:length(avg_m)
                    if avg_m(ii,1) == avg_m(jj,1)
                        avg_m(ii,1) = avg_m(ii,1)+0.000001*(ii+jj);
                    end
                end
            end

            for ii = 2:length(force)
                for jj = 2:length(force)
                    if force(ii,1) == force(jj,1)
                        force(ii,1) = force(ii,1)+0.000001*(ii+jj);
                    end
                end
            end

            f_points = [];
            if strcmp(testing_name{iitesting,1}(1),'M') == 1
                f_points = [0:0.01:1.4];
            else
                f_points = [0:0.01:1.2];
            end

            force = force*1e-3;

            force = flipud(force);
            avg_m = flipud(avg_m);
            force(1) = 0;
            avg_m(1) = 1;

            mech_all(1,1) = 1;
            f_points = f_points';

            if length(force) ~= length(avg_m)
                avg_m(end) = [];
            end
```

```
for ii = 2:length(f_points)
    mech_all(ii) = interp1(force, avg_m, ...
        f_points(ii), 'nearest', 'extrap');
end
```

- On the other hand, for analyzing the pSFDI information, tissue geometries are first defined using the user-created function `grabit.m` (available via MathWorks). The geometry is composed of three pieces: (i) the leaflet insertion portion (`capture_coor2`), (ii) the chordae portion (`capture_coor3`), and (iii) the full tissue geometry (`capture_coor`) – a combination of geometries (i) and (ii). The full tissue geometry is processed to obtain the collagen fiber angle predictions and degree of optical anisotropy. Processing begins with defining the file locations for the images at each polarizer phase shift, and reading the images to MATLAB using the `imread()` built-in function.

```
temp_txt = ['spatial_freq_' num2str(sf_idx) '_'];

folder1 = [test_folder test_name '/' temp_txt 'ps_0'];
folder2 = [test_folder test_name '/' temp_txt 'ps_1'];
folder3 = [test_folder test_name '/' temp_txt 'ps_2'];

[X_temp_1] = imread([folder1 '/image_' num2str((1-1)*5)
'.tiff']);

RI = imref2d(size(X_temp_1));

II_1 = zeros(37, RI.ImageExtentInWorldY,
RI.ImageExtentInWorldX);
II_2 = zeros(37, RI.ImageExtentInWorldY,
RI.ImageExtentInWorldX);
II_3 = zeros(37, RI.ImageExtentInWorldY,
RI.ImageExtentInWorldX);

for ii = 1:37
    fprintf('ii = %d,  ', ii);

    [X_temp_1] = imread([folder1 '/image_' num2str((ii-1)*5)
...
                                    '.tiff']);
    [X_temp_2] = imread([folder2 '/image_' num2str((ii-1)*5)
...
                                    '.tiff']);
```

```
            [X_temp_3] = imread([folder3 '/image_' num2str((ii-1)*5)
...
                                            '.tiff']);

            II_1(ii, :, :) = (X_temp_1); % I_0
            II_2(ii, :, :) = (X_temp_2); % I_120
            II_3(ii, :, :) = (X_temp_3); % I_240

            if mod(ii,5) == 0 || ii == 37
                fprintf('\n');
            end
        end
        clear X_temp_1  X_temp_2  X_temp_3
```

- Then, an ID mask is generated to identify the region of interested defined by `capture_coor` so that only the pixels associated with the region of interest are processed.

```
        id_mask = zeros(RI.ImageExtentInWorldY,
RI.ImageExtentInWorldX);

        [bb, cc] = size(id_mask);

        [xx1_temp yy1_temp] = meshgrid(1:1:bb, 1:1:cc);

        xx1 = reshape(xx1_temp, [bb*cc 1]);
        yy1 = reshape(yy1_temp, [bb*cc 1]);

    point_in = inpolygon(xx1, yy1, capture_coor(:,1), ...
                                   capture_coor(:,2));

        info_in = find(point_in == 1);

    [X_temp_1,cmap1] = imread([folder1 '/image_' ...
                               num2str((1-1)*5) '.tiff']);

        RI = imref2d(size(X_temp_1));
        temp1 = RI.XWorldLimits;
        temp2 = RI.YWorldLimits;

        info_in = [info_in, xx1(info_in), yy1(info_in)];

        point_in = [point_in, xx1, yy1];
```

- Next, a defined level of smoothing for the data is prescribed using the `smoothing_window` parameter. The associated parameters are loaded into the MATLAB environment for the following processing.

```
load(['PSFDI_Auxiliary/neighbor_list_'...
      num2str(smoothing_window) '.mat'])

   id_list = id_list(info_in(:,1), :);

   ifac_AC = sqrt(2)/3;  ifac_DC = 1/3;
   theta = 0:5:180;
   nid_process = length(info_in(:,1));

   II_DC = zeros(37, nid_process);
   DC_par = zeros(8, nid_process);

   II_1_grid = zeros(37, nid_process);
   II_2_grid = zeros(37, nid_process);
   II_3_grid = zeros(37, nid_process);
   II_AC = zeros(37, nid_process);
   AC_par = zeros(8, nid_process);
```

- Linear least-squares regression is used to fit the data for deriving the Fourier series coefficients in Eq. (5.4).

```
  for ii = 1:nid_process
      if mod(ii, 50000) == 0
          fprintf('ii = %d \n', ii);
      end

      nn_temp = 0;
      I1_temp = zeros(37, 1);
      I2_temp = zeros(37, 1);
      I3_temp = zeros(37, 1);

      for jj = 1:id_list(ii,1)
          jj_id = id_list(ii, jj+1);

          if point_in(jj_id, 1) == 1
              nn_temp = nn_temp + 1;
              aa_temp = point_in(jj_id,3);
              bb_temp = point_in(jj_id,2);

              I1_temp = I1_temp + II_1(:, aa_temp, bb_temp);
              I2_temp = I2_temp + II_2(:, aa_temp, bb_temp);
              I3_temp = I3_temp + II_3(:, aa_temp, bb_temp);
          end

      end

      if idddd > 0
          I1_temp = [I1_temp(idddd+1:end); I1_temp(1:idddd)];
          I2_temp = [I2_temp(idddd+1:end); I2_temp(1:idddd)];
          I3_temp = [I3_temp(idddd+1:end); I3_temp(1:idddd)];
```

```
        elseif idddd < 0
            idddd = abs(idddd); %quick correction
            I1_temp = [I1_temp(end-idddd+1:end);
            I1_temp(1:end-idddd)];
            I2_temp = [I2_temp(end-idddd+1:end);
            I2_temp(1:end-idddd)];
            I3_temp = [I3_temp(end-idddd+1:end);
            I3_temp(1:end-idddd)];
            idddd = -idddd;
        end

        ifac_temp = 1 / nn_temp;

        I1_temp = I1_temp * ifac_temp;
        I2_temp = I2_temp * ifac_temp;
        I3_temp = I3_temp * ifac_temp;

        II_1_grid(:, ii) = I1_temp;
        II_2_grid(:, ii) = I2_temp;
        II_3_grid(:, ii) = I3_temp;

        II_DC(:, ii) = (I1_temp + I2_temp + I3_temp) * ifac_DC;

        [theta_fiber, DOA_1, DOA_2, beta] = ...
                   user_LLSR(II_DC(:, ii)', theta);

        DC_par(:, ii) = [theta_fiber, DOA_1, DOA_2, beta']';

        II_AC(:, ii) = sqrt((I1_temp - I2_temp).^2 + ...
            (I2_temp - I3_temp).^2 + ...
            (I3_temp - I1_temp).^2) * ifac_AC;

        [theta_fiber, DOA_1, DOA_2, beta] = ...
                   user_LLSR(II_AC(:, ii)', theta);

        AC_par(:, ii) = [theta_fiber, DOA_1, DOA_2, beta']';
    end
```

- Finally, the shape defined for the region of interest and the associated polygon are saved for use in future plotting and data visualization.

```
    clear xxx yyy tri cg ROI_poly tri_bool tri_ID

    xxx = info_in(:,2);
    yyy = info_in(:,3);

    tri = delaunay(xxx, yyy);
```

```
        cg(:,1) = (xxx(tri(:,1),1) + xxx(tri(:,2),1) +
xxx(tri(:,3),1))/3;
        cg(:,2) = (yyy(tri(:,1),1) + yyy(tri(:,2),1) +
yyy(tri(:,3),1))/3;

        ROI_poly = polyshape(capture_coor(:,1), capture_coor(:,2));

        tri_bool = isinterior(ROI_poly, cg(:,1), cg(:,2));
        tri_ID = find(tri_bool(:,1) == true);

        tri = tri(tri_ID,:);
```

REFERENCES

1. Fawzy, H., Fukamachi, K., Mazer, C.D., Harrington, A., Latter, D., Bonneau, D., and Errett, L., "Complete Mapping of the Tricuspid Valve Apparatus Using Three-Dimensional Sonomicrometry." *The Journal of Thoracic and Cardiovascular Surgery*, 2011. 141(4): pp. 1037-1043.
2. Meador, W.D., Mathur, M., Sugerman, G.P., Jazwiec, T., Malinowski, M., Bersi, M.R., Timek, T.A., and Rausch, M.K., "A Detailed Mechanical and Microstructural Analysis of Ovine Tricuspid Valve Leaflets." *Acta Biomaterialia*, 2020. 102: pp. 100-113.
3. Martin, M., "Heart Valve Macro-and Microstructure/Martin Misfield, Hans-Hinrich Sievers." *Phil. Trans. R. Soc. B*, 2007. 362: pp. 1421-1436.
4. Marron, K., Yacoub, M.H., Polak, J.M., Sheppard, M.N., Fagan, D., Whitehead, B.F., de Leval, M.R., Anderson, R.H., and Wharton, J., "Innervation of Human Atrioventricular and Arterial Valves." *Circulation*, 1996. 94(3): pp. 368-375.
5. Eckert, C.E., Fan, R., Mikulis, B., Barron, M., Carruthers, C.A., Friebe, V.M., Vyavahare, N.R., and Sacks, M.S., "On the Biomechanical Role of Glycosaminoglycans in the Aortic Heart Valve Leaflet." *Acta Biomaterialia*, 2013. 9(1): pp. 4653-4660.
6. Lovekamp, J.J., Simionescu, D.T., Mercuri, J.J., Zubiate, B., Sacks, M.S., and Vyavahare, N.R., "Stability and Function of Glycosaminoglycans in Porcine Bioprosthetic Heart Valves." *Biomaterials*, 2006. 27(8): pp. 1507-1518.
7. Filip, D., Radu, A., and Simionescu, M., "Interstitial Cells of the Heart Valves Possess Characteristics Similar to Smooth Muscle Cells." *Circulation research*, 1986. 59(3): pp. 310-320.
8. Mulholland, M.D.L. and Gotlieb, M.D.C.M.F.A.I., "Cardiac Valve Interstitial Cells: Regulator of Valve Structure and Function." *Cardiovascular Pathology*, 1997. 6(3): pp. 167-174.
9. Taylor, P.M., Batten, P., Brand, N.J., Thomas, P.S., and Yacoub, M.H., "The Cardiac Valve Interstitial Cell." *The International Journal of Biochemistry & Cell Biology*, 2003. 35(2): pp. 113-118.
10. Gupta, V., Werdenberg, J.A., Blevins, T.L., and Grande-Allen, K.J., "Synthesis of Glycosaminoglycans in Differently Loaded Regions of Collagen Gels Seeded with Valvular Interstitial Cells." *Tissue Engineering*, 2007. 13(1): pp. 41-49.
11. Gould, R.A., Chin, K., Santisakultarm, T.P., Dropkin, A., Richards, J.M., Schaffer, C.B., and Butcher, J.T., "Cyclic Strain Anisotropy Regulates Valvular Interstitial Cell Phenotype and Tissue Remodeling in Three-Dimensional Culture." *Acta Biomaterialia*, 2012. 8(5): pp. 1710-1719.
12. Jett, S.V., Laurence, D.W., Kunkel, R.P., Babu, A.R., Kramer, K.E., Baumwart, R., Towner, R.A., Wu, Y., and Lee, C.-H., "An Investigation of the Anisotropic Mechanical Properties and Anatomical Structure of Porcine Atrioventricular Heart Valves." *Journal of the Mechanical Behavior of Biomedical Materials*, 2018. 87: pp. 155-171.

13. Jett, S.V., Laurence, D.W., Kunkel, R.P., Babu, A.R., Kramer, K.E., Baumwart, R., Towner, R.A., Wu, Y., and Lee, C.-H., "Biaxial Mechanical Data of Porcine Atrioventricular Valve Leaflets." *Data in Brief*, 2018. 21: pp. 358-363.

14. Khoiy, K.A. and Amini, R., "On the Biaxial Mechanical Response of Porcine Tricuspid Valve Leaflets." *Journal of Biomechanical Engineering*, 2016. 138(10): p. 104504.

15. Pokutta-Paskaleva, A., Sulejmani, F., DelRocini, M., and Sun, W., "Comparative Mechanical, Morphological, and Microstructural Characterization of Porcine Mitral and Tricuspid Leaflets and Chordae Tendineae." *Acta Biomaterialia*, 2019. 85: pp. 241-252.

16. Ross, C.J., Laurence, D.W., Wu, Y., and Lee, C.-H., "Biaxial Mechanical Characterizations of Atrioventricular Heart Valves." *Journal of Visualized Experiments*, 2019. 146: p. e59170.

17. Duginski, G.A., Ross, C.J., Laurence, D.W., Johns, C.H., and Lee, C.-H., "An Investigation of the Effect of Freezing Storage on the Biaxial Mechanical Properties of Excised Porcine Tricuspid Valve Anterior Leaflets." *Journal of the Mechanical Behavior of Biomedical Materials*, 2020. 101: p. 103438.

18. Grashow, J.S., Sacks, M.S., Liao, J., and Yoganathan, A.P., "Planar Biaxial Creep and Stress Relaxation of the Mitral Valve Anterior Leaflet." *Annals of Biomedical Engineering*, 2006. 34(10): pp. 1509-1518.

19. May-Newman, K. and Yin, F.C., "Biaxial Mechanical Behavior of Excised Porcine Mitral Valve Leaflets." *American Journal of Physiology: Heart and Circulatory Physiology*, 1995. 269(4): pp. H1319-H1327.

20. Pierlot, C.M., Moeller, A.D., Lee, J.M., and Wells, S.M., "Biaxial Creep Resistance and Structural Remodeling of the Aortic and Mitral Valves in Pregnancy." *Annals of Biomedical Engineering*, 2015. 43(8): pp. 1772-1785.

21. Clark, R.E., "Stress-Strain Characteristics of Fresh and Frozen Human Aortic and Mitral Leaflets and Chordae Tendineae. Implications for Clinical Use." *Journal of Thoracic and Cardiovascular Surgery*, 1973. 66(2): pp. 202-8.

22. Grashow, J.S., Yoganathan, A.P., and Sacks, M.S., "Biaixal Stress–Stretch Behavior of the Mitral Valve Anterior Leaflet at Physiologic Strain Rates." *Annals of Biomedical Engineering*, 2006. 34(2): pp. 315-325.

23. Ayoub, S., Lee, C.-H., Driesbaugh, K.H., Anselmo, W., Hughes, C.T., Ferrari, G., Gorman, R.C., Gorman, J.H., III, and Sacks, M.S., "Regulation of Valve Interstitial Cell Homeostasis by Mechanical Deformation: Implications for Heart Valve Disease and Surgical Repair." *Journal of the Royal Society Interface*, 2017. 14(135): p. 20170580.

24. Huang, H.-Y.S., Balhouse, B.N., and Huang, S., "Application of Simple Biomechanical and Biochemical Tests to Heart Valve Leaflets: Implications for Heart Valve Characterization and Tissue Engineering." *Proceedings of the Institution of Mechanical Engineers. Part H: Journal of Engineering in Medicine*, 2012. 226(11): pp. 868-876.

25. Rego, B.V., Khalighi, A.H., Drach, A., Lai, E.K., Pouch, A.M., Gorman, R.C., Gorman III, J.H., and Sacks, M.S., "A Noninvasive Method for the Determination of in Vivo Mitral

Valve Leaflet Strains." *International Journal for Numerical Methods in Biomedical Engineering*, 2018. 34(12): p. e3142.

26. Lee, J.M., Courtman, D.W., and Boughner, D.R., "The Glutaraldehyde - Stabilized Porcine Aortic Valve Xenograft. I. Tensile Viscoelastic Properties of the Fresh Leaflet Material." *Journal of Biomedical Materials Research*, 1984. 18(1): pp. 61-77.

27. Lanir, Y. and Fung, Y.C., "Two-Dimensional Mechanical Properties of Rabbit Skin—Ii. Experimental Results." *Journal of Biomechanics*, 1974. 7(2): pp. 171-182.

28. Hosseini, S.M., Wilson, W., Ito, K., and van Donkelaar, C.C., "How Preconditioning Affects the Measurement of Poro-Viscoelastic Mechanical Properties in Biological Tissues." *Biomechanics and Modeling in Mechanobiology*, 2014. 13(3): pp. 503-513.

29. Fung, Y.C., "On Mathematical Models of Stress-Strain Relationship for Living Soft Tissues." *Polymer Mechanics*, 1975. 11(5): pp. 726-740.

30. Pham, T., Sulejmani, F., Shin, E., Wang, D., and Sun, W., "Quantification and Comparison of the Mechanical Properties of Four Human Cardiac Valves." *Acta Biomaterialia*, 2017. 54: pp. 345-355.

31. Laurence, D.W., Ross, C.J., Jett, S.V., Johns, C.H., Echols, A.L., Baumwart, R., Towner, R.A., Liao, J., Bajona, P., Wu, Y., and Lee, C.-H., "An Investigation of Regional Variations in the Biaxial Mechanical Properties and Stress Relaxation Behaviors of Porcine Atrioventricular Heart Valve Leaflets." *Journal of Biomechanics*, 2019. 83: pp. 16-27.

32. Fratzl, P., Misof, K., Zizak, I., Rapp, G., Amenitsch, H., and Bernstorff, S., "Fibrillar Structure and Mechanical Properties of Collagen." *Journal of Structural Biology*, 1998. 122(1-2): pp. 119-122.

33. Kunzelman, K.S., Cochran, R.P., Murphree, S.S., Ring, W.S., Verrier, E.D., and Eberhart, R.C., "Differential Collagen Distribution in the Mitral Valve and Its Influence on Biomechanical Behaviour." *Journal of Heart Valve Disease*, 1993. 2(2): pp. 236-244.

34. Lee, C.-H., Rabbah, J.-P., Yoganathan, A.P., Gorman, R.C., Gorman, J.H., III, and Sacks, M.S., "On the Effects of Leaflet Microstructure and Constitutive Model on the Closing Behavior of the Mitral Valve." *Biomechanics and Modeling in Mechanobiology*, 2015. 14(6): pp. 1281-1302.

35. Goth, W., Potter, S., Allen, A.C.B., Zoldan, J., Sacks, M.S., and Tunnell, J.W., "Non-Destructive Reflectance Mapping of Collagen Fiber Alignment in Heart Valve Leaflets." *Annals of Biomedical Engineering*, 2019. 47(5): pp. 1250-1264.

36. Liao, J., Yang, L., Grashow, J., and Sacks, M.S., "The Relation between Collagen Fibril Kinematics and Mechanical Properties in the Mitral Valve Anterior Leaflet." *Journal of Biomechanical Engineering*, 2007. 129(1): pp. 78-87.

37. Millington-Sanders, C., Meir, A., Lawrence, L., and Stolinski, C., "Structure of Chordae Tendineae in the Left Ventricle of the Human Heart." *Journal of Anatomy*, 1998. 192(4): pp. 573-581.

38. Ritchie, J., Warnock, J.N., and Yoganathan, A.P., "Structural Characterization of the Chordae Tendineae in Native Porcine Mitral Valves." *Annals of Thoracic Surgery*, 2005. 80(1): pp. 189-197.

39. Duran, C.M.G. and Gunning, A.J., "The Vascularization of the Heart Valves: A Comparative Study." *Cardiovascular Research*, 1968. 2(3): pp. 290-296.

40. Chen, L., Yin, F.C., and May-Newman, K., "The Structure and Mechanical Properties of the Mitral Valve Leaflet-Strut Chordae Transition Zone." *Journal of Biomechanical Engineering*, 2004. 126(2): pp. 244-251.

41. Gusukuma, L.W., Prates, J.C., Smith, R.L., Gusukuma, W.L., Prates, J.C., and Smith, R.L., "Chordae Tendineae Architecture in the Papillary Muscle Insertion." *International Journal of Morphology*, 2004. 22(4): pp. 267-272.

42. Liao, J. and Vesely, I., "Relationship between Collagen Fibrils, Glycosaminoglycans, and Stress Relaxation in Mitral Valve Chordae Tendineae." *Annals of Biomedical Engineering*, 2004. 32(7): pp. 977-983.

43. Padala, M., Sacks, M.S., Liou, S.W., Balachandran, K., He, Z., and Yoganathan, A.P., "Mechanics of the Mitral Valve Strut Chordae Insertion Region." *Journal of Biomechanical Engineering*, 2010. 132(8): p. 081004.

44. Ritchie, J., Jimenez, J., He, Z., Sacks, M.S., and Yoganathan, A.P., "The Material Properties of the Native Porcine Mitral Valve Chordae Tendineae: An *in Vitro* Investigation." *Journal of Biomechanics*, 2006. 39(6): pp. 1129-1135.

45. Tang, G.H.L., David, T.E., Singh, S.K., Maganti, M.D., Armstrong, S., and Borger, M.A., "Tricuspid Valve Repair with an Annuloplasty Ring Results in Improved Long-Term Outcomes." *Circulation*, 2006. 114(1 suppl): pp. I-577-I-581.

46. Van de Veire, N.R., Braun, J., Delgado, V., Versteegh, M.I., Dion, R.A., Klautz, R.J., and Bax, J.J., "Tricuspid Annuloplasty Prevents Right Ventricular Dilatation and Progression of Tricuspid Regurgitation in Patients with Tricuspid Annular Dilatation Undergoing Mitral Valve Repair." *The Journal of Thoracic and Cardiovascular Surgery*, 2011. 141(6): pp. 1431-1439.

47. Condado, J.A. and Velez‐Gimon, M., "Catheter‐Based Approach to Mitral Regurgitation." *Journal of Interventional Cardiology*, 2003. 16(6): pp. 523-534.

48. Flameng, W., Herijgers, P., and Bogaerts, K., "Recurrence of Mitral Valve Regurgitation after Mitral Valve Repair in Degenerative Valve Disease." *Circulation*, 2003. 107(12): pp. 1609-1613.

49. Taramasso, M., Pozzoli, A., Guidotti, A., Nietlispach, F., Inderbitzin, D.T., Benussi, S., Alfieri, O., and Maisano, F., "Percutaneous Tricuspid Valve Therapies: The New Frontier." *European Heart Journal*, 2016. 38(9): pp. 639-647.

50. Taramasso, M., Denti, P., Latib, A., Guidotti, A., Buzzatti, N., Pozzoli, A., Di Giannuario, G., La Canna, G., Colombo, A., and Alfieri, O., "Clinical and Anatomical Predictors of Mitraclip Therapy Failure for Functional Mitral Regurgitation: Single Central Clip Strategy in Asymmetric Tethering." *International Journal of Cardiology*, 2015. 186: pp. 286-288.

51. Chiang, Y.P., Chikwe, J., Moskowitz, A.J., Itagaki, S., Adams, D.H., and Egorova, N.N., "Survival and Long-Term Outcomes Following Bioprosthetic Vs Mechanical Aortic Valve Replacement in Patients Aged 50 to 69 Years." *Jama*, 2014. 312(13): pp. 1323-1329.

52. Hammermeister, K., Sethi, G.K., Henderson, W.G., Grover, F.L., Oprian, C., and Rahimtoola, S.H., "Outcomes 15 Years after Valve Replacement with a Mechanical Versus a Bioprosthetic Valve: Final Report of the Veterans Affairs Randomized Trial." *Journal of the American College of Cardiology*, 2000. 36(4): pp. 1152-1158.

53. Jamieson, W.R.E., Von Lipinski, O., Miyagishima, R.T., Burr, L.H., Janusz, M.T., Ling, H., Fradet, G.J., Chan, F., and Germann, E., "Performance of Bioprostheses and Mechanical Prostheses Assessed by Composites of Valve-Related Complications to 15 Years after Mitral Valve Replacement." *Journal of Thoracic and Cardiovascular Surgery*, 2005. 129(6): pp. 1301-1308.

54. Schoen, F.J., "Pathology of Heart Valve Substitution with Mechanical and Tissue Prostheses." *Cardiovascular Pathology*, 2001. 3.

55. Smedira, N.G., Selman, R., Cosgrove, D.M., McCarthy, P.M., Lytle, B.W., Taylor, P.C., Apperson-Hansen, C., Stewart, R.W., and Loop, F.D., "Repair of Anterior Leaflet Prolapse: Chordal Transfer Is Superior to Chordal Shortening." *Journal of Thoracic and Cardiovascular Surgery*, 1996. 112(2): pp. 287-292.

56. Sousa, U.M., Grare, P., Jebara, V., Fuzelier, J.F., Portoghese, M., Acar, C., Relland, J., Mihaileanu, S., Fabiani, J.N., and Carpentier, A., "Transposition of Chordae in Mitral Valve Repair. Mid-Term Results." *Circulation*, 1993. 88(5 Pt 2): pp. II35-8.

57. Tabata, M., Kasegawa, H., Fukui, T., Shimizu, A., Sato, Y., and Takanashi, S., "Long-Term Outcomes of Artificial Chordal Replacement with Tourniquet Technique in Mitral Valve Repair: A Single-Center Experience of 700 Cases." *Journal of Thoracic and Cardiovascular Surgery*, 2014. 148(5): pp. 2033-2038. e1.

58. Colli, A., Manzan, E., Rucinskas, K., Janusauskas, V., Zucchetta, F., Zakarkaitė, D., Aidietis, A., and Gerosa, G., "Acute Safety and Efficacy of the Neochord Procedure." *Interactive Cardiovascular and Thoracic Surgery*, 2015. 20(5): pp. 575-581.

59. Cochran, R.P. and Kuzelman, K.S., "Comparison of Viscoelastic Properties of Suture Versus Porcine Mitral Valve Chordae Tendineae." *Journal of Cardiac Surgery*, 1991. 6(4): pp. 508-513.

60. Aggarwal, A., Aguilar, V.S., Lee, C.-H., Ferrari, G., Gorman, J.H., III, Gorman, R.C., and Sacks, M.S. *Patient-Specific Modeling of Heart Valves: From Image to Simulation*. in *International Conference on Functional Imaging and Modeling of the Heart, London, UK*. 2013. Springer.

61. Ionasec, R.I., *Patient-Specific Modeling and Quantification of the Heart Valves from Multimodal Cardiac Images*. 2010, Technische Universität München: Munich, Germany.

62. Padala, M., "Patient-Specific Computational Biomechanical Modeling to Guide Mitral Valve Repair Strategy: Practicality and Value?" *Journal of Thoracic and Cardiovascular Surgery*, 2018. 155(2): pp. 606-607.

63. Foutz, T.L., Stone, E.A., and Abrams, C.F., III, "Effects of Freezing on Mechanical Properties of Rat Skin." *American Journal of Veterinary Research*, 1992. 53(5): pp. 788-792.

64. Stemper, B.D., Yoganandan, N., Stineman, M.R., Gennarelli, T.A., Baisden, J.L., and Pintar, F.A., "Mechanics of Fresh, Refrigerated, and Frozen Arterial Tissue." *Journal of Surgical Research*, 2007. 139(2): pp. 236-242.

65. Woo, S.L.-Y., Orlando, C.A., Camp, J.F., and Akeson, W.H., "Effects of Postmortem Storage by Freezing on Ligament Tensile Behavior." *Journal of Biomechanics*, 1986. 19(5): pp. 399-404.

66. Huang, H.-Y.S., Liao, J., and Sacks, M.S., "In-Situ Deformation of the Aortic Valve Interstitial Cell Nucleus under Diastolic Loading." *Journal of Biomechanical Engineering*, 2007. 129(6): pp. 880-889.

67. Reddy, J.N., *An Introduction to Continuum Mechanics*. 2013: Cambridge University Press.

68. Tadmor, E.B., Miller, R.E., and Elliott, R.S., *Continuum Mechanics and Thermodynamics: From Fundamental Concepts to Governing Equations*. 2012: Cambridge University Press.

69. Lee, C.-H., Carruthers, C.A., Ayoub, S., Gorman, R.C., Gorman, J.H., III, and Sacks, M.S., "Quantification and Simulation of Layer-Specific Mitral Valve Interstitial Cells Deformation under Physiological Loading." *Journal of Theoretical Biology*, 2015. 373: pp. 26-39.

70. Flanagan, T.C., Black, A., O'Brien, M., Smith, T.J., and Pandit, A.S., "Reference Models for Mitral Valve Tissue Engineering Based on Valve Cell Phenotype and Extracellular Matrix Analysis." *Cells Tissues Organs*, 2006. 183(1): pp. 12-23.

71. Ruifrok, A.C. and Johnston, D.A., "Quantification of Histochemical Staining by Color Deconvolution." *Analytical and Quantitative Cytology and Histology*, 2001. 23(4): pp. 291-299.

72. Shah, S.R. and Vyavahare, N.R., "The Effect of Glycosaminoglycan Stabilization on Tissue Buckling in Bioprosthetic Heart Valves." *Biomaterials*, 2008. 29(11): pp. 1645-1653.

73. Anssari-Benam, A., Tseng, Y.-T., and Bucchi, A., "A Transverse Isotropic Constitutive Model for the Aortic Valve Tissue Incorporating Rate-Dependency and Fibre Dispersion: Application to Biaxial Deformation." *Journal of the Mechanical Behavior of Biomedical Materials*, 2018. 85: pp. 80-93.

74. Anssari-Benam, A., Screen, H.R.C., and Bucchi, A., "Insights into the Micromechanics of Stress-Relaxation and Creep Behaviours in the Aortic Valve." *Journal of the Mechanical Behavior of Biomedical Materials*, 2019. 93: pp. 230-245.

75. Sacks, M.S. and Yoganathan, A.P., "Heart Valve Function: A Biomechanical Perspective." *Philosophical Transactions of the Royal Society of London B: Biological Sciences*, 2007. 362(1484): pp. 1369-1391.

76. Sacks, M.S., David Merryman, W., and Schmidt, D.E., "On the Biomechanics of Heart Valve Function." *Journal of Biomechanics*, 2009. 42(12): pp. 1804-1824.

77. Grande-Allen, K.J., Calabro, A., Gupta, V., Wight, T.N., Hascall, V.C., and Vesely, I., "Glycosaminoglycans and Proteoglycans in Normal Mitral Valve Leaflets and Chordae: Association with Regions of Tensile and Compressive Loading." *Glycobiology*, 2004. 14(7): pp. 621-633.

78. Vyavahare, N., Ogle, M., Schoen, F.J., Zand, R., Gloeckner, D.C., Sacks, M., and Levy, R.J., "Mechanisms of Bioprosthetic Heart Valve Failure: Fatigue Causes Collagen Denaturation and Glycosaminoglycan Loss." *Journal of Biomedical Materials Research*, 1999. 46(1): pp. 44-50.

79. Cacho, F., Elbischger, P.J., Rodriguez, J.F., Doblaré, M., and Holzapfel, G.A., "A Constitutive Model for Fibrous Tissues Considering Collagen Fiber Crimp." *International Journal of Non-Linear Mechanics*, 2007. 42(2): pp. 391-402.

80. Kroon, M. and Holzapfel, G.A., "A New Constitutive Model for Multi-Layered Collagenous Tissues." *Journal of Biomechanics*, 2008. 41(12): pp. 2766-2771.

81. Lee, C.-H., Zhang, W., Feaver, K., Gorman, R.C., Gorman, J.H., 3rd, and Sacks, M.S., "On the *in Vivo* Function of the Mitral Heart Valve Leaflet: Insights into Tissue–Interstitial Cell Biomechanical Coupling." *Biomechanics and Modeling in Mechanobiology*, 2017. 16(5): pp. 1613-1632.

82. Sacks, M.S., "Incorporation of Experimentally-Derived Fiber Orientation into a Structural Constitutive Model for Planar Collagenous Tissues." *Journal of Biomechanical Engineering*, 2003. 125(2): pp. 280-287.

83. Stevanella, M., Maffessanti, F., Conti, C.A., Votta, E., Arnoldi, A., Lombardi, M., Parodi, O., Caiani, E.G., and Redaelli, A., "Mitral Valve Patient-Specific Finite Element Modeling from Cardiac Mri: Application to an Annuloplasty Procedure." *Cardiovascular Engineering and Technology*, 2011. 2(2): pp. 66-76.

84. Holzapfel, G.A., Niestrawska, J.A., Ogden, R.W., Reinisch, A.J., and Schriefl, A.J., "Modelling Non-Symmetric Collagen Fibre Dispersion in Arterial Walls." *Journal of the Royal Society Interface*, 2015. 12(106): p. 20150188.

85. Prot, V., Skallerud, B., Sommer, G., and Holzapfel, G.A., "On Modelling and Analysis of Healthy and Pathological Human Mitral Valves: Two Case Studies." *Journal of the Mechanical Behavior of Biomedical Materials*, 2010. 3(2): pp. 167-177.

86. Holzapfel, G.A. and Ogden, R.W., "Constitutive Modelling of Arteries." *Proceedings of the Royal Society of London, Series A; Mathematical and Physical Sciences*, 2010. 466(2118): pp. 1551-1597.

87. Rego, B.V., Wells, S.M., Lee, C.-H., and Sacks, M.S., "Mitral Valve Leaflet Remodelling During Pregnancy: Insights into Cell-Mediated Recovery of Tissue Homeostasis." *Journal of the Royal Society Interface*, 2016. 13(125): p. 20160709.

88. Ambrosi, D., Ateshian, G.A., Arruda, E.M., Cowin, S.C., Dumais, J., Goriely, A., Holzapfel, G.A., Humphrey, J.D., Kemkemer, R., and Kuhl, E., "Perspectives on Biological Growth and Remodeling." *Journal of the Mechanics and Physics of Solids*, 2011. 59(4): pp. 863-883.

89. Humphrey, J.D. and Rajagopal, K.R., "A Constrained Mixture Model for Growth and Remodeling of Soft Tissues." *Mathematical Models and Methods in Applied Sciences*, 2002. 12(03): pp. 407-430.

90. Mol, A., Smits, A.I.P.M., Bouten, C.V.C., and Baaijens, F.P.T., "Tissue Engineering of Heart Valves: Advances and Current Challenges." *Expert Review of Medical Devices*, 2009. 6(3): pp. 259-275.

91. Schenke-Layland, K., Vasilevski, O., Opitz, F., König, K., Riemann, I., Halbhuber, K.J., Wahlers, T.H., and Stock, U.A., "Impact of Decellularization of Xenogeneic Tissue on Extracellular Matrix Integrity for Tissue Engineering of Heart Valves." *Journal of Structural Biology*, 2003. 143(3): pp. 201-208.

92. Lomholt, M., Nielsen, S.L., Hansen, S.B., Andersen, N.T., and Hasenkam, J.M., "Differential Tension between Secondary and Primary Mitral Chordae in an Acute in-Vivo Porcine Model." *Journal of Heart Valve Disease*, 2002. 11(3): pp. 337-345.

93. Zuo, K., Pham, T., Li, K., Martin, C., He, Z., and Sun, W., "Characterization of Biomechanical Properties of Aged Human and Ovine Mitral Valve Chordae Tendineae." *Journal of the Mechanical Behavior of Biomedical Materials*, 2016. 62: pp. 607-618.

94. Gunning, G.M. and Murphy, B.P., "Characterisation of the Fatigue Life, Dynamic Creep and Modes of Damage Accumulation within Mitral Valve Chordae Tendineae." *Acta Biomaterialia*, 2015. 24: pp. 193-200.

95. Silver, M.D., Lam, J.H.C., Ranganathan, N., and Wigle, E.D., "Morphology of the Human Tricuspid Valve." *Circulation*, 1971. 43(3): pp. 333-348.

96. Chuong, C.-J. and Fung, Y.-C., *Residual Stress in Arteries*, in *Frontiers in Biomechanics*, G.W. Schmid-Schnöbein, S.L.-Y. Woo, and B.W. Zweifach, Editors. 1986, Springer-Verlag: New York. pp. 117-129.

97. Jimenez, J.H., Soerensen, D.D., He, Z., He, S., and Yoganathan, A.P., "Effects of a Saddle Shaped Annulus on Mitral Valve Function and Chordal Force Distribution: An *in Vitro* Study." *Annals of Biomedical Engineering*, 2003. 31(10): pp. 1171-1181.

98. Hughes, T.J., *The Finite Element Method: Linear Static and Dynamic Finite Element Analysis*. 2012: Courier Corporation.

99. Eckert, C.E., Zubiate, B., Vergnat, M., Gorman, J.H., Gorman, R.C., and Sacks, M.S., "In Vivo Dynamic Deformation of the Mitral Valve Annulus." *Annals of Biomedical Engineering*, 2009. 37(9): pp. 1757-1771.

100. Ogden, R.W., *Elastic Deformations of Rubberlike Solids*, in *Mechanics of Solids*, H.G. Hopkins and M.J. Sewell, Editors. 1982, Pergamon: New York. pp. 499-537.

101. Storn, R. and Price, K., "Differential Evolution–a Simple and Efficient Heuristic for Global Optimization over Continuous Spaces." *Journal of Global Optimization*, 1997. 11(4): pp. 341-359.

102. Liao, J. and Vesely, I., "A Structural Basis for the Size-Related Mechanical Properties of Mitral Valve Chordae Tendineae." *Journal of Biomechanics*, 2003. 36(8): pp. 1125-1133.

103. Jett, S.V., Hudson, L.T., Baumwart, R., Bohnstedt, B.N., Mir, A., Burkhart, H.M., Holzapfel, G.A., Wu, Y., and Lee, C.-H., "Integration of Polarized Spatial Frequency Domain Imaging (Psfdi) with a Biaxial Mechanical Testing System for Quantification of Load-Dependent Collagen Architecture in Soft Collagenous Tissues." *Acta Biomaterialia*, 2020. 102: pp. 149-168.

104. Humphrey, J.D., Vawter, D.L., and Vito, R.P., "Quantification of Strains in Biaxially Tested Soft Tissues." *Journal of Biomechanics*, 1987. 20(1): pp. 59-65.

105. Billiar, K.L. and Sacks, M.S., "A Method to Quantify the Fiber Kinematics of Planar Tissues under Biaxial Stretch." *Journal of Biomechanics*, 1997. 30(7): pp. 753-756.

106. Sedransk, K.L., Grande-Allen, K.J., and Vesely, I., "Failure Mechanics of Mitral Valve Chordae Tendineae." *Journal of Heart Valve Disease*, 2002. 11(5): pp. 644-650.

107. Rabbah, J.-P., Saikrishnan, N., and Yoganathan, A.P., "A Novel Left Heart Simulator for the Multi-Modality Characterization of Native Mitral Valve Geometry and Fluid Mechanics." *Annals of Biomedical Engineering*, 2013. 41(2): pp. 305-315.

108. Goth, W., Yang, B., Lesicko, J., Allen, A., Sacks, M.S., and Tunnell, J.W. *Polarized Spatial Frequency Domain Imaging of Heart Valve Fiber Structure*. in *Proceedings of SPIE Volume 9710, Optical Elastography and Tissue Biomechanics III*. 2016.

109. Salvador, L., Mirone, S., Bianchini, R., Regesta, T., Patelli, F., Minniti, G., Masat, M., Cavarretta, E., and Valfrè, C., "A 20-Year Experience with Mitral Valve Repair with Artificial Chordae in 608 Patients." *Journal of Thoracic and Cardiovascular Surgery*, 2008. 135(6): pp. 1280-1287.e1.

110. Seeburger, J., Rinaldi, M., Nielsen, S.L., Salizzoni, S., Lange, R., Schoenburg, M., Alfieri, O., Borger, M.A., Mohr, F.W., and Aidietis, A., "Off-Pump Transapical Implantation of Artificial Neo-Chordae to Correct Mitral Regurgitation: The Tact Trial (Transapical Artificial Chordae Tendinae) Proof of Concept." *Journal of the American College of Cardiology*, 2014. 63(9): pp. 914-919.

111. Venkatasubramanian, R.T., Grassl, E.D., Barocas, V.H., Lafontaine, D., and Bischof, J.C., "Effects of Freezing and Cryopreservation on the Mechanical Properties of Arteries." *Annals of Biomedical engineering*, 2006. 34(5): pp. 823-832.

112. O'Leary, S.A., Doyle, B.J., and McGloughlin, T.M., "The Impact of Long Term Freezing on the Mechanical Properties of Porcine Aortic Tissue." *Journal of the Mechanical Behavior of Biomedical Materials*, 2014. 37: pp. 165-173.

113. Ross, C.J., Laurence, D.W., Hsu, M.-C., Baumwart, R., Zhao, Y.D., Mir, A., Burkhart, H.M., Holzapfel, G.A., Wu, Y., and Lee, C.-H., "Mechanics of Porcine Heart Valves' Strut Chordae Tendineae Investigated as a Leaflet–Chordae–Papillary Muscle Entity." *Annals of Biomedical Engineering*, 2020. 48(5): pp. 1463-1474.

114. Hughes, T.J.R., *The Finite Element Method: Linear Static and Dynamic Finite Element Analysis*. 2000: Courier Corporation.

115. Ogden, R.W., "Large Deformation Isotropic Elasticity–on the Correlation of Theory and Experiment for Incompressible Rubberlike Solids." *Proceedings of the Royal Society of London. A. Mathematical and Physical Sciences*, 1972. 326(1567): pp. 565-584.

116. Lim, K.O. and Boughner, D.R., "Mechanical Properties of Human Mitral Valve Chordae Tendineae: Variation with Size and Strain Rate." *Canadian Journal of Physiology and Pharmacology*, 1975. 53(3): pp. 330-339.

117. Lim, K.O. and Boughner, D.R., "Morphology and Relationship to Extensibility Curves of Human Mitral Valve Chordae Tendineae." *Circulation Research*, 1976. 39(4): pp. 580-585.

118. Lim, K.O., "Mechanical Properties and Ultrastructure of Normal Human Tricuspid Valve Chordae Tendineae." *Japanese Journal of Physiology*, 1980. 30(3): pp. 455-464.

119. Sacks, M.S., Smith, D.B., and Hiester, E.D., "A Small Angle Light Scattering Device for Planar Connective Tissue Microstructural Analysis." *Annals of Biomedical Engineering*, 1997. 25(4): pp. 678-689.

120. Cyron, C.J. and Humphrey, J.D., "Growth and Remodeling of Load-Bearing Biological Soft Tissues." *Meccanica*, 2017. 52(3): pp. 645-664.

121. Horvat, N., Virag, L., Holzapfel, G.A., Sorić, J., and Karšaj, I., "A Finite Element Implementation of a Growth and Remodeling Model for Soft Biological Tissues: Verification and Application to Abdominal Aortic Aneurysms." *Computer Methods in Applied Mechanics and Engineering*, 2019. 352: pp. 586-605.

122. Lam, J.H.C., Ranganathan, N., Wigle, E.D., and Silver, M.D., "Morphology of the Human Mitral Valve." *Circulation*, 1970. 41(3): pp. 449-458.

123. Gillinov, A.M., Cosgrove, D.M., Blackstone, E.H., Diaz, R., Arnold, J.H., Lytle, B.W., Smedira, N.G., Sabik, J.F., McCarthy, P.M., and Loop, F.D., "Durability of Mitral Valve Repair for Degenerative Disease." *The Journal of Thoracic and Cardiovascular Surgery*, 1998. 116(5): pp. 734-743.

124. Jensen, M.O., Jensen, H., Levine, R.A., Yoganathan, A.P., Andersen, N.T., Nygaard, H., Hasenkam, J.M., and Nielsen, S.L., "Saddle-Shaped Mitral Valve Annuloplasty Rings Improve Leaflet Coaptation Geometry." *Journal of Thoracic and Cardiovascular Surgery*, 2011. 142(3): pp. 697-703.

125. Sacks, M.S., "Biaxial Mechanical Evaluation of Planar Biological Materials." *Journal of Elasticity and the Physical Science of Solids*, 2000. 61(1): pp. 199-246.